UNIVERSITÀ DEGLI STUDI DI CAMERINO

school of Advanced Studies

DOCTORAL COURSE IN Science and Technology
Cycle XXXIV

Electron Spectroscopy with the SLICES setup

PhD Student
Naomi Marchini

Supervisor
Prof. Stefano Simonucci

Co-Supervisor
Dott.ssa Adriana Nannini

Coordinator
Prof. Andrea Perali

Contents

Introduction

The subject of this thesis is the setup of a new spectrometer for internal conversion electron measurements, SLICES (Spes Low energy Internal Conversion Electron Spectrometer), and its first use in an experiment aimed to study the structure of the low-lying states in ^{106}Pd.

Electron spectroscopy is a powerful tool in the investigation of fundamental properties of the atomic nucleus, essential in the study of nuclear structure, where empirical nuclear models provide a framework to understand many nuclear phenomena. For instance shape coexistence, that is, following the Poves [55] states, " a very peculiar nuclear phenomenon consisting in the presence in the same nuclei, at low excitation energy, and within a very narrow energy range, of two or more states (or bands of states) which: (a) have well defined and distinct properties, and, (b) which can be interpreted in terms of different intrinsic shapes.".

Shape coexistence is a widespread feature that is thought to occur in nearly all nuclei [32]. It is associated with the fundamental tendency of nuclei to deform, if not in their ground states, in their excited states. The distinctive character of shape coexistence lies in the interplay between two opposing trends: shell and subshell closures have a stabilizing effect leading to sphericity while residual interactions between protons and neutrons outside closed shells drive the nucleus to deformation.

The study of electric monopole transitions between nuclear states having the same spin and parity, the main topic of this thesis, can give an important contribution to clarify the configuration of the nuclear states. Electric monopole (E0) transitions are determined by a change in the radial distribution of the electric charge inside the nucleus, and high E0 transition strengths are expected whenever configurations with different mean-square charge radii mix. In this regard, an enhancement of the monopole strength in transitions between $\Delta J = 0$ states may be considered as a "signature" for shape coexistence [34]. This conclusion involves also states with J>0, in fact, as recently pointed out in Ref. [67], $J^{\pi} \rightarrow J^{\pi}$ $(J \neq 0)$ transitions in both even and odd nuclei with shape-coexisting configurations can have large E0 components accompanying their M1+E2 allowed multipolarities.

E0 transitions play a crucial role in determining nuclear structure properties and provide sensitive tests for nuclear models, developed since the second half of the 20^{th} century, from the formulation of the Shell Model [48] and the Bohr-Mottelson Hamiltonian [11] to the Interacting Boson Model [33].

The measurement of the monopole strength is complicated by the fact that E0 transitions can proceed solely via internal conversion or pair production (if the transition energy is larger than $2m_0c^2$). Simultaneous emission of two photons is a higher order process (relative probability $\sim 10^{-3} \div 10^{-4}$) and is usually neglected.

The measurement of conversion electrons is typically achieved using silicon detectors, drifted with lithium (Si(Li)), coupled with a magnetic transport system. The latter allows a high efficiency for electron collection on the detector together with the powerful rejection of background γ-rays.

The design of the different components of the magnetic transport system, studied in detail in this thesis, depends also on the electron energies of interest. In each case, before proposing an experiment, Monte Carlo simulations for different configurations have to be performed. For this reason, a GEANT4 simulation has been implemented to provide useful tools to plan future experiments with SLICES, paving the way to experimental campaigns with radioactive beams.

Advances in accelerator and ion-source technologies have made it possible to produce Radioactive Ion Beams (RIBs) and have thus opened many horizons to investigate the structure of exotic nuclei. The Selective Production of Exotic Species (SPES) facility [61], currently under construction at INFN Laboratori Nazionali di Legnaro (LNL), aims to produce RIBs using the Isotope Separation OnLine (ISOL) technique with a particular focus on neutron-rich beams in the vicinity of ^{78}Ni and ^{132}Sn, where detailed nuclear structure information is scarce. The development of an experimental setup to perform electron spectroscopy of radioactive beam represents a crucial requirement for the SPES project. To this end, SLICES has been developed to be used in conjunction with the β-decay station that is envisaged at the SPES low energy beam line.

Waiting for the future radioactive SPES beams, the commissioning of SLICES has been successfully performed at LNL using the proton beams provided by the Van de Graaf CN accelerator at LNL. The levels of interest have been populated via EC/β^+ decays of ^{106}Ag produced in the ^{106}Pd(p,n)^{106}Ag reaction. Following the decay of the ^{106}Ag isotope, the ^{106}Pd isotope was populated in its excited states. In the nuclear de-excitation process, γ-rays and internal conversion electrons are emitted. In our spectroscopic study, these were detected by an HPGe detector and the SLICES spectrometer, respectively. The measurement was performed alternating irradiation and measurement periods using a movable target remotely controlled with a dedicated control system developed in this thesis.

Measurements of E0 strengths for transitions between the first excited states 0^+ and 2^+ in this nucleus have been achieved. The isotope was carefully chosen: some nuclear observables were known with high accuracy, offering the possibility to have a stringent test for the new setup. However, some observables necessary to the ^{106}Pd structure description had never been measured, and, for others, conflicting results were available in the literature.

The theoretical interpretation of Palladium isotopes is still controversial: on one hand, their level schemes have been organized into rotational bands, while on the other hand they have been interpreted as vibrational-like nuclei in the framework of Interacting Boson Model (IBM). The predictions of this model have been compared to the experimental values for many nuclear observables e.g. excitation energies, static moment and E2/M1 transition strengths but a systematic study of the E0 strengths is still missing. For this reason, in the present work, IBM calculations of E0 transitions have been performed in order to further clarify the level scheme interpretation of ^{104,106}Pd isotopes. A re-analysis of old ICE data on ^{104}Pd has been performed with the intent to extend our study in the Palladium isotopic chain.

The thesis is organized as follows: Chapter 1 introduces the general framework of this work, describing the nuclear observables relevant in the considered experiment, the theoretical models used in the description of the nuclei of interest, and the definition of nuclear shape coexistence phenomenon. The spectroscopic information obtained from the measurements of internal conversion electrons are presented in chapter 2, focusing on the experimental techniques involved in this thesis. Finally, a review of the current experimental and theoretical knowledge on the structure of even-even Pd isotopes is provided. Chapter 3 describes the experimental setup, starting from an overview of the SPES facility and its β-decay station, followed by a detailed description of the SLICES spectrometer components, with particular attention to the tests performed for the Si(Li) detector and the design of the magnetic transport system components. The commissioning experiment of SLICES is presented in chapter 4. Since this was the first experiment using SLICES, a detailed description of the setup implemented for the CN accelerator and of the controls developed in this work is provided. The data reduction and the comparison between the obtained results and previous measurements are presented. In chapter 5 the experimental results are interpreted by performing IBM calculations, followed by a description of the ground state and first excited 0^+ state in the context of the two-level mixing model. Finally, the outcome of this work is summarized in Chapter 6.

1. Outlines of some collective models

The most ambitious goal of nuclear structure physics is to describe the fundamental properties of all the atomic nuclei, starting from their building blocks, protons and neutrons. From the theoretical point of view, several studies have been developed in order to describe the properties of nuclei with A > 40. For these many body systems, the Schrödinger equation is not exactly solvable and the establishment of their properties starting from the interaction of all nucleons is not a feasible task. A reasonable approach is the use of optimized models. These models belong essentially to three classes. The first class assumes that the nucleons interact strongly in the interior of the nucleus and that their mean free path is small compared to the nuclear dimension. These are the collective models which study phenomena that involve the nucleus as a whole. Examples are the vibrational and rotational models. The second class is represented by the independent particle models that assume that the Pauli principle restricts the collisions of the nucleons inside the nuclear matter, leading to a larger mean free path, the most conspicuous example is the shell model. The third class is that of the algebraic models, such as the interacting boson model (IBM), based on group theory and dynamical symmetry.

In this chapter, the observables important for the study of the atomic nucleus are introduced. In the following, the basic ideas of three theoretical approaches will be briefly presented: the modern shell model, the collective vibrational and rotational models, and the interacting boson model. In particular, the last one will be used to analyse the results of the ^{106}Pd experiment discussed in this thesis.

1.1 Nuclear Observables

1.1.1 Electromagnetic Nuclear Properties

A nucleus can be found in different quantum states characterized by excitation energy, angular momentum and parity. The study of the discrete spectrum associated with the excited states provides information about the nuclear structure. The energy, the spin and the parity of the states can be obtained by measuring the energies, intensities, angular distributions and polarizations of the γ-rays emitted by the nucleus during its de-excitation. In order to obtain further and precise indications about the nuclear microscopic and macroscopic degrees of freedom, it is useful to measure also transition probabilities and electromagnetic static moments of the excited states. Most of the experimental information that have been obtained about the nuclear excited states derive from studies concerning not the strong nuclear interaction, but the much weaker (and better understood) electromagnetic interaction. It is well known how the electromagnetic field can be decomposed by a multipole expansion into components, each carrying a definite angular momentum L. A transition with an associated angular momentum L can be further distinguished as having an electric (EL) or magnetic (ML) multipolarity according to the parity of the associated field component given by:

$$\pi\,(EL) = (-1)^L \qquad \pi\,(ML) = (-1)^{L+1} \tag{1.1}$$

Considering a γ-ray emitted by a nucleus in the de-excitation from an initial state of angular momentum J_i and parity π_i, to a final state with J_f and π_f , the conservation of the angular momentum and parity requires the following rules to be satisfied:

$$|J_i - J_f| \leq L \leq J_i + J_f \qquad (no\ L = 0) \tag{1.2}$$

and

$$EL:\ \pi_i \cdot \pi_f = (-1)^L \qquad ML:\ \pi_i \cdot \pi_f = (-1)^{L+1} \tag{1.3}$$

for electric and magnetic multipoles, respectively. The reduced transition probability for an electromagnetic transition of multipolarity Ω (E or M) can be expressed as

$$B\,(\Omega L; J_i \longrightarrow J_f) = \frac{1}{2J_i+1}\,|\langle J_f||M(\Omega L)||J_i\rangle|^2 \tag{1.4}$$

where M(ΩL) is the electromagnetic operator. B(EL) values are typically expressed in $e^2\mathrm{fm}^{2\mathrm{L}}$, while B(ML) values $\mu_N^2\mathrm{fm}^{2(\mathrm{L}-1)}$ where e is the electron charge and μ_N is the nuclear magneton. In both cases, barns units are also used instead of fm (1b =100 fm^2). The Weisskopf estimates of the γ-decay probabilities, which give the possibility to compare different transition probabilities related to different nuclei and to different multipoles, are expressed as:

$$EL:\ \ 1\ \mathrm{W.u.} = \frac{1}{4\pi}\left(\frac{3}{\mathrm{L}+3}\right)^2 \left(1.2\mathrm{A}^{1/3}\right)^{2\mathrm{L}}\ \ e^2\mathrm{fm}^{2\mathrm{L}} \tag{1.5}$$

$$ML:\ \ 1\ \mathrm{W.u.} = \frac{10}{\pi}\left(\frac{3}{\mathrm{L}+3}\right)^2 \left(1.2\mathrm{A}^{1/3}\right)^{2\mathrm{L}-2}\ \ \mu_\mathrm{N}^2\mathrm{fm}^{2(\mathrm{L}-1)} \tag{1.6}$$

(where A is the mass number). The decay rate T for a transition of multipolarity Ω, expressed in Hz, is given by:

$$T(\sigma L; J_i \to J_f) = \frac{8\pi L+1}{L[(2L+1)!!]^2}\frac{1}{\hbar}\left(\frac{E_\gamma}{\hbar c}\right)^{2L+1} B(\sigma L; J_i \to J_f) \tag{1.7}$$

where E is the energy of the emitted γ-ray. The lifetime τ of a state is the inverse of the sum of the partial decay rates, considering all the possible final states and the different multipolarities that are involved. In the simplest example is the very common case of an E2 transition connecting the first excited 2_1^+ state to a ground state $0_{g.s.}^+$ the relation is:

$$\tau = \frac{1}{T\left(E2; 2_1^+ \longrightarrow 0_{g.s}\right)} \tag{1.8}$$

A γ transition can have more than one multipolarity ΩL allowed by the selection rules (the most common case being a mixed E2/M1 multipolarities). In this case the mixing ratio δ is defined as the ratio of the reduced matrix elements for each multipole operator:

$$\delta = \frac{\langle J_f||M(\Omega' L')||J_i\rangle}{\langle J_f||M(\Omega L)||J_i\rangle} \tag{1.9}$$

(L'> L is assumed by convention). Hence δ expresses the ratio of the transition probabilities of the two competing de-excitation modes, ΩL and Ω'L'. The sign of δ depends on the definition of the reduced matrix elements. The Krane-Steffen convention for the sign of the mixing ratio has been used in this work [41].

1.1.2 Nuclear Shape

The nuclear shape can be expanded in an infinite series of spherical harmonics and written as:

$$R\left(\theta,\phi\right) = R_0\left[1+\sum_{\lambda=0}^{\infty}\sum_{\mu=-\lambda}^{\lambda}\alpha_{\lambda\mu}Y_{\lambda\mu}\left(\theta,\phi\right)\right] \tag{1.10}$$

where R_0 is the radius of a spherical nucleus with an equivalent volume, $Y_{\lambda\mu}$ are the usual spherical harmonics function of the polar and azimuthal angles and $\alpha_{\lambda\mu}$ are spherical tensor components (possibly time dependent). The index λ indicates the type of deformation:

- $\lambda = 0$ corresponds to a change in the radius of a spherical form.
- $\lambda = 1$ corresponds to the motion of the center of mass
- $\lambda = 2$ corresponds to quadrupole oscillations, the most frequent ones in the nuclei, that represent the most important deformation of interest in the following. A positive quadrupole deformation means that the nuclear shape is a prolate one, with polar axis longer than equatorial radius. A negative quadrupole deformation is one in which the nucleus has an oblate shape, with equatorial radius longer than polar one.
- $\lambda = 3, 4$ correspond to octupole and hexadecapole oscillations respectively.

Focusing on λ=2, the quadrupole deformed surface is an ellipsoid randomly oriented in space. The five coordinates $\alpha_{2,\mu}$ may thus be mapped onto a set of other five variables a_0, a_2, θ_1, θ_2, θ_3, three of which describe angular orientations of the ellipsoid, the other two parameters being related to the extent of the deformation. This mapping from the frame of reference R to a second frame of reference R', called "intrinsic", may be achieved via a unitary transformation [24] through the Wigner rotation functions for spherical harmonics with λ=2. The transformation may be conveniently chosen so that the axes of the frame of reference R' coincide with the principal axes of the ellipsoid. Another substitution is required to reach a new set of coordinates β, γ, θ_i called the Hill-Wheeler coordinates, in which the subset β, γ defines a two-dimensional polar coordinate system within the five-dimensional quadrupole deformation space, namely:

$$\begin{aligned} &\alpha_{2,0} = \beta cos\gamma \\ &\alpha_{2,1}, \alpha_{2,-1} = 0 \\ &\alpha_{2,-2} = \alpha_{2,2} = \beta sin\gamma \end{aligned} \tag{1.11}$$

The expression of the nuclear shape then reads:

$$R\left(\theta,\phi\right) = R_0\left[1+\beta\sqrt{\frac{5}{16\pi}}\left(cos\gamma(2cos^2\theta-1)+\sqrt{3}sin\gamma sin^2\theta cos2\phi\right)\right] \tag{1.12}$$

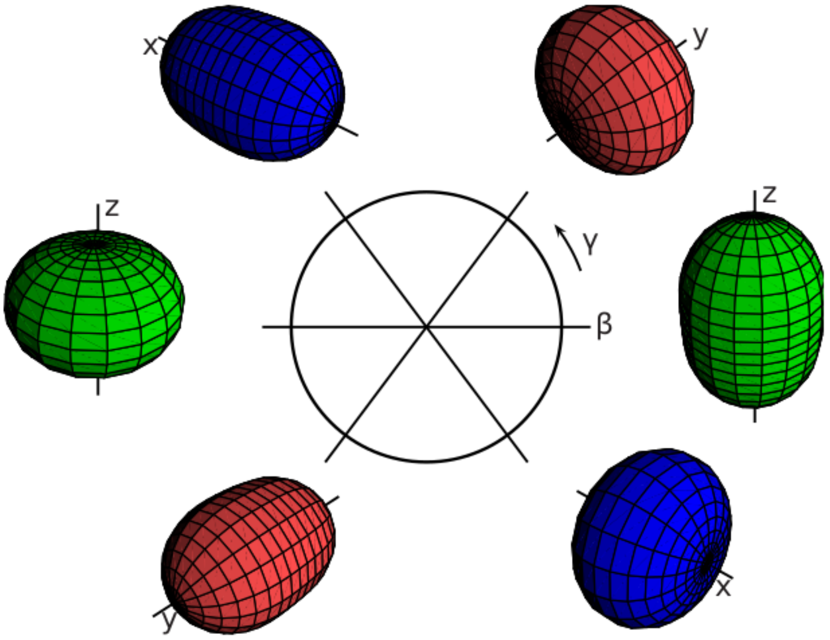

Figure 1.1: Quadrupole deformed shapes as a function of the Hill-Wheeler parameters. Different colors identify the axes of the intrinsic reference frame (green for z, red for y and blue for x). Figure taken from Ref. [24]

The parameter β is related to the magnitude of deformation, while γ is related to the axial symmetry of the system. For instance, $\beta = 0$ (with any γ) corresponds to a spherical shape, while $\beta \neq 0$ and $\gamma = 0$ to an axially symmetric shape. If $\beta \neq 0$, particular cases are:

(a) $\gamma = 0°$, $120°$, $240°$: prolate shape with symmetry axes z,x,y respectively.

(b) $\gamma = 60°$, $180°$, $300°$: oblate shape with symmetry axes y,z,x respectively.

(c) γ different from previous cases: triaxial shapes.

The labeled of the axis being of no physical significance, the interval $0° < \gamma < 60°$ describes all the possible quadrupole deformations. Figure 1.1 shows the different shapes associated with different β and γ values.

For states with $J^{\pi} \neq 0$, a spectroscopic quadrupole moment Q_s is conventionally defined by:

$$Q_s\left(J\right) = \sqrt{\frac{16\pi}{5}} \frac{\langle JJ20|JJ\rangle}{\sqrt{2J+1}} \langle J\left|\left|E2\right|\right|J\rangle \tag{1.13}$$

where $\langle JJ20|JJ\rangle$ is the Clebsch-Gordan coefficient. It is related to the mass distribution and it provides an estimate of non-sphericity of the nucleus in a given excited state.

1.2 Nuclear Models

1.2.1 Shell Model

The nuclear Shell Model (SM) has been developed since the early fifties to the present days. Within this model, the complexity of the many-body problem is greatly reduced by the empirical evidence for shell structure in nuclei. The system is approximated to an inert core composed of closed shells (doubly magic nucleus), which are filled up with neutrons and protons paired to angular momentum J = 0, plus a certain number of "valence" nucleons outside the magic shells that are constrained to move in a truncated Hilbert space, the so-called "model space". The SM Hamiltonian, acting only between the valence particles, should account for the neglected degrees of freedom, namely those of the core particles as well as of the excitations of valence particles above the chosen model space. In the nuclear shell model [12] the wave function of the nucleons is described as the solution of the Schrödinger equation:

$$H|\Psi\rangle = E|\Psi\rangle \tag{1.14}$$

with the Hamiltonian operator:

$$H = \sum_{i=1}^{A} T_i + \sum_{i,j=1 \;\; i<j}^{A} V_{ij}^{(2)} + \sum_{i,j,k=1 \;\; i<j<k}^{A} V_{ijk}^{(3)} \tag{1.15}$$

where T_i is the kinetic energy of the i^{th} particle and V_{ij} is the two-body interaction potential between the particles i and j. The summations extend to all the nucleons and only two-body $V^{(2)}$ and three-body $V^{(3)}$ interactions are considered. The $V^{(3)}$ terms have been usually neglected in the past; however, in modern SM calculations also three-body interactions V_{ijk} are included such as the phenomenological interactions characterized by many parameters fitted to the experimental data (the Gogny [8] and Skyrme [59] forces are two of the most used to date). One of the common approaches used to solve the Schrödinger equation of the atomic nucleus is the description of the motion of a single nucleon in a mean potential generated by all the others. This can be achieved by adding and subtracting an auxiliary one-body potential U to the Hamiltonian of the system. Considering, for simplicity, only the two-body interactions:

$$H = \left[\sum_{i=1}^{A} T_i + \sum_{i=1}^{A} U_i\right] + \left[\sum_{i,j=1 \;\; i<j}^{A} V_{ij}^{(2)} - \sum_{i=1}^{A} U_i\right] \equiv H_0 + H_{res} \tag{1.16}$$

in this way the Hamiltonian is decomposed in two terms, one which describes the independent motion of the nucleons (H_0) and a residual interaction which is usually small compared with the first term (H_{res}). The nucleons can be thus considered as independent particles in a common mean field, while H_{res} can be treated as a perturbation.

In the SM one first assumes a single particle potential generated by the inert core as:

$$V_i = V_c(r) + V_l + V_{ls}(r) \tag{1.17}$$

consisting of an attractive central Harmonic-Oscillator potential, the angular momentum term ($V_l \propto l^2$) and the spin-orbit term ($V_{ls} \propto l \cdot s$). Using this potential the experimental magic number are reproduced as shown in Fig. 1.2. The valence nucleons are than subject to the residual interaction H_{res}.

Although the modern shell models show detailed and precise descriptions of many nuclear properties, severe computational difficulties arise when dealing with the increasing number of valence particles in large model spaces. The Monte Carlo calculation techniques have been applied in recent years (Monte Carlo Shell Model), to extend the model to the description of heavy nuclei. Significant progress has been made within the realistic SM framework in the last three decades and a number of calculations have been performed using various Nucleon-Nucleon potentials.

1.2.2 Collective Models

Nuclei can undergo collective oscillations around an equilibrium shape. For simplicity, only vibrational oscillations are considered (around a spherical shape) that do not alter the volume and nuclear density. In this way, the vibrational motion stands out clearly, without complications due to rotation. The vibrational motion can be described as boson excitations (phonons) that carry the intrinsic angular momentum λ. The $\lambda = 2$ mode describes a quadrupole oscillation of the nucleus, where it changes its shape back and forth, from spherical to prolate, back to spherical and then to oblate, and then back again to spherical. This corresponds to the lowest energy and most common oscillation mode.

The typical quadrupole-phonon vibrational spectrum built on the ground state is characterized by a 0^+ ground state, one-phonon 2^+ state, two-phonon triplet 4^+, 2^+ and 0^+ states with twice the energy of the first 2^+ level and three-phonon quintuplet 6^+, 4^+, 3^+, 2^+ and 0^+ states with three times the energy of the first 2^+ level. Besides level excitation energies, the vibrational model provides selection rules and predicts intensity ratios between several E2 transitions. The selection rule for E2 transitions is $\Delta N_{ph} = \pm 1$, where N_{ph} is the number of phonons. Considering the magnitude of the allowed reduced transition probabilities B(E2), it is proportional to the N_{ph} in the initial state of the decay. For example, the B(E2) values for the transitions between states with N_{ph}=2 and N_{ph}=1 is twice the B(E2) value for the N_{ph}=1 and ground state. For the $N_{ph} \geq 3$, the proportionality of the B(E2) values to the number of phonons in the initial state actually refers to the sum of the B(E2) values from a given N_{ph}-phonon level to all the $(N_{ph} - 1)$-phonon levels allowed by the angular momentum conservation.

The existence of a deformed shape of the nucleus opens the possibility of nuclear rotation. These are characterized by a rotational angular momentum $\vec{R}$, which, in the case of axially-symmetric nuclei, is perpendicular to the symmetry axis. The rotational energy is given by:

$$E_{rot} = \frac{\hbar^2}{2I}\vec{R}^2 = \frac{\hbar^2}{2I}(\vec{J} - \vec{j})^2 \tag{1.18}$$

where I is the moment of inertia, $\vec{J} = \vec{R} + \vec{j}$ is the total angular momentum and $\vec{j}$ represents the intrinsic angular momentum. If we assume that the ground state is $J^\pi = 0^+$ and if the angular momentum can all be ascribed to rotation (as is normally true for the low- lying, low-spin, positive parity states in deformed even-even nuclei) then $\vec{J} = \vec{R}$ and the symmetric rotational energy is:

$$E_{rot}(J) = \frac{\hbar^2}{2I}J(J+1) \tag{1.19}$$

where only even J are allowed since the form of the wavefunction must be invariant under reflection over a plane perpendicular to the symmetry axis. The excitation energy

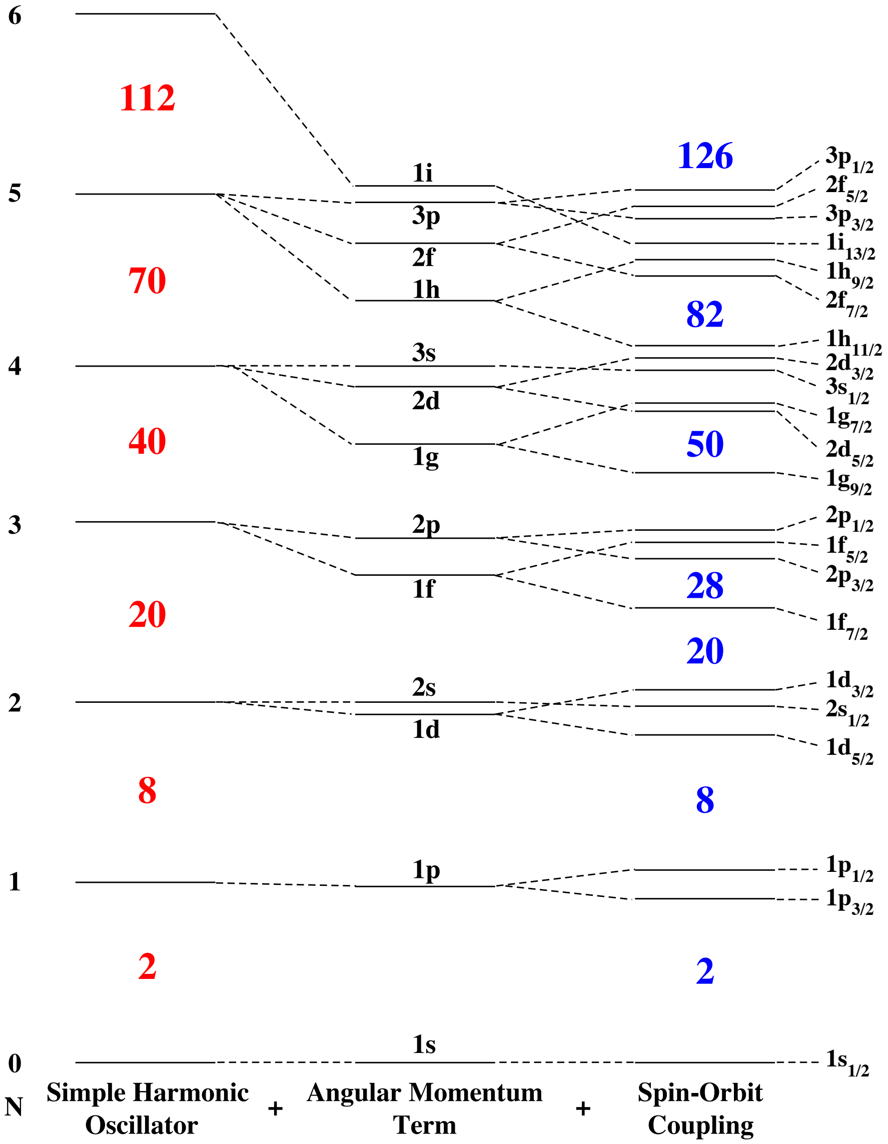

Figure 1.2: Schematic diagram of single-particle energy levels for spherical shell model. The break of degeneracy caused by the angular momentum and spin-orbit terms, which produces the emergence of the magic number in the shell closure, is also visible. The energy values in the first set are the ones of the simple harmonic oscillator. Figure taken from [58].

for the first three states belonging to the band built on the 0^+ ground state are:

$$\begin{aligned} E_{2_1^+} &= 6\frac{\hbar^2}{2I} \\ E_{4_1^+} &= 20\frac{\hbar^2}{2I} \\ E_{6_1^+} &= 42\frac{\hbar^2}{2I} \end{aligned} \tag{1.20}$$

Thus the energy ratio $E_{4_1^+}/E_{2_1^+}$=3.33. This simple formula is one of the most famous results of the rotational model and still remains one of the best signatures for rotational motion and deformation [11].

The scenario is different when the nuclear rotational motion is superimposed on intrinsic excitations, like those induced by a collective vibration. Each intrinsic excitation carries an intrinsic angular moment j, which has a given projection Ω on the symmetry axis. The projection of the total angular momentum J along the symmetry axis, denoted by K, is the same as that of the intrinsic excitation. If the intrinsic excitation characterized by projection $\Omega = K$ different from 0, the total angular momentum can take on values $J = K, K+1, K+2, ...$ Thus the rotational energies, relative to the "base" energy of the intrinsic excitation, becomes [12]:

$$E_{rot}(J) = \frac{\hbar^2}{2I}[J(J+1) + E_K] \tag{1.21}$$

where E_K is a constant that involves the projection K and quantities related to the intrinsic part of the wave function.

The most common low-lying vibrational excitation in deformed nuclei are quadrupole vibrations, similarly to the fact that the most common deformation in nuclei is quadrupolar. In particular, oscillations along the β parameter correspond to K=0 and are referred to as β- vibrations. The vibration is aligned along the symmetry axis and therefore preserves axial symmetry. In the case of K = 2 mode, the vibration occurs along the γ degree of freedom (γ-vibrations) and thus the axial symmetry is instantaneously broken. As a consequence, an axially symmetric deformed nucleus could be characterized by a ground state band, a β rotational band ($K = 0$) build on a 0^+ excited states and a γ rotational band ($K = 2$) built on a 2^+ state. An example of nuclei which exhibit rotational bands is reported in Fig. 1.3. States belonging to a β or γ rotational bands can decay, by E2 radiation to the ground state band, but transitions between β and γ vibrational bands are forbidden, since they involve the simultaneous destruction of one vibration and creation of another. The values of the B(E2) values expected for the allowed transitions are summarized by the Alaga rules. [12].

1.2.3 Interacting Boson Model

The Interactic Boson Model (IBM) is an algebraic model based on group theory to reproduce collective nuclear properties. The major assumptions of this model are:

- Closed shells of either protons or neutrons, and excitations out of them, are neglected. The structure of the low-lying excited states in the even-even nuclei depends only on the valence nucleons.
- The valence nucleons are treated in pairs. The collective properties of a nucleus are described in terms of a system of bosons, made of pairs of identical nucleons

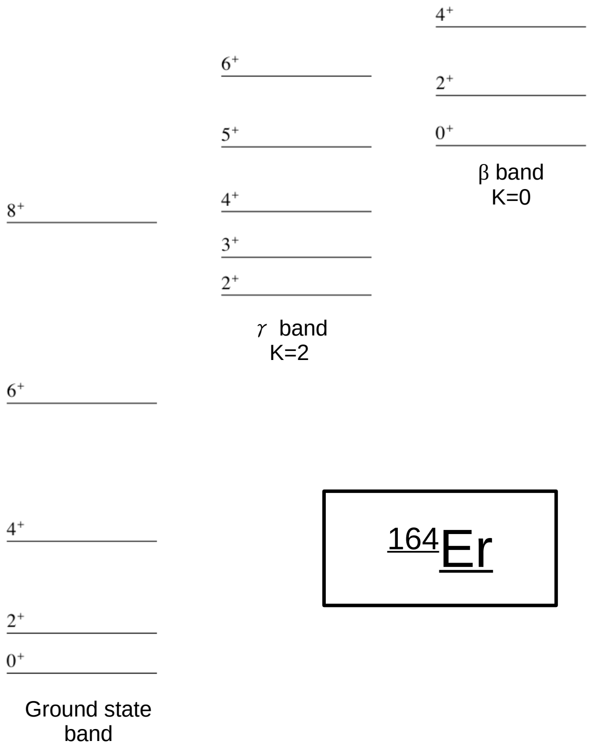

Figure 1.3: Partial level scheme of deformed ^{164}Er nucleus. The ground state, β, and γ bands are labeled.

that can be coupled to total angular momentum $J = 0$ (s-boson) or $J = 2$ (d-boson), which interact with one another via one- or two-body interactions. The number of bosons is half the number of valence protons and neutrons, both of which are always counted to the nearest proton and neutron closed shells. This counting rule generates a finite, fixed, number of s and d bosons.

- The number of bosons is equal to the number of pairs of particles outside the closed shell. If, however, the major shell is more than half filled one should count the number of hole-pairs.

The original version of the model (IBM-1) considers only one type of bosons (s,d), without the distinction between proton and neutron bosons. The Hamiltonian for a system of s and d bosons that conserves the total number of bosons can be expressed in terms of the boson creation operators $(s^{\dagger}, d^{\dagger}_{\mu})$ and annihilation operators (s, d_{μ}), $(\mu = 0 \pm 1 \pm 2)$. The distinction between proton and neutron bosons (s$_{\pi}$, d$_{\pi}$, s$_{\nu}$, d$_{\nu}$) has been implemented in the next version of the model (IBM-2) [33].

Since an s boson (J = 0) has only one magnetic substate and a d boson (J = 2) has five, the s-d boson system can be looked at mathematically as a six dimensional space. The basis states span that space. It turns out that such a system can be described in terms of the algebraic group structure U(6). Three subgroup chains can be constructed starting from U(6) (where all the states are degenerate for a given number N of bosons), and ending with O(3). The Hamiltonian for any chain is written as a sum over the Casimir operators of the subgroups of the specific chain and is therefore diagonal in a basis defined by the corresponding representation labels. Each step in the chain reduction requires one or more quantum numbers to distinguish the representations of the particular sub-group and breaks a previous degeneracy. The solution of the eigenvalue problem for such a chain reduces to that of the (known) eigenvalues of each of the Casimir operators.

The structure defined by such a Hamiltonian is referred to as a dynamical symmetry. There are three of these symmetries that are physically interesting, known by the labels U(5), SU(3), and O(6). The U(5) symmetry is the IBM version of a vibrator. This limit provides the basis states used in most treatments of the general IBM Hamiltonian. The SU(3) symmetry is the IBM version of a deformed rotor, and the O(6) symmetry is recognized as corresponding to a deformed, axially-asymmetric rotor.

Since transition operators can also often be written in terms of the group generators, transition selection rules also appear naturally, and the rates for allowed transitions can be written analytically.

The most important aspect of IBM approach is that the total number of bosons is a conserved, finite number. As a consequence the set of boson states that span the model space is finite, which makes it possible to represent the Hamiltonian as a finite matrix. The eigenvalues and eigenvectors can be obtained by making a full diagonalization using numerical methods. Once the eigenvectors are obtained, other properties as, for example, electromagnetic transition probabilities are calculated by evaluating the matrix elements of the appropriate operator between the eigenvectors. In this thesis, the results of the experimental analysis have been compared with the calculation performed in the framework of IBM. The matrix elements are calculated thanks to NPBOS code [52]. The NPBOS is an open source code developed by T. Otsuka in 1976 with the aim to extract energy levels, wave functions, and electromagnetic matrix elements within the IBM-2 framework. In order to perform the diagonalization of the Hamiltonian (see Eq. A.13) the code requires as input the properties of the nucleus of interest (mass number, number of proton and neutron bosons and the experimental energy levels) and the boson Hamiltonian parameters: $\epsilon, \kappa, \chi_\pi, \chi_\nu, c_L, \xi_1, \xi_2, \xi_3$ (see Appendix A for more details).

1.3 Shape Coexistence in nuclei

In nuclei along the nuclear chart the coexistence of states with the same angular momentum and parity, but with different deformations can be found. This phenomenon is known as shape coexistence and it is thought to occur in nearly all nuclei. One of the most prominent examples of shape coexistence is given by the Pb isotopes at the closed shell Z = 82. In moderately neutron-deficient lead isotopes (with $N > 106$) oblate-deformed structures coexist with spherical states, while for $N \leq 106$ a coexistence between prolate deformed bands and spherical states occur [5]. The lowest three 0^+ states in the energy spectrum of ^{186}Pb have spherical, oblate and prolate shapes [3]. The calculated nuclear potential energy surface is displayed in Fig. 1.4. Next to the spherical minimum corresponding to the ground state, an oblate and a prolate minimum at excitation energies around 1 MeV are located.

Nuclear theory uses two main approaches to describe this phenomenon. The first one is via microscopic shell models [13], while the second one via mean-field models [65]. In the first approach, multiple particle-hole excitations across closed shells are supposed to be the origin of collective nuclear excitations, which become manifested in the form of 0^+ states at low excitation energy. In the second approach, the ground state energy of the nuclear system is calculated through constrained Hartree-Fock methods [7]. The

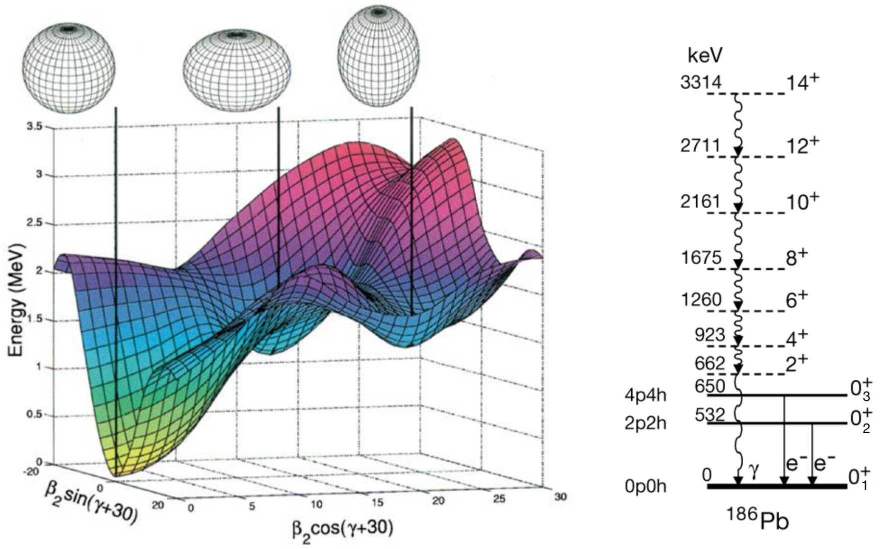

Figure 1.4: The calculated potential energy surface and the partial level scheme of ^{186}Pb are reported. The lowest three states are 0^+ states with spherical, prolate and oblate shape. β_2 is the deformation parameter, $\gamma = 0°$ corresponds to a prolate shape, while $\gamma = 60°$ describes an oblate shape [3].

constraint is set by requiring the nuclear density to assume a certain low-multipole deformation, and then sampling the deformation space.

However, at the moment universal description of this phenomenon is missing. A complete description would require the knowledge of the nucleon-nucleon interaction and the inclusion of every possible nucleon-nucleon correlations as a function of the excitation energy.

From the experimental point of view the nuclear deformation, hence of shape coexistence, can be studied in Coulomb excitation experiments that permit to obtain the E2 matrix elements, and hence the spectroscopic quadrupole moment. Strengths of electric monopole (E0) transitions are also accounted as indicators of shape coexistence since they depend on the mixing of intrinsic configurations with different deformations. E0 transitions and their strength will be discussed in detail in the next Chapter.

2. Electron Spectroscopy

2.1 Internal Conversion Electron

In the de-excitation of nuclear states, a competitive process of the well known γ-ray emission is the internal conversion one. In this case, the electromagnetic interaction is between the nucleus and its orbiting electrons. Excited nucleus interacts with electrons in the atomic orbits that are ejected from the atom with a kinetic energy equal to the difference between the nuclear transition energy and the binding energy of the relevant electron shell. Most of the internal conversion electrons (ICE) are ejected from the K shell since they have the maximum probability to be closer to the nucleus, but also electrons from L, M, N shells could be ejected. The electron binding energy B_e depends on Z and varies with the atomic shell considered. Hence, electron conversion can be used as a fingerprint to identify which is the element of origin, and conversion electrons emitted from different atomic shells of a nucleus will have a different kinetic energy. A conversion electron spectrum will thus present multiple discrete peaks corresponding to a certain nuclear transition, in contrast with a γ-ray spectrum, where only one peak corresponds to each nuclear transition. The internal conversion coefficient α is given by:

$$\alpha = \frac{\lambda_e}{\lambda_\gamma} \tag{2.1}$$

where λ_e is the total decay constant of ICE from all shells ($\lambda_e = \lambda_{eK}+\lambda_{eL}+\lambda_{eM}+\lambda_{eM}+...$) and λ_γ is the decay constant for the γ-ray emission. The possibility of internal e^+-e^- creation in a $0^+ \rightarrow 0^+$ nuclear transition is here neglected. The decay constant of a nuclear state λ_t is defined as:

$$\lambda_t = \lambda_\gamma + \lambda_e = \lambda_\gamma(1+\alpha) \tag{2.2}$$

The contribution to the ICE from different shells can be made explicit by the equivalent expression for λ_t (in a obvious notation):

$$\lambda_t = \lambda_\gamma(1 + \alpha_K + \alpha_M + \alpha_L + \alpha_N + ...) \tag{2.3}$$

The internal conversion coefficients for different atomic shells could be calculated using relativistic electron wave functions, taking into account the finite nuclear size (see Ref. [9]). A simple and accurate analytic approximation to the general formula of α for electric (EL) and magnetic (ML) transitions of order L are given by:

$$\alpha(EL) \cong \frac{Z^3}{n^3}\left(\frac{L}{L+1}\right)\left(\frac{e^2}{\hbar c}\right)^4\left(\frac{2m_ec^2}{E}\right)^{L+\frac{5}{2}} \tag{2.4}$$

$$\alpha(ML) \cong \frac{Z^3}{n^3}\left(\frac{e^2}{\hbar c}\right)^4\left(\frac{2m_ec^2}{E}\right)^{L+\frac{3}{2}} \tag{2.5}$$

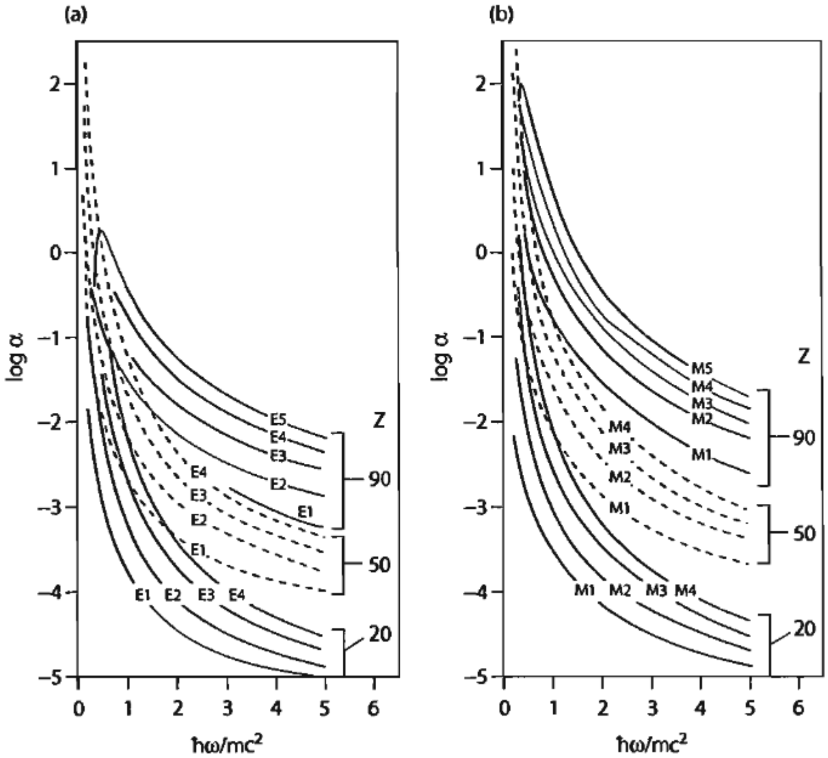

Figure 2.1: Internal conversion coefficients of K shell for electric (a) and magnetic (b) transitions in Ca, Sn e Th elements. Figure adapted from Ref. [9]

where Z is the atomic number, n is the main quantum number (n=1 for K shell, n=2 for L shell, etc.) and E is the energy of the nuclear transition equal to the difference between initial and final levels. From Eq. 2.4, 2.5 many properties are revealed:

- $\alpha \propto Z^3$: internal conversion process is favoured in heavy nuclei.
- $\alpha \propto n^{-3}$: internal conversion electrons from the internal atomic shells are ejected preferentially.
- $\alpha \propto E^{-L}$: internal conversion probability increases for high multipolarity and for small de-excitation energy.

Using Eq. 2.4, 2.5 α_K have been calculated and tabulated for different combinations of Z, E and multipolarities for electric and magnetic transitions [37]. The calculated α_K coefficient are shown in Fig. 2.1. These results are sufficiently reliable and can be used with confidence in the interpretation of experimental data. The experimental values α_K could be compared with the calculated ones to obtain, for example, the character (E or M) and the multipolarity of a transition. In this way, it is possible to determine the relative parity between the initial and final states connected by the transition.

2.2 Electric Monopole Transitions

If the transition of interest is between two states with the same angular momentum and parity (J^π) also electric monopole transitions (E0) are allowed. Due to the intrinsic angular momentum of the single photon, γ-ray emission of this multipole order is strictly forbidden, and the transition proceeds only via internal conversion, by transferring energy, zero units of angular momentum, and no parity change to an atomic electron ($\Delta I = 0$).

The transition from an initial state Ψ_i to a final state Ψ_f can be expressed by the monopole matrix element M(E0):

$$M(E0) = \langle \Psi_f | T(E0) | \Psi_i \rangle \tag{2.6}$$

where T(E0) is the monopole operator. M(E0) is sensitive to the changes in the nuclear charge-square radii since the T(E0) operator is (in a single particle model):

$$T(E0) = \sum_k e\, r_k^2 \tag{2.7}$$

where the sum is over the Z protons in the nucleus, e is the unit of electrical charge and r_k is the radial position of the k^{th} proton. The monopole matrix element M(E0) is related to the dimensionless quantity ρ^2 which is the monopole transition strength [34], defined as:

$$\rho^2 = \mid \frac{M(E0)}{eR^2} \mid^2 \tag{2.8}$$

where R is the nuclear radius ($R \simeq 1.2A^{1/3}$ fm). Electric monopole transitions are determined by a change in the radial distribution of the electric charge inside the nucleus and a high E0 strength is expected whenever configurations characterized by different mean-square charge radii mix. In this sense, an enhancement of the monopole strength in transitions between states with $\Delta J = 0$ may be considered as a signature for shape coexistence [32].

The E0 transition probability as a function of ρ^2 is given by:

$$W(E0) = \frac{1}{\tau(E0)} = \rho^2 \times [\Omega_{IC} + \Omega_{IP}] \tag{2.9}$$

where $\tau(E0)$ is the partial mean life of the initial state for E0 decay. The quantities Ω_{IC} and Ω_{IP} are the electronic factors for internal-conversion electron and electron–positron pair emission (defined in Ref. [14]), respectively. Ω_i depends on the nuclear charge Z and the transition energy E, they can be calculated using the LISE++ [45] program or Bricc database [37].

Some of the ratio of Ω_K (the most relevant term of Ω_{IC}) and Ω_{IP} reported in Ref. [22] is shown in Table 2.1. In the third and fourth columns, the experimental ratios and the theoretical ones are reported. As it can be noted for the mass number A larger than 90 and for energies less than 2 MeV (as in the case of the present work with A=106 and energies of interest < 2 MeV), the internal conversion process prevails over the pair emission. Since it is the conversion electrons from the atomic shell K that give rise to the most intense transitions, usually the transition probability by internal conversion from the orbital K is:

$$W_K(E0) = \rho^2 \times \Omega_K \tag{2.10}$$

2.3 Two-level Mixing Model

Nuclear states are complex admixtures of many components, and the determination of the corresponding wave function and eigenvalues must involve the diagonalization

Table 2.1: Experimental data and theoretical values of K-shell electron to internal pair conversion probability ratios for E0 transitions from Ref. [22]

		$\Omega_K(E0)/\Omega_{IP}(E0)$		
Nucleus	E_γ [keV]	Experiment		Theory
^{42}Ca	1837	0.111(22)	[40]	0.133
^{64}Zn	1910	0.46(7)	[53]	0.475
^{90}Zr	1761	2.38(8)	[50]	2.48
^{140}Ce	1904	< 6.3	[4]	7.23

of a large Hamiltonian matrix. In Ref. [12] the author demonstrates that in many cases, one can simulate the full diagonalization reasonably well using sequences of a few two-state mixing calculations. Fig. 2.2 reported a simple case of arbitrary perturbation V which mixes the basis states changing their initial energies. The intrinsic (unperturbed) configurations with energies E$_1$ and E$_2$ and deformations β_1 and β_2 with a transition energy ΔE$_u$ are described by the wave functions ϕ_1 and ϕ_2 (see Fig. 2.2). The perturbed configurations are described by the energies E$_I$ with E$_{II}$ with a transition energy ΔE$_p$ and wave functions Φ_I and Φ_{II}. The perturbed wave functions depend on the unperturbed ones via the mixing amplitude a as:

$$\Phi_I = a^2\phi_1 + b^2\phi_2 \quad \Phi_{II} = b^2\phi_2 - a^2\phi_1 \quad (a^2 + b^2 = 1) \tag{2.11}$$

This simple model can be used to describe the mixing of a 0^+_i ground state and an excited 0^+_f state, each characterized by a given value of the quadrupole deformation parameters β and γ (see Ref. [34]). The 0^+_f and 0^+_i states are assumed to be a linear combination of two basic configurations $|1\rangle$ and $|2\rangle$ of different deformations:

$$|0^+_i\rangle = b|1\rangle + a|2\rangle \quad |0^+_f\rangle = a|1\rangle - b|2\rangle \tag{2.12}$$

Using the definition in Eq. 2.8, the ρ^2_{fi} value can be write as:

$$\rho^2_{fi} = \frac{1}{e^2R^4}[ab(\langle 1|T(E0)|1\rangle - \langle 2|T(E0)|2\rangle) - (a^2 - b^2)\langle 2|T(E0)|1\rangle]^2 \tag{2.13}$$

Let’s assume that the mixing among the different shape configurations is weak. The first two terms in Eq. 2.13 will thus be negligible, since $ab << 1$. The third term will be negligible as well since in the case of well distinct shape configurations, it will imply that $\langle 2|T(E0)|1\rangle \sim 0$ given the different localization of the 1 and 2 wavefunctions in the deformation space. Therefore, in the case of weak mixing among configurations with different shapes $\rho^2 \sim 0$.

Consider now a strong mixing scenario, where $|a| = |b| = 1/\sqrt{2}$. The third term in Eq. 2.13 cancels and the E0 strength becomes:

$$\rho^2_{fi} = \frac{1}{e^2R^4}[\frac{1}{2}(\langle 1|T(E0)|1\rangle - \langle 2|T(E0)|2\rangle)]^2 \tag{2.14}$$

Since the monopole operator is directly connected to the nuclear mean squared radii (see Eq. 2.7), the monopole strength in this approximation is proportional to the difference in the mean square radii of the configurations.

This simple model illustrates how a large ρ^2 can be a remarkable indicator of a shape difference in the two mixing states, or a large amount of configuration mixing, or both

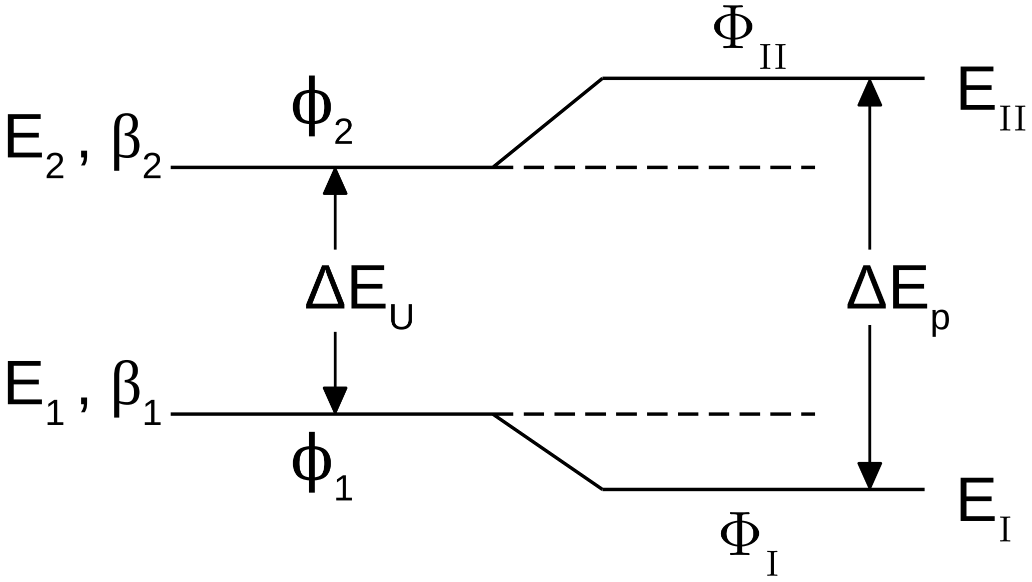

Figure 2.2: Schematic illustration of the simplifying two-level mixing model of two states interacting with each other. The unperturbed is described by the energy $E_{1,2}$ deformations $\beta_{1,2}$ and wave functions $\phi_{1,2}$. The unperturbed transition energy is given by ΔE_u. The perturbed system is described by the energies $E_{I,II}$ and wave functions $\Phi_{I,II}$. In this model the unperturbed and perturbed wave functions are linked by the mixing amplitude a.

the effects. This model has been used, for example, to effectively describe the large ρ^2 value measured for the $0_3^+ \to 0_2^+$ in ^{96}Sr ($\rho^2_{exp}(0_3^+ \to 0_2^+) \cdot 10^3 = 185(50)$) [34].

It is possible to deduce an approximate expression of ρ^2 in terms of the β and γ deformation parameters of the unmixed states [21]:

$$\begin{aligned} \rho^2(0_2^+ \to 0_1^+) = (\frac{3Z}{4\pi})^2 a^2(1-a^2)[(\beta_1^2 - \beta_2^2) \\ + \frac{5\sqrt{5}}{21\sqrt{\pi}}(\beta_1^3 cos3\gamma_1 - \beta_2^3 cos3\gamma_2)]^2 \end{aligned} \tag{2.15}$$

where β_1, γ_1 and β_2, γ_2 are the deformation parameters of the unmixed states. The value of mixing amplitude a starting from the experimental monopole strength $\rho^2(0_2^+ \to 0_1^+)$ in ^{106}Pd has been calculated in Sec. 5.2.1

2.4 Experimental Techniques

In order to extract the α_K and the ρ^2 values, it is needed to measure the energy spectra of both internal conversion electrons and γ-rays. Spectrometers for ICE measurement are typically a combination of Si(Li) detector to detect the ICE coupled with a device for electron transportation. An array of HPGe detectors is used to detect the γ-rays emitted in the de-excitation of the excited states of the nuclei under investigation [49].

An experimental setup of this kind allows to determine the quantity q^2_{ifj}(E0/E2), defined as the ratio between the transition probabilities $W_K(E0)$ and $W_K(E2)$:

$$q^2_{ifk} = \frac{W_K(E0; J_i^+ \rightarrow J_f^+)}{W_K(E2; J_i^+ \rightarrow J_k^+)} = \frac{I_K(E0; J_i^+ \rightarrow J_f^+)}{I_K(E2; J_i^+ \rightarrow J_k^+)} \cdot \frac{\epsilon_e(E2)}{\epsilon_e(E0)} \tag{2.16}$$

where I_K are the intensities for the K internal conversion electrons from the $E0(J_i^+ \rightarrow J_f^+)$ transition and an $E2(J_i^+ \rightarrow J_j^+)$ transition from the same initial level to a J = 2 final state (usually the 2_1^+, see Fig. 2.3). Here, $\epsilon_e(\omega L)$ is the efficiency of the electron detector.

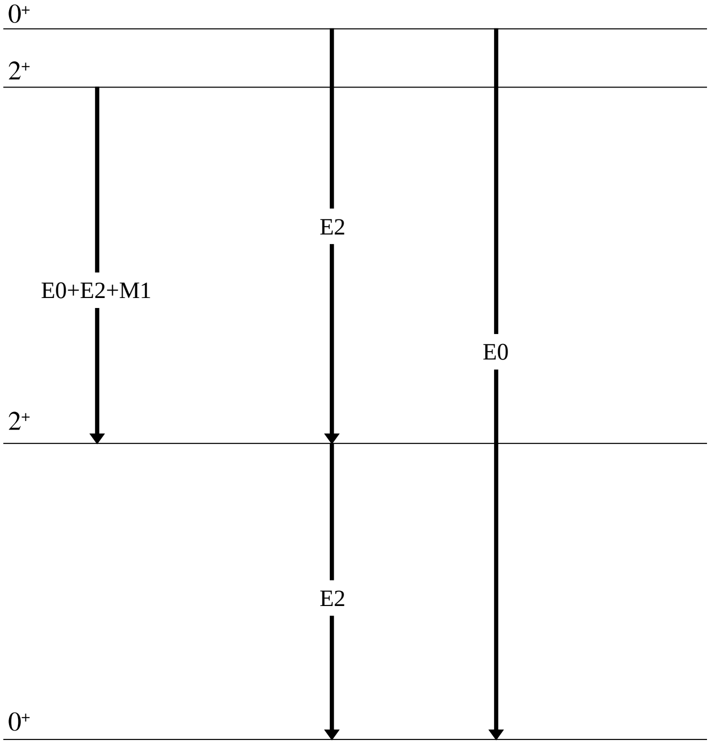

Figure 2.3: Example of possible low-spin states in a even-even nucleus. The allowed multipolarities for each transition are reported on the arrow.

The E0 transition probability $W_K(E0)$ can be then expressed as:

$$W_K(E0; J_i^+ \rightarrow J_f^+) = q^2_{ifk}\ \alpha_K(E2)\ W_\gamma(E2; J_i^+ \rightarrow J_k^+) \tag{2.17}$$

and it can be derived from the measure of $\alpha_K(E2)$, q^2, and W_γ.

According to the definition of α in Eq. 2.1 the experimental value of the K internal conversion coefficient can be obtained as:

$$\alpha^{exp} = \frac{I_K(J_i^+ \rightarrow J_f^+)}{I_\gamma(J_i^+ \rightarrow J_k^+)} \cdot \frac{\epsilon_\gamma}{\epsilon_e} \tag{2.18}$$

where I$_K$ and I$_\gamma$ represent the number of counts detected in the ICE and γ-ray energy spectra, respectively. While ϵ_e and ϵ_γ are the efficiencies of electron and γ-rays detectors, respectively.

The procedure to determine q^2_{ifj} depends on the value of the spin J:

- if the $E0$ transition connects states with $J_i^+ = J_f^+ = 0^+$, q_{ifj}^2 can be directly measured from the intensities of the K conversion electron lines corresponding to the E0 and E2 transitions in the spectra.

- if the $E0$ transition connects states with $J_i^+ = J_f^+ \neq 0^+$, the E2 transition connects the same initial and final levels of the E0 one. In this case the experimental value of q_{ifj}^2 can be extracted from the measurement of the K internal conversion coefficient via the expression:

  $$\alpha_K = \frac{\alpha_K^{th}(M1) + (1 + q_{ifj}^2) \cdot \delta^2 \cdot \alpha_K^{th}(E2)}{(1 + \delta^2)} \tag{2.19}$$

  where δ is the (E2/M1) mixing-ratio, and $\alpha_K^{th}(M1)$, $\alpha_K^{th}(E2)$ are the theoretical values of the internal conversion coefficient available on Ref. [37].

The transition probability $W_\gamma(E2; J_i^+ \to J_k^+)$ can be measured directly (e.g. via Coulomb excitation) or derived from the measurement of the lifetime of the initial level and the branching ratios of the transitions that de-excited it. If the transition $E2$ starts from a level $J^\pi \neq 0^+$ it is necessary to measure also the mixing ratio δ^2, to take into account the M1 contribution to the total γ-ray transition probability.

It is then possible to determine the monopole strength ρ^2 using the relation:

$$\rho^2 = \frac{\alpha_K(E2)W_\gamma(E2)}{\Omega_K} \cdot q_K^2(E0/E2) \tag{2.20}$$

obtained by equaling the expressions Eqs. 2.10 and 2.17.

If $W_\gamma(J_i^+ \to J_k^+)$ is not known, what is commonly done is to determine the value of the ratio X(E0/E2) (introduced in Ref. [57]) between the E0 and E2 reduced transition probabilities :

$$X(E0/E2) = \frac{B(E0)}{B(E2)} \tag{2.21}$$

The reduced E0 transition probability, B(E0), is equal to the square of the E0 matrix element, and so from Eq. 2.8:

$$X(E0/E2) = \frac{\rho^2 e^2 R^4}{B(E2)} \tag{2.22}$$

The experimental value of X(E0/E2), considering as usual only K conversion electrons, can be deduced from the formula:

$$X(E0/E2) = 2.54 \times 10^9 \times A^{4/3} \times q_K^2(E0/E2) \times \frac{\alpha_K(E2)}{\Omega_K(E0)} \times E_\gamma^5 \tag{2.23}$$

obtained exploiting the equations:

$$B(E0)(\mathrm{e^2fm^4}) = \quad 2.07A^{4/3}\rho^2 \tag{2.24}$$

$$B(E2)(\mathrm{e^2fm^4}) = \quad 8.16 \cdot 10^{-10} W_\gamma(E2)/E_\gamma^5 \tag{2.25}$$

where E_γ is the E2 γ-ray energy in MeV.

2.5 Structure of the Pd Isotopes

Over recent years extensive works have focused on the properties of lowest-lying excited 0^+ states in nuclei with Z$\sim$ 50 mass region, which lead to a new interpretation of these states in association with shape mixing and shape coexistence phenomenon [34]. The Cd isotopes (Z = 48) located close to the Z = 50 major shell closure have been considered for many years as a "textbook" example of U(5) symmetry in the framework of the IBM [35] based on patterns of excitation energies and transition branching ratios. However, in a systematic study of stable even-mass Cd isotopes, it was concluded that some of these nuclei are poorly described by collective vibrational models [26]. This interpretation opens the question of whether the neighboring Pd isotopes (Z = 46) may actually exhibit a near-harmonic quadrupole vibrational behavior as their excitation energy patterns suggest. The collective properties of stable Pd isotopes have been the focus of detailed experimental and theoretical studies for the past decades. The excitation energy pattern of the low-lying levels in the ^{106}Pd isotope and the B(E2) values normalized to the B(E2; $2^+_1 \rightarrow 0^+_1$) value are reported in Fig. 2.4. As it can be seen the excitation energies might suggest a vibrational structure, with a triplet of states with $J^\pi = 0^+$, 2^+, 4^+ whose energy is approximately twice that of the first 2^+ state. On the other hand, the B(E2) values of transitions from these states to the 2^+_1 put their vibrational character in doubt. The values of the $B(E2; I^\pi \rightarrow 2^+_1)$ for the de-excitations of the two-phonon states (0^+, 2^+, 4^+) should be identical and twice the value of the $B(E2; 2^+_1 \rightarrow 0^+_1)$ one-phonon de-excitation. Instead, as shown in Fig. 2.4, they differ considerably from each other and they are smaller than the expected values of 2. As to the identification of the three-phonon quintuplet, it is made difficult by the presence of additional levels with $J^\pi = 0^+$, 2^+. They have been considered as intruder states resulting from proton-pair excitations across the Z = 50 shell. Two signatures are commonly given for the identification of an intruder states: i) the characteristic V-shape pattern of their excitation energies versus neutron number ii) the enhanced cross section for single- and two-nucleon transfer reactions with respect to those between collective states. Low-lying intruder configurations have been studied in even-even $^{106-116}$Pd isotopes in Refs. [44, 43, 66]. Based on the level energy systematic, the $0^+_3, 2^+_4$ pair of states is suggested to have intruder character until N=60 and again for N=70, while the pair $0^+_2, 2^+_3$ becomes intruder state for N=62, 64. Within this hypothesis, the V-shaped pattern of the excitation energy is granted as shown in Fig. 2.5. The interpretation of the 0^+_3 states as intruder states in ^{104,106}Pd isotopes was also supported in Ref. [29] by the analysis of their decay properties. The only available data of the (^{3}He,n) transfer reaction is an upper limit for the cross section to the 0^+_2 state for the N=58 isotope reported in Ref. [25], much smaller than the ground-state to ground-state cross section in ^{104}Pd and ^{106}Pd.

A detailed analysis of excitation energy patterns and electromagnetic properties of positive-parity levels in even $^{100-116}$Pd was performed some years ago [29] in the framework of the IBM-2 model, which is particularly suitable to study the evolution of an isotopic chain as a function of the neutron number. In that work, all the excitation energies and electromagnetic properties, available at the time for the low-lying levels in the even $^{100-116}$Pd isotopes, were investigated, with the exception of E0 transitions. An analogous study had been also performed by the same authors in the even $^{98-114}$Ru isotopes [30]. Six out of the twelve model parameters were kept fixed for each isotopic chain while the other were requested to vary smoothly along each isotopic chain and among isotones in neighboring isotopic chains. An overall satisfactory agreement was

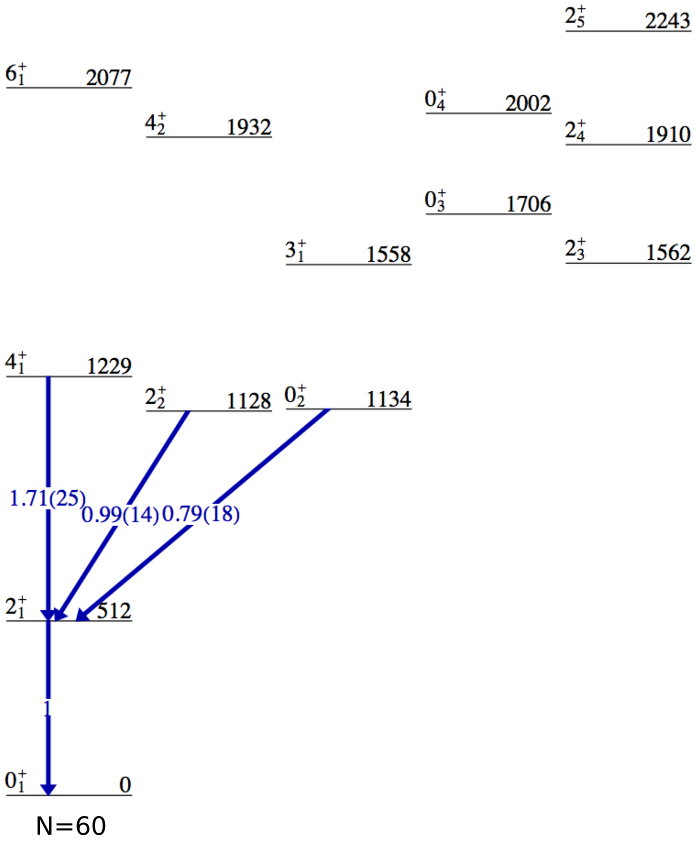

Figure 2.4: Low-lying levels in even-even ^{106}Pd isotope. The B(E2) transition strengths normalized to the B(E2; $2_1^+ \rightarrow 0_1^+$) value are reported on the arrows. Data are taken from Ref. [20].

obtained. The conclusion was that the even palladium isotopes could be considered as lying close to a transitional region between the vibrational U(5) limit to the γ-soft O(6) limit of the IBM-2 model.

More recently a new IBM-2 work has been published [28], which uses the parameters of Ref. [29] to study the large body of new experimental data become available over the years on the even Pd isotopic chain.

An interpretation very different from that of Ref. [29, 28] was given in Ref. [26]. Here, the authors compare the properties of the low-lying levels of $^{102-110}$Pd with the predictions of the harmonic vibrator and it is underlined that in none of the considered Pd isotopes the B(E2) values meet the vibrational requirements. The conclusion is that the harmonic spherical vibrator interpretation breaks down already at the two-phonon levels. In particular, in the ^{106}Pd isotope the author assigns the 0_2^+ state as the head of an intruder shape-coexisting band (in agreement with Ref. [56]) while the 2_5^+ is suggested to be the member of a γ band built on the 0_2^+ state.

The discussion about the collective properties of Pd isotopes is still completely open and no firm conclusions have been reached concerning the level scheme interpretation. The study of collective states must involve not only electromagnetic observable such as B(E2) values and quadrupole moments, which by definition only sample the charge and/or current distributions, but also other electromagnetic probes that are sensitive to shape coexistence and configuration mixing, such as, for instance, the electric monopole transitions.

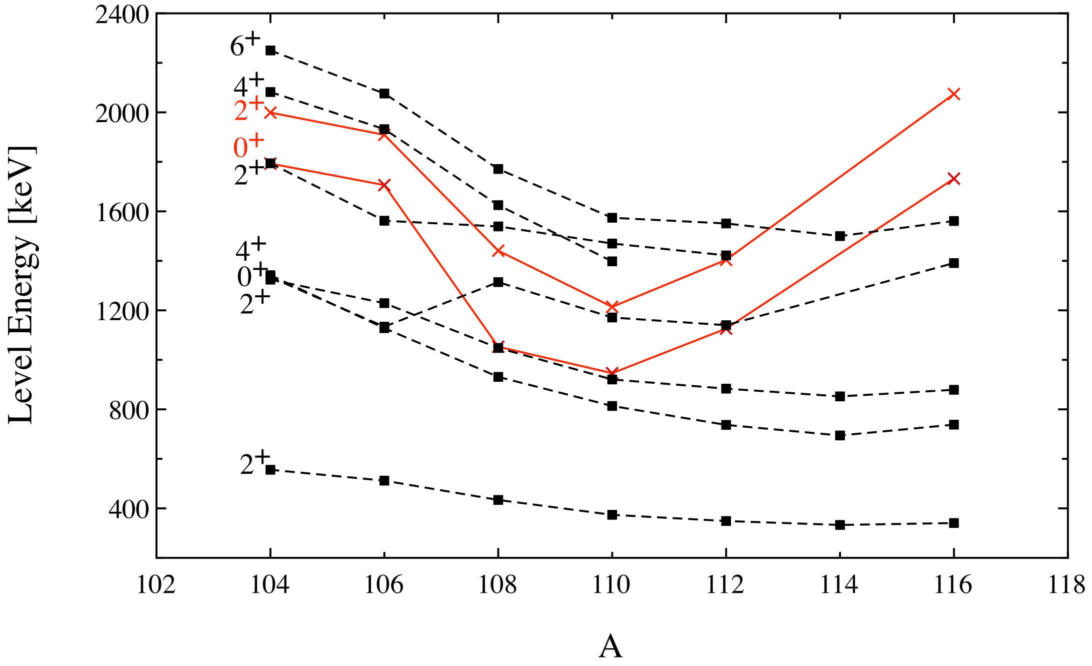

Figure 2.5: Level energy systematics of low spin states in even mass $^{106-116}$Pd isotopes organized into different bands as suggested in Refs. [43, 66]. The intruder-state band is reported in red. See text for more details.

For this reason, the E0 transitions between both 0^+ and 2^+ states in ^{106}Pd have been studied via internal conversion electron spectroscopy, performed by means of an electron spectrometer developed during this PhD work.

From the experimental point of view a Coulomb excitation experiment on ^{106,108}Pd isotopes was performed some years ago by Svensson *et al.* [62], aimed at the measurements of the spectroscopic quadrupole moments in this nuclei. The authors concluded that vibrational degrees of freedom are important for the description of the low-spin level structure of these nuclei but that not all of the observed decay properties can be understood without invoking rotational motion and triaxiality.

The topic of the level vibrational character of the ^{106}Pd isotope has been recently addressed by two neutron inelastic scattering experiments on ^{106}Pd [56, 54]. In the first one, a detailed characterization of the low-lying excited state with spin ≤ 6 was obtained and the level scheme was organized into rotational bands. In the second one, on the basis of previously measured internal conversion electron [16] and new lifetime data, the strengths of E0 transitions between 2^+ states were determined. The authors suggest an interpretation of the level scheme organized into rotational bands and concluded that the extracted monopole strength values provided evidence for shape coexistence between bands having the same K value. However, the existing data on conversion electrons are rather limited and affected by a large uncertainty (for instance, two values differing by a factor $\sim$3 appear in the literature for the internal conversion coefficient of the $2^+_3 \rightarrow 2^+_1$ transition) thus preventing a definite conclusion on the amount of mixing of these two levels. In this thesis, a new measurement of internal conversion electrons in ^{106}Pd is presented, aimed at providing more information on the ρ^2 strengths of $0_i^+ \rightarrow 0_f^+$ and $2_i^+ \rightarrow 2_f^+$ transitions, that are lacking or known with large uncertainty in the literature.

3. The SLICES spectrometer

The Spes Low energy Internal Conversion Electron Spectrometer (SLICES) is the apparatus to perform internal conversion electron measurements designed and implemented during this thesis [47]. The original project was to use SLICES in association with radioactive beams provided by the SPES facility at Legnaro National Laboratory to develop an experimental setup for electron spectroscopy at LNL.

SLICES consists of a large area Si(Li) detector used in conjunction with a magnetic transport and filter system. The large unconventional size of the lens and detector, compared to a traditional mini-orange arrangement [38], will grant a large acceptance in both electron energy and emission angle, ensuring high efficiency of the apparatus. A view of SLICES is reported in Fig. 3.1.

The design of SLICES was based mainly on two existing apparatus for ICE spectroscopy, the Mini Orange Spectrometer (MOS) of the Camerino-Milano collaboration and the SPectrometer for Internal Conversion Electrons (SPICE) installed at TRIUMF (Canada).

The Mini Orange Spectrometer (MOS) is installed at the INFN Laboratori Nazionali del Sud (LNS) in Catania [10]. It consists of a Si(Li) detector 5 mm thick and 500 mm^2 area, placed at 45° with respect to the beam in the backward direction and a set of permanent wedge shaped magnets placed in front of the detector. To grant a good energy resolution, the Si(Li) is cooled to liquid-nitrogen temperature. The magnets are arranged around a photon shield of high-Z material to screen the detector from the γ-ray flux of the target. The magnetic field produced by the permanent magnets has the purpose of filtering in energy and transporting the electrons to the detector. Therefore, the efficiency of the MOS strongly depends on the electron energy. When the levels of interest are populated in the decay of a parent nucleus, a fast switching shutter is used to stop the beam allowing the irradiation of the target at fixed intervals. Data are taken during beam-off intervals. This is a feature also implemented in the SLICES spectrometer. The ICE measurements performed off-beam allow for reduction of the background (coming mainly from δ electrons, X rays and charged particles originated in competing reactions) with respect to the one collected during in-beam measurements.

The SPICE spectrometer is installed at the Isotope Separator and ACcelerator (ISAC) facility at TRIUMF [36]. It consists of an electron detector, a photon shield, and a magnetic lens. A large area annular Si(Li) detector, 6.1 mm thick and 7037 mm^2, is positioned upstream from the target. The central hole of 10 mm diameter allows the radioactive beams delivered from ISAC to reach the reaction target. The detector is segmented into 120 individual segments arranged as 12 azimuthal sectors and 10 rings and it is cooled down by a liquid nitrogen cold-finger to -100°C. The magnetic lens collects and directs electrons emitted from the target position around the photon shield to the electron detector. Also, the efficiency of SPICE is, therefore, strongly energy dependent. The SPICE spectrometer operates in conjunction with the TIGRESS HPGe

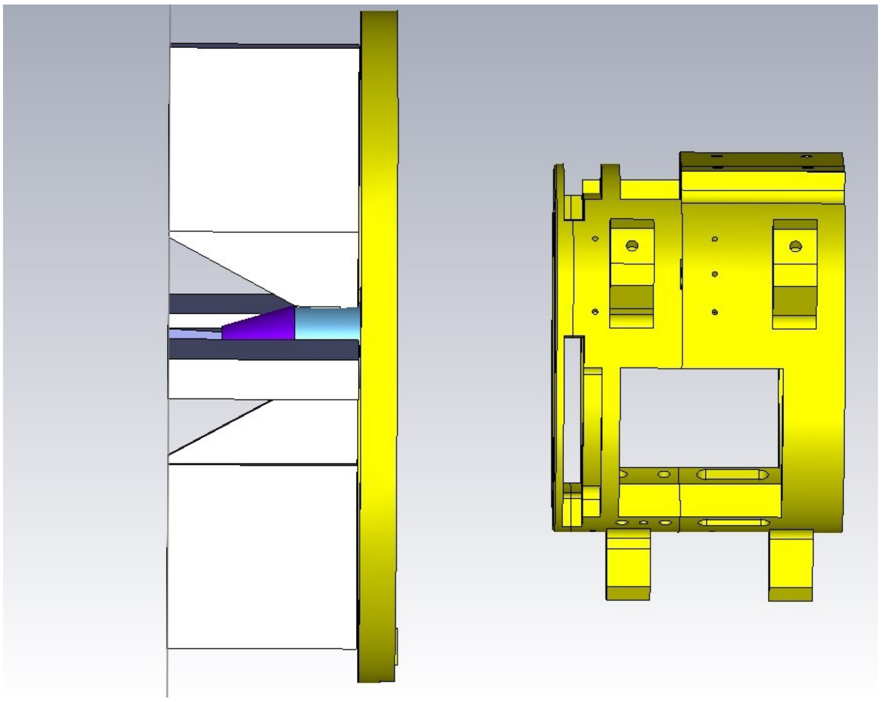

Figure 3.1: View of the SLICES set-up. The magnetic transport system (in the left part of the figure) is positioned in front of the Si(Li) detector (right part of the figure).

clover array to perform in-beam ICE spectroscopy with stable and radioactive beams. The large size and the segmentation of the Si(Li) detector as well as the shape of the magnets were taken as examples in the design of SLICES components.

3.1 SLICES at SPES β-DS

As already said, SLICES has been constructed to perform ICE spectroscopy at the β-decay station of the SPES facility. Here the low-lying non-yrast states of interest will be populated via β/EC decay of a parent nucleus, granting a superior signal to background ratios as compared to typical measurements performed with in-beam reactions.

In the next sections, a brief description of the SPES facility and of the β-decay station will be given. Then the plastic scintillator used to perform β-tagging and the mechanical part of the apparatus will be described.

3.1.1 The SPES facility

SPES is an ISOL (Isotopic Separator OnLine) facility for the production of radioactive beams, currently under construction at INFN LNL. The ISOL method uses light ion beams (or in some cases neutrons, photons) to induce fragmentation, spallation and/or fission in a thick target. SPES uses a primary beam of 40 MeV and 200μA protons directly impinging on seven separate thin discs made of uranium carbide dispersed in graphite (namely UCx, with C/U = 4). The target is kept at high temperature (exceeding 2000 °C) in order to maximize the extraction of the produced species by thermal motion.

The nuclei diffuse in the target material and after that will effuse into an ion source where they are ionized to the 1^+ charge state. Different kinds of ion sources have been developed within the SPES project: i) A surface ion source, in which the ionizer consists of a metal (for example tantalum or tungsten) which has a higher work function than the atom that should be ionized. This source has a good efficiency and selectivity for elements like Rb, Cs, Ba; ii) A plasma ion source, needed to ionize elements with high ionization potential; iii) A laser ion source, which is based on laser induced step-wise resonance photo-ionization. By exploiting the unique electronic structure of different atomic species the laser ion source provides a rapid, efficient, and highly Z selective ionization process.

The ions are swept out of the ion source by an applied voltage, accelerated to 40 kV, and directed into an electro-magnet where they undergo a first separation in mass, reaching about $\Delta M/M \sim 1/200$. At this point the radioactive ions can be sent to the low-energy area for the experiments or directed towards a beam cooler necessary to couple the emittance of the beam to the High Resolution Mass Spectrometer (HRMS), which is under design, to reach a separation of $\Delta M/M \sim 1/20000$. At the exit of the HRMS, the radioactive ions can either be sent back to the low energy area or go towards the post-accelerator. In the last case, the beam is first sent to a charge breeder, necessary to charge up the isotopic species from 1^+ to n^+ charge states. A further medium resolution mass spectrometer is used to clean up the beam from possible contaminants generated in the charge breeder. Finally, the radioactive ions are injected into the superconducting ALPI (Acceleratore Lineare Per Ioni [46]) linac of LNL for post-acceleration up to 10 MeV/A. Beam intensities of 10^7 10^8 particles per second in a wide range of mass ($60 < A < 160$) are expected to be eventually available.

3.1.2 The β-decay station

A β-decay station is envisaged at SPES to study the β-decay of the radioactive ion and the level structure of the child nuclei.

The β-decay station uses the low energy radioactive beams produced by SPES, which are implanted onto a moving tape. After the parent nucleus decays, the tape is moved away in order to minimize background contributions coming from long-living isotopes present as contaminants of the beam or populated in the decay as successors, and a fresh piece of tape is presented to new implantation.

The decay station is primarily composed of two different elements: the tape distributing cassette and two decay chambers as shown in Fig. 3.2. The first decay chamber is located where the beam impinges on the tape, below it the second chamber equipped with the setup for the measurement of conversion electrons, is placed. The distributing cassette is placed at floor level both so that it easy accessible and far from the measurement points. The tape consists of a long plastic Mylar band 38-micron thick and 12.5 mm large, aluminized on one side.

The first decay chamber, at a few millimeters from the implantation point, houses five plastic scintillators arranged in a box configuration, to detect the β particles. Outside the chamber, in a close geometry, are installed five coaxial high-purity Germanium (HPGe) crystals, equipped with anti-Compton shield.

After a collection period, the tape is moved with a velocity of about 2 m/s to the second measurement point: this will be equipped with a plastic scintillator to detect β particles, a coaxial large-volume HPGe crystal, and the electron spectrometer SLICES. The configuration of this measurement point is schematically shown in Fig. 3.3. The

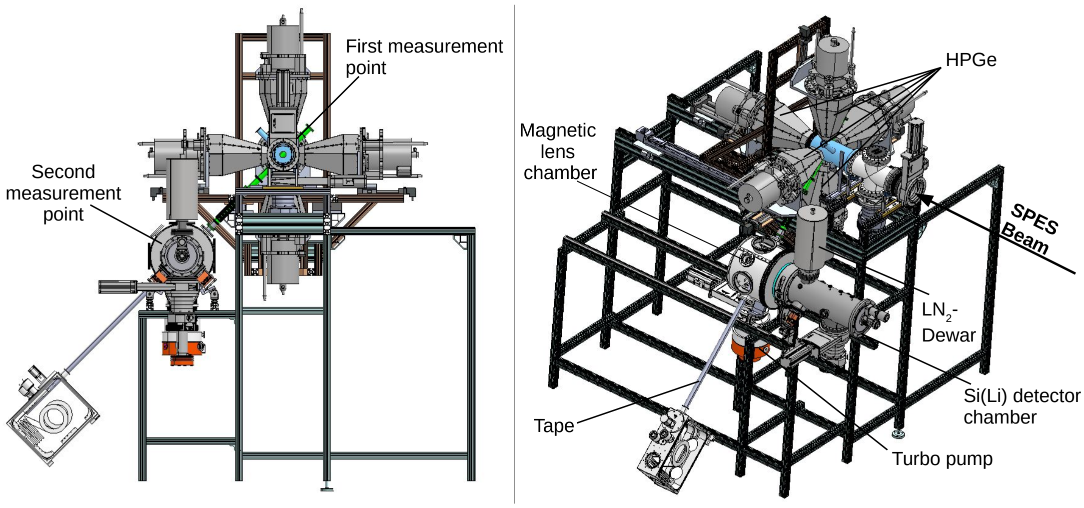

Figure 3.2: Two different cross-sectional views of the β-decay station of the SPES facility at LNL. The main parts of the setup are indicated.

decay chamber (experimental chamber (b) in Fig. 3.3) contains, besides the tape and the plastic scintillator, the magnetic transport system. A second vacuum chamber (experimental chamber (a) in Fig. 3.3) houses a Si(Li) detector together with the cooling and handling system.

3.1.3 Plastic Scintillator

The β-particles emitted in the decay of the parent nucleus can reach the Si(Li), producing a continuous background that deteriorates the final peak-to-total ratio. A large portion of this unwanted contribution in the electron spectra can be removed if the signals of internal conversion electrons in the Si(Li) are acquired requiring a coincidence condition with β-particles emitted in the decay of the parent nucleus. For this reason, a plastic scintillator is positioned in the opposite direction of the SLICES spectrometer with respect to the tape position: when the plastic scintillator detects a β-particle a trigger is sent to the acquisition of the SLICES detector.

The scintillator is positioned close to the collection point, so as to cover the largest solid angle available to allow for the highest efficiency. It is used as a ΔE detector, that, at sufficiently high energies, will only measure a fraction of the electron energy: the main purpose is to give a time response largely independent on the energies of the detected β-particles. The interaction probability for γ radiation in the scintillator has to be close to zero in order to not create misleading trigger signals. Both conditions (independence on β-particle energy and low γ-ray efficiency) were realised by choosing a relatively small thickness of the scintillator.

Prototype detectors have been purchased, based on EJ212 crystals. The thickness of the scintillator is 3 mm since it provides a good compromise between the requirement of a strong signal for good timing response and the need to minimise the γ-ray sensitivity. A detector has been tested with standard electron and γ-ray sources in this work. Signals from the crystals were read out at the corners by 4 SiPM (SiPhotoMultiplier). A schematic view of the detector is shown in Fig. 3.4.

The use of an array of 3×3 mm^2 SiPM, had the advantage of offering a compact

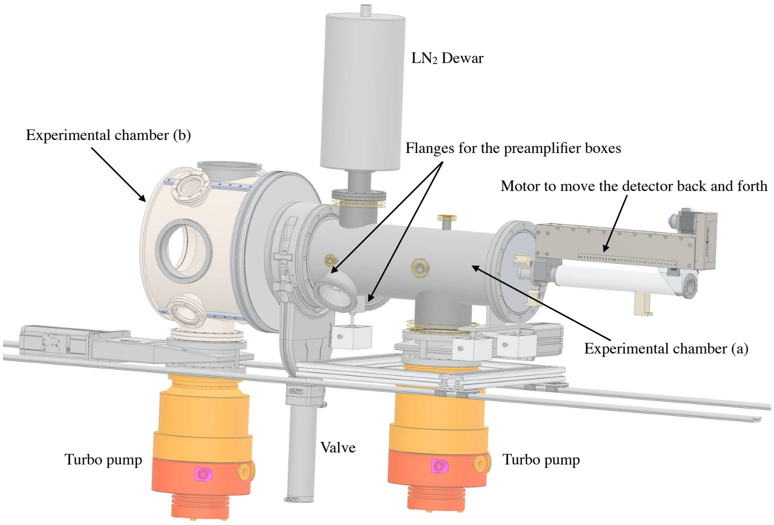

Figure 3.3: View of the two vacuum chambers designed to be installed at the SPES facility. Chamber (a) houses the detector and the cooling system, chamber (b) houses the tape, the magnetic transport system and a plastic scintillator.

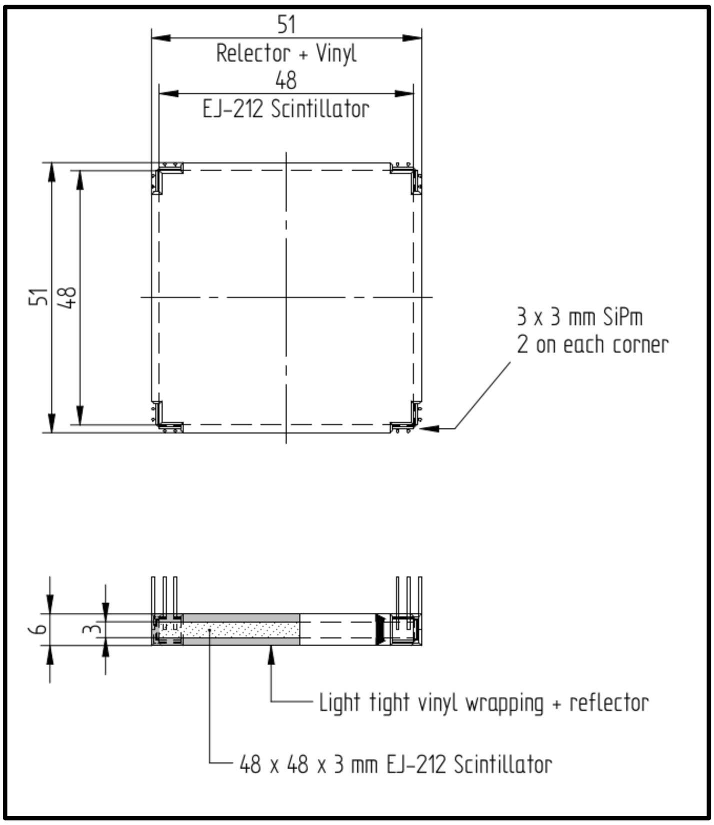

Figure 3.4: Mechanical drawing for the square prototype of the plastic detector.

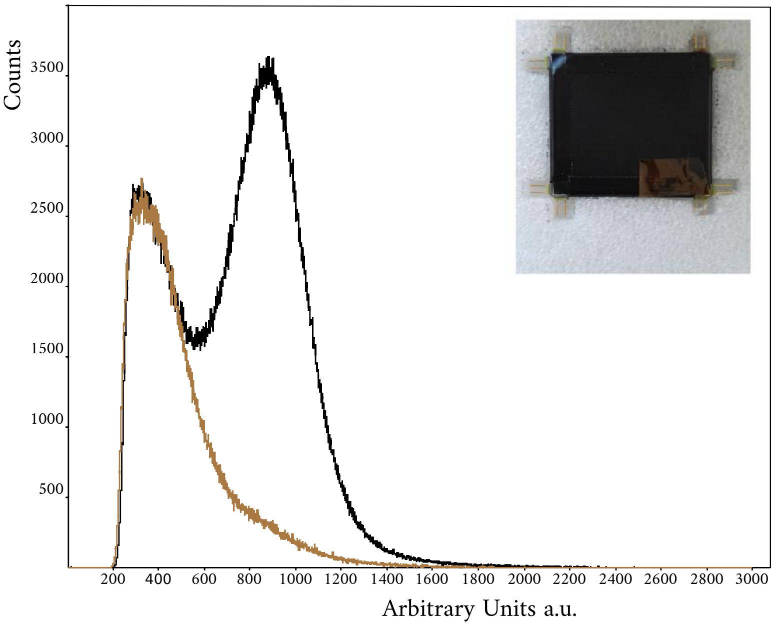

Figure 3.5: Plastic scintillator spectrum from measurements of ^{207}Bi radioactive source acquired with (brown line) and without (black line) an aluminum foil. The inset shows a photo of the plastic scintillator used for the measurement. See text for more details.

solution with a better light collection and, consequently, a higher detection efficiency than traditional PhotoMultiplier Tubes (PMTs).

In order to test the detector the radiations from a ^{207}Bi source (see Tab. 3.1) have been acquired. The resulting energy spectrum is reported in black in Fig. 3.5. Two bumps are clearly visible one at lower energies from the γ radiations and the second one corresponding to the internal electrons emitted by the source. To clearly identify the two contributions an aluminum foil, whose thickness (2 mm) was enough to stop electrons, was positioned in front of the source. The acquired spectrum is reported in brown in Fig. 3.5. Only the bump at lower energy is visible, thus confirming our hypothesis that it is due to γ radiation. This test proved the possibility to distinguish between the γ-ray and β-particle contributions, setting energy gates on the spectra acquired by the plastic scintillator. In this way, a correct tagging of β-decay of the parent nucleus will be granted.

Table 3.1: γ-ray energies, conversion electron energies and intensities of the ^{207}Bi source. The values are taken from [51].

E_γ[keV]	E_e	Shells	I_e[%]
569.7	481.7	K	1.537(22)
	553.8	L	0.442(6)
	565.8	M	0.111(5)
1063.7	975.7	K	7.08(17)
	1047.8	L	1.84(5)
	1059.8	M	0.44(3)
1770.2	1682.2	K	0.0238(12)
	1754.3	L	0.0034(5)

3.2 Handling and Cooling System

In order to have a good energy resolution, the Si(Li) detectors should be cooled with liquid-nitrogen to reduce the influence of thermal noise. For this reason, a dedicated cooling system has been implemented. The system, besides granting to reach the crystal temperature of about -150 °C, should allow moving the detector back and forth for a length of about 10 cm inside the vacuum chamber. Indeed, this possibility allows operating on the setup of the magnets and tape while keeping the detector cold; with the Si(Li) detector completely moved backward, the valve that separates the two chambers can be closed and the chamber housing the tape can be vented (see Fig. 3.3).

The detector holder is coupled to a linear translator, bellows sealed, driven by a stepper motor placed outside the vacuum chamber. The range of the detector-target distances varies from 105 to 170 mm. Accordingly to the solid angle covered by the detector ranges from 340 to 136 mrad. Both the movement of the translator and the valve opening/closing are remotely controlled. The motor for moving the detector can be seen on the right end of the chamber in Fig. 3.3.

In order to allow the movement of the detector while cold, the cooling system consists of a liquid nitrogen dewar and a copper braid. The dewar is mounted on top of the chamber housing the detector. A copper cold-finger dipped in the dewar is connected to the detector via a flexible and oxygen-free copper braid. This cooling system has been tested for a 300 mm length copper braid with a section of 90 mm^2 reaching -150° C in 9 h.

A Pt100 sensor is integrated into the front part of the detector holder to measure the temperature of the crystal. An additional Pt100 is integrated into the copper cold finger to monitor the difference in temperature between the cold finger and the detector holder.

3.3 SLICES description

SLICES combines the excellent energy and time resolution of the Si(Li) detector (described in section 3.3.1) with the selectivity and high efficiency of the magnetic lens (described in sections 3.3.2 et seq).

3.3.1 Si(Li) detector

The detectors to perform electron spectroscopy with a good energy resolution are the lithium-drift silicon Si(Li) ones, cooled to $\approx$-150° C. Unfortunately, these detectors have not seen in recent years the same technological progress as e.g. the HPGe ones. The commercial detectors have a maximum active area of 500 mm^2 and are not segmented. The only segmented, large area Si(Li) used for electron spectroscopy before this thesis, was the one installed in SPICE at TRIUMF. The SPICE detector has been developed at the Forschungszentrum GmbH in Juelich (Germany), therefore as a first step of this work, contacts were taken with this research center.

The SLICES detector has been developed in Juelich, from a Si-wafer of 3" in diameter and 6.5 mm thickness. This thickness is well suited to the measurement of electron energies up to 2 MeV since it exceeds the maximum distance of penetration of the electrons. One side of the crystal is a boron implanted contact and the other side is a $\sim$500 μm thick Li-diffused contact. Both contacts are covered with a $\sim$3000 $\mathring{A}$ thick

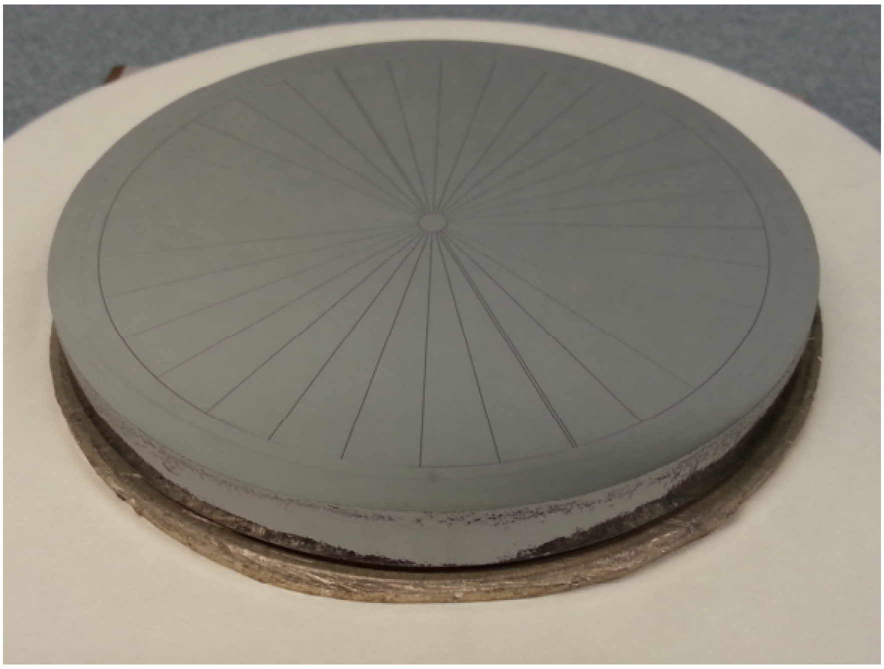

Figure 3.6: The segmented Si(Li) detector before mounting into the detector holder (view onto the boron-implanted contact). The 32 radial segments, the circular element at the center of the structure and the two wide tracks connecting the central element with the 4 mm wide guard-ring are visible.

Al-layer. The detector is fully depleted when biased at 800 V (depletion voltage is about 700 V).

The boron implanted contact has to be segmented into smaller elements to reduce the capacitance at Field Effect Transistor (FET) input of the preamplifier and, as a consequence, to improve the energy resolution. The preamplifiers are out of the vacuum installed in dedicated flanges. For the segmentation, a compromise between the number of elements and the required number of acquisition channels had to be chosen. In addition, the size of the elements should not be too small to keep the charge-sharing between neighbouring elements as low as possible. Eventually, a segmentation in 32 radial segments, each subtending a central angle of 11.25°, was chosen. The segments are surrounded by a 4 mm wide guard-ring. At the center, there is a circular element with a diameter of 3 mm which is connected to the guard-ring by two $\sim$300 μm wide tracks (see Fig. 3.6). The guard-ring and the circular element at the center will be grounded while the (not structured) Li-diffused back side contact will be connected to the detector bias. After the wire-bonding of the 32 segments to the printed circuit board (PCB) the front face of the detector has been covered with a thermal shield (17 μm thick aluminized Mylar-foil).

The first tests of the detector have been performed at the Juelich Research Center using a radioactive ^{207}Bi conversion electron source. Fig. 3.7 shows the decay of the ^{207}Bi source to excited states of ^{207}Pb via electron capture providing three strong transitions at 569.7 keV, 1063.7 keV and 1770.2 keV. The energy of the conversion electrons is given by the γ transition energy minus the binding energy of the K, L, and M electrons, which amounts to 88.0 keV, 15.3 keV and 3.9 keV, respectively. Tab. 3.1 shows a list of the energies and intensities of the internal conversion electrons.

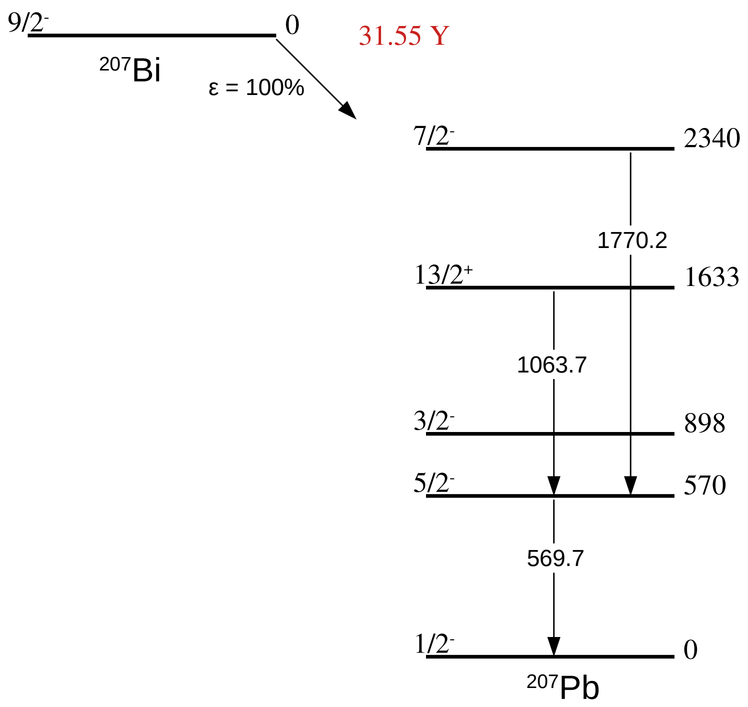

Figure 3.7: Level scheme of ^{207}Pb, populated by electron capture from ^{207}Bi.

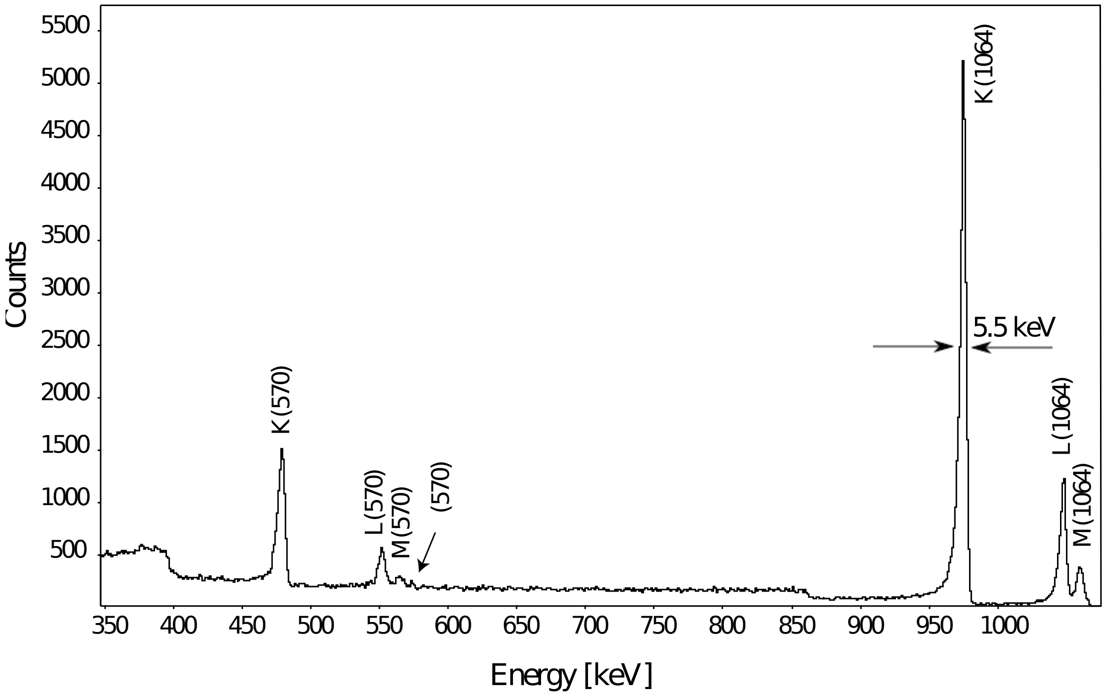

Figure 3.8: ^{207}Bi source spectrum obtained by adding the Si(Li) detector spectra from all the sectors. This spectrum has been acquired by an analog acquisition system with a shaping time of 6 μsec for the spectroscopy amplifier. No magnetic transport system was used.

The Si(Li) electron spectrum of this radioactive source is shown in Fig. 3.8. The spectrum has been obtained by adding the energy spectra from all sectors acquired with analog electronics. The shaping time for the spectroscopy amplifier was 6 μsec. The Si(Li) energy resolution is 5.5 keV at 975 keV enhanced with the respect to the test performed without segmentation for which the energy resolution was 8.7 keV at the same energy.

In Fig. 3.8 the Compton edges of the γ lines and a small peak corresponding to the 570 keV γ line are clearly visible. These background contributions to the electron spectrum will be reduced using the photon shield described in Sec. 3.3.3.

The electrons peaks in Fig. 3.8 have a tail towards the low energy side, due to incomplete energy deposition of electrons in the sensitive volume of the detector attributed to electron backscattering on the detector surface. In Ref. [42] the effects of backscattering on electron spectroscopy have been studied, finding a strong decrease of this contribution for the electrons hitting the detector at an angle close to the normal to its surface. The backscattering contribution to the background once fixed the distance source-detector, increases with the area of the Si(Li) detector and with the presence of the magnetic field, since the electron incident angle on the detector surface increases. For this reason, an appropriate choice of the shape of the magnets that produce the deflecting field is needed, as described in section 3.3.4, to reduce as much as possible the backscattering background.

3.3.2 Magnetic Transport system

The magnetic transport system is composed of a set of permanent NdFeB (N52) magnets and a central photon shield. It works similar to an optical lens: the electrons are focused onto the detector by the lenses as a function of the object distance g between the target and the center of the lenses (as following described) and the image distance b between the center of the lenses and the detector. For fixed electron energies the magnetic transport system works according to the well-known optical relation for the focal length f:

$$\frac{1}{f} = \frac{1}{g} + \frac{1}{b} \tag{3.1}$$

In this thesis, a detailed study of the design of the photon shield and the magnets has been performed, as following described.

3.3.3 Photon Shield

The γ-rays emitted from the nucleus under investigation can be a large source of background if not treated properly. In SLICES, and other electron spectrometers (see Ref. [49]), a photon shield is placed between the detector and target in order to absorb the γ-rays.

The linear attenuation coefficient is dependent on the energy of the γ-ray, therefore particular energy must be chosen to fix the design of the photon shield. In our case, the 511 keV is a good reference as it is the energy of the γ-rays produced during positron annihilation. Using the spectroscopic calculator of J. Kantele [45] it was calculated that to absorb/scatter 99.8 % of 511 keV γ-rays a Pb shield of 35 mm thick is needed. The γ-rays incident on the photon shield can ionise the Pb via the photoelectric effect or Compton scattering and subsequently, X rays would be emitted following atomic de-excitation. Thus, Cu layer of 3 mm was added to rear part of the shield, in front of

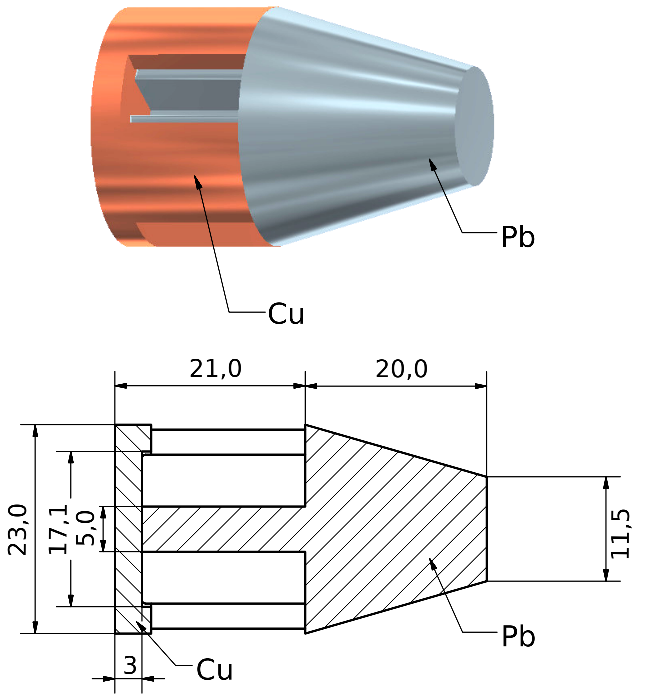

Figure 3.9: Upper panel: View of the photon shield composed by two different parts of Pb and Cu. See text for more details. Lower panel: Schematic view of the photon shield used for the commissioning. Dimensions are given in mm.

the Si(Li) detector. This thickness of the copper layer absorbs/scatters the 92% of the 75 keV X-rays produced in Pb.

The lead part of the photon shield has the shape of a truncated cone ending with a cylinder surrounded on the side of the detector by a copper layer as shown in the upper panel of Fig. 3.9.

The cylindrical part of the lead shield has four grooves to house the magnets, while the copper end cap has four tabs to keep them in the desired position. In this way the magnets are arranged symmetrically around the shield: the toroidal magnetic field focuses the electrons on the detector, while the γ-rays are blocked by the central absorber.

The truncated lead cone should completely cover the solid angle subtended by the detector. Its dimension depends not only on the source-detector distance but also on the source-shield distance, therefore the ideal situation is to have more absorbers for each combination of the chosen distances.

For the experiment performed in this thesis the minor radius and major radius of the truncated cone were 11.5 mm and 23 mm respectively, as shown in Figure 3.9 (for further details see Sec. 4).

3.3.4 SLICES efficiency: Tests and Simulations

Electron transmission has a primary role in the magnetic system design since it is the fundamental quantity that enters into the definition of the efficiency of the spectrometer. A compromise between the maximum (T) and the width (W) of the transmission curve needs to be found. When measuring monoenergetic electrons with energy E, the transmission T of an orange-type magnetic spectrometer is defined in Ref. [42] as:

$$T(E) = \frac{N(E)_{MS}}{N(E)_0} \tag{3.2}$$

where $N(E)_{MS}$ is the number of electrons with energy E and $N(E)_0$ is the number of electrons with the same energy detected without the magnetic transport system.

The transmission curve is related to another key feature: the detection efficiency. The absolute efficiency is usually defined as the ratio between the number of electrons detected in presence of the magnetic lens and the number of electrons emitted by the source. For an orange-type magnetic spectrometer [38], the absolute efficiency is defined starting from the transmission T(E) as:

$$\varepsilon(E) = T(E) \cdot \Omega \tag{3.3}$$

Where Ω is the solid angle subtended by the detector to the source in absence of the magnetic lens and photon shield. In this definition 100% of intrinsic efficiency for electron detection is assumed.

The efficiency curve is not only affected by the choice of the distances target-magnetic lens and magnetic lens-detector as reported in Eq. 3.1 but it is the result of an interplay of different factors, well illustrated in Ref. [39]. The most important ones are briefly summarized in the following paragraphs.

Shape of the magnets

Many different magnet shapes have been designed and implemented for electron spectrometers; the wedge shaped magnet is one of the most used in the case of mini-orange spectrometers (i.e. [39, 42]), while for a spectrometer involving large area detectors an irregular pentagonal shape has been adopted [36, 49].

In this thesis, the absolute efficiency of SLICES has been calculated for different magnet shapes in order to choose the best solution. Monte Carlo simulations using the GEANT4 code [27] have been performed (see Appendix B for more details). Both the geometry and the magnetic field data are imported from CST studio software [18]. This software is a powerful tool for the fast and accurate analysis of charged particle dynamics in 3D electromagnetic fields. Fig. 3.10 shows the simulated efficiency curves for two different magnetic lens configurations. The first is composed of four symmetric wedge shaped magnets (scaled compared to those described in Ref. [42]) and the other of four magnet clusters formed by a central pentagonal magnet between a pair of shorter rectangular magnets (similar to the ones described in Ref. [49].) A schematic view of the two types of magnets is reported in the left panel of Fig. 3.10). In the simulations the emission of 10^6 electrons for given energy from 200 to 2400 keV range in steps of 200 keV has been considered.

In order to validate the simulation, the efficiency curve for the configuration of four magnet clusters has been also measured using the internal conversion lines from the transitions from ^{207}Bi source (see Table 3.1). The K, L and M conversion electron lines for both the 569.7 keV, 1063.7 keV transitions are clearly identified in the electron spectrum measured using a Si(Li) detector with and without the magnetic transport system. For the 1770.2 keV transition, only the K conversion electron line is visible. The efficiency has been calculated as the ratio of counts in the Si(Li) spectrum with

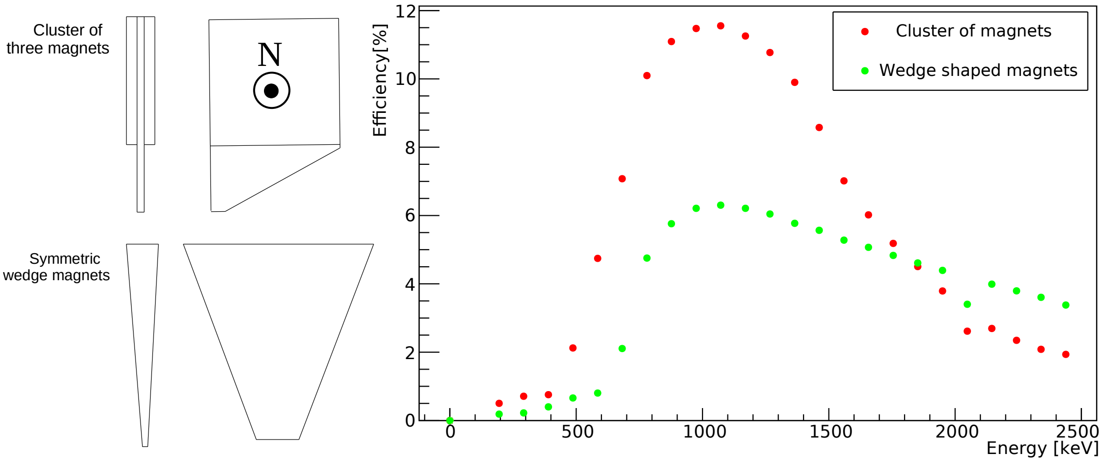

Figure 3.10: Right: simulated efficiency curves for two different magnetic lens shapes. Left: a schematic drawing of magnets used in the simulation, N is the direction of magnetisation. See text for more details.

and without the magnetic transport system, multiplied by the solid angle as reported in Eq. 3.3. The comparison between the experimental efficiency (red diamonds) and the simulated one (blue line) is shown in Fig. 3.11. The inset of this figure is a photo of the assembled magnetic transport system composed of four magnet clusters around a central absorber. The experimental data points nicely agree with the trend exhibited by the simulated curve. The drop of the efficiency for energies <800 keV is due to the size of the chosen magnetic lens: by changing the thickness of the magnetic clusters the efficiency maximum could be moved to lower (thinner magnets) or higher (thicker magnets) energies. An example of this effect is shown in Fig. 3.12, where the efficiency curves simulated for four clusters of three magnets of different thicknesses are reported. The green triangles refer to the efficiency in the case of four pentagonal magnets 3 mm thick, then the thickness has been modified adding two outer rectangular magnets each of 4 mm (red points) and 8 mm (blue diamonds) respectively. As shown in Fig. 3.12, both the maximum and the width of the efficiency curve change varying the thickness of the magnets, keeping fixed their shape and the detector-lens-source distances. The best configuration of magnets has to be chosen case by case as a function of the electron energies of interest.

Number of gaps

All the magnetic lens configurations implemented and tested during this thesis have equally spaced gaps. The maximum and the width of the efficiency curve could be modified by changing the number of gaps. As example in Fig. 3.13 is reported the simulated efficiency for a configuration of 3 (red points) and 4 (blue points) wedge shaped permanent magnets fixing both the distances detector-magnetic lens and magnetic lens-target.

For the configuration of four wedge shaped permanent magnets arranged symmetrically around a central photon shield the axial, radial and azimuthal B-field distribution has been measured using a Hall Probe. In Fig. 3.14 is reported a photo of the dedicated test station implemented during this thesis (left panel) and a schematic drawing of the magnetic transport system (right panel). The results are reported in Fig. 3.15: on the upper panel the magnetic field for the first gap as a function of the azimuthal angle

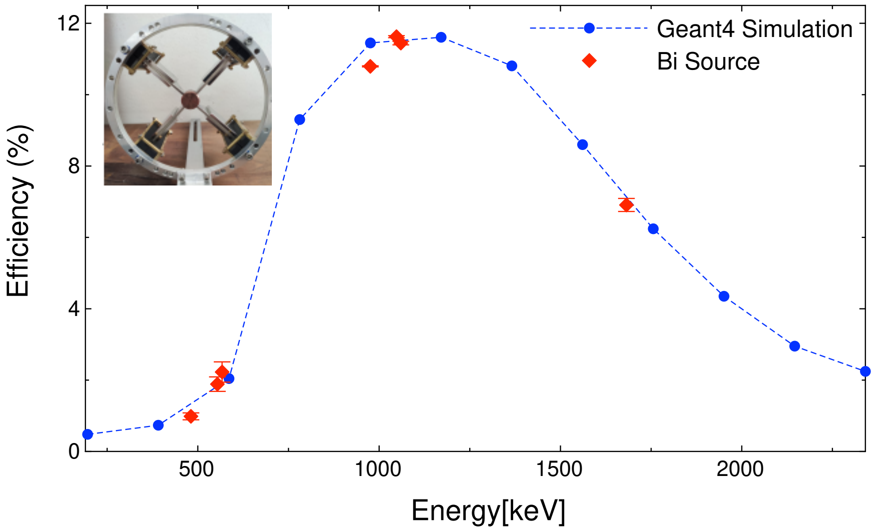

Figure 3.11: Absolute efficiency of SLICES for a source-detector distance of 117 mm using four magnet clusters. GEANT4 simulated efficiency curve is reported in blue dashed line while the experimental data points of transitions from a radioactive ^{207}Bi conversion electron source are reported in red. The inset shows a photo of the assembled magnetic transport system used for this measurement.

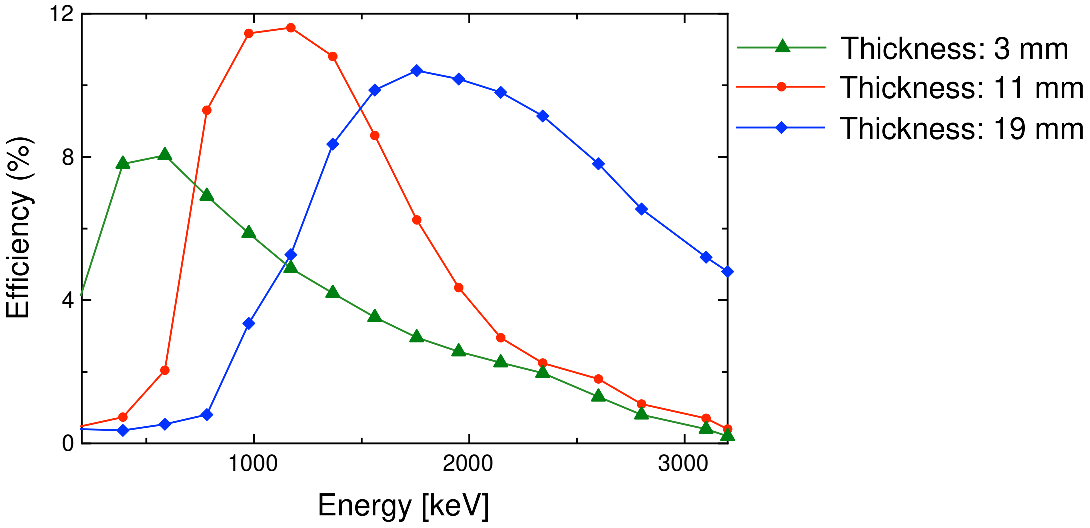

Figure 3.12: Absolute efficiency of SLICES for the detector–source distance of 117 mm and using four magnet clusters with three different thicknesses: 3 mm (green triangles), 11 mm (red points) and 19 mm (blue diamonds). The statistical errors are within the symbols.

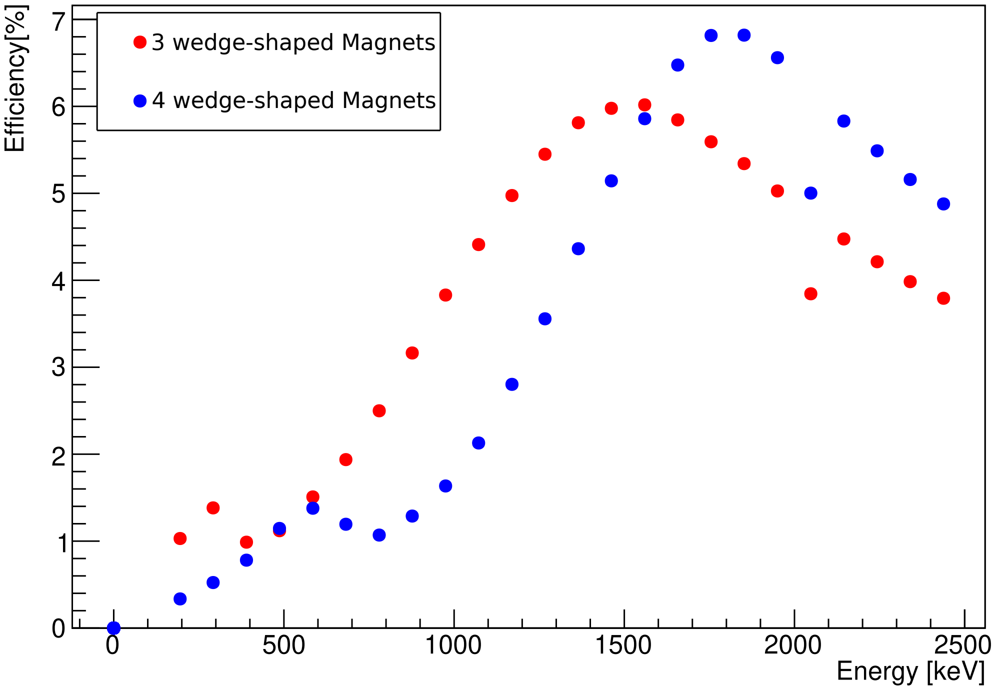

Figure 3.13: Absolute efficiency of SLICES for fixed distance detector-target and using three (red points) and four (blue points) wedge shaped magnets.

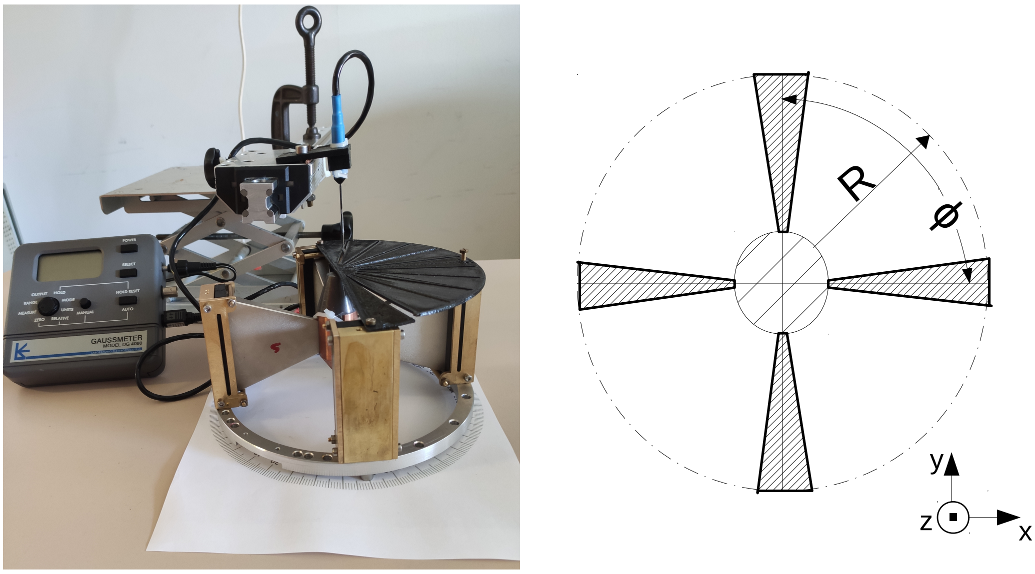

Figure 3.14: Setup to measure the magnetic field with a Hall probe. It enables to measure the magnetic field strength in radial, azimuthal and axial direction. Left: picture of the dedicated test station. Right: Drawing of the magnetic transport system.

for different radial distances R; on the lower panel the magnetic field strength in the middle plane of each gap as a function of the radial distance from the magnetic transport system center. The azimuthal angle ϕ equal to 45° and z (which corresponds to the distance between halfway entrance and exit surface of the magnets) equal to 0 have been fixed. Increasing the radial distance the magnetic field decreases, in particular for R $\leq$ 30 mm the magnetic field has an average value of B $\sim$ 250 mT. In the middle plane between two lenses, the magnetic field falls off for radii larger than R$\sim$ 30 mm for all the gaps.

For this studied configuration the magnetic field strength has been also mapped using the CST Studio software [18]. In order to map the magnetic field a dedicated CAD design of the apparatus has been done. The residual magnetic induction value used for the simulations is 1.25 T, which corresponds to the value given by the manufacturer for the N52 material. In Fig. 3.16 a comparison between simulated (blue points) and measured (red diamonds) magnetic field strength is reported as a function of radial distance R (fixing ϕ=45° and z=0). No experimental data is available at lower radius due to the radial dimension of the photon shield, which makes this region inaccessible for the probe. The agreement between the simulation and the measured data is excellent.

Electron Backscattering

As described in Sec. 3.3.1 both the large size of SLICES detector and the presence of the magnetic field increase the electron incident angle thereby the amount of backscattering background in our spectra. For this reason, in the design of the shape of the magnetic lens, it is also important to ensure an incident angle of the electrons on the detector as small as possible to reduce the electron backscattering contribution to the background.

In order to evaluate the distribution of the angles of incidence on the detector surface, the electron trajectories in the magnetic fields have been simulated using CST studio software for the two types of magnetic lens reported in Fig. 3.10. The detector-source distance is the same in both cases. The distribution of the electron incident angle on the detector plane as a function of energy is reported in Fig. 3.17. It can be seen how, for given electron energy the incidence angle is closer to 0° when the magnet clusters are used. This configuration, which decreases the backscattering contribution to the background, has been accordingly adopted.

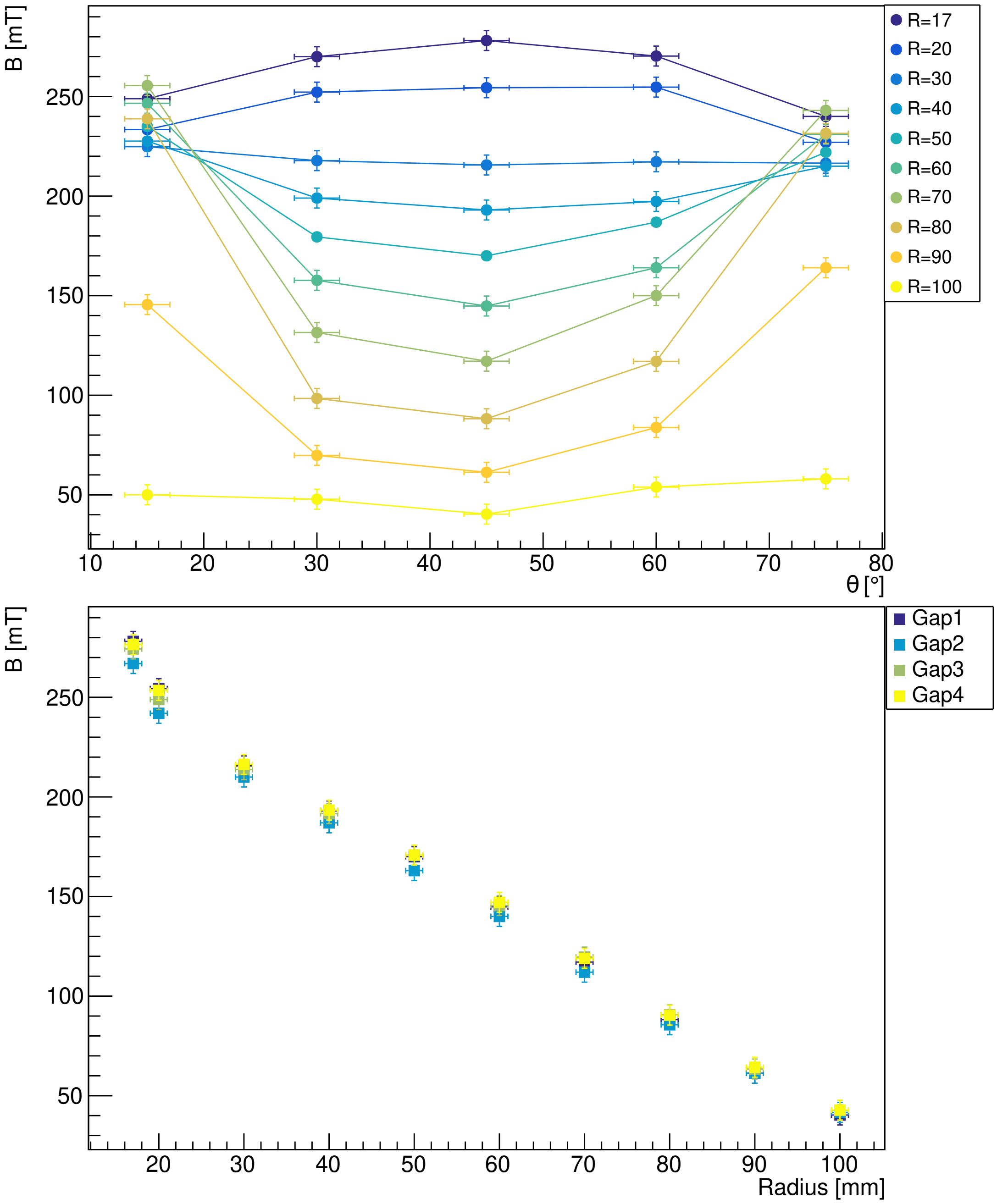

Figure 3.15: Upper: the magnetic field in the first gap as a function of the azimuthal angle ϕ and for different values of radial distances R from the magnetic transport system center. Lower: the magnetic field strength in the middle plane (see text for more details) in each of the 4 gaps as a function of the radial distance from the magnetic transport system center.

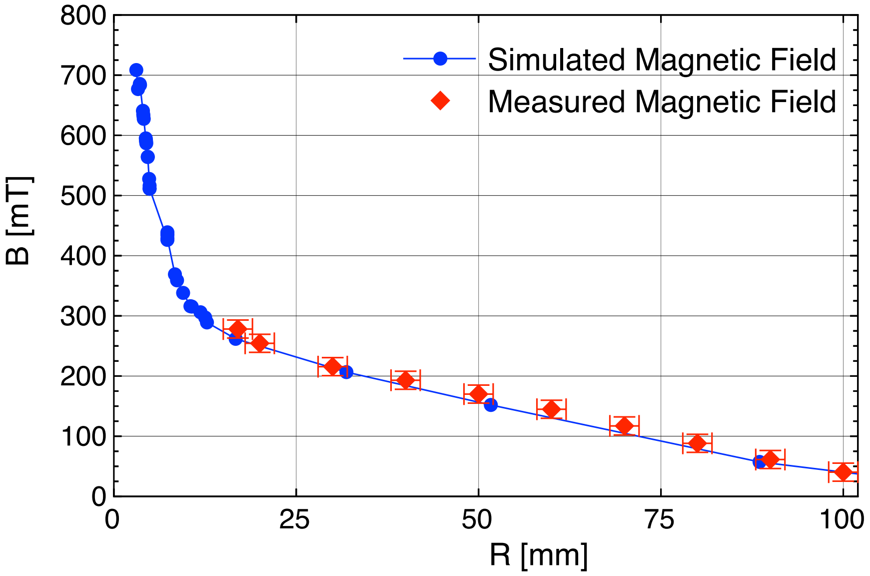

Figure 3.16: Comparison between simulated (blue line) and measured (red points) magnetic field as a function of radial distance from the photon shield fixing the azimuthal angle $\phi \sim 45°$ and $z \sim 0$. See text for details.

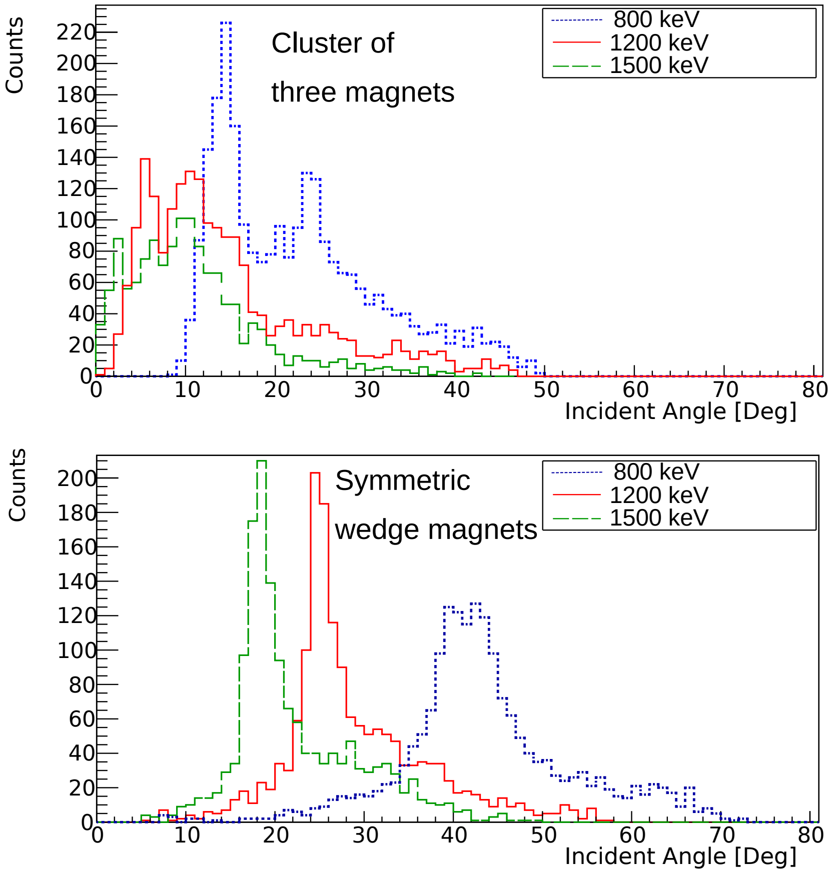

Figure 3.17: The electron incident angle on the detector plane, as a function of energy for four clusters of three magnets (upper panel) and for four symmetric wedge shaped magnets (lower panel).

4. Commissioning Experiment

In this chapter, the commissioning of SLICES, with an experiment aimed at studying the properties of the low-lying levels of the nucleus ^{106}Pd, will be described. The levels of interest have been populated via the EC/β^+ decay of ^{106g}Ag ($T_{1/2}$=24 min). The ^{106}Ag nucleus has been produced in the ^{106}Pd(p,n)^{106}Ag reaction, using a 5.5 MeV proton beam delivered by the Van de Graaff CN accelerator at LNL with an average intensity of 200 nA, impinging on a self-supporting ^{106}Pd target 3 mg/cm^2 thick (96% enriched).

4.1 SLICES at the CN accelerator

Since the ^{106}Ag parent nucleus has a long lifetime, a new setup for SLICES has been implemented for this experiment. This uses a movable target instead of the tape system.

A schematic view of the new setup is shown in Fig. 4.1. It consists of: a coaxial large-volume HPGe crystal to detect the γ-rays, SLICES to detect conversion electrons and a step motor to move periodically the target from the irradiation point to the counting point and back. In Fig. 4.1 the experimental chamber (a) is the vacuum chamber designed to house the Si(Li) at the SPES facility, but used in this commissioning for both the detector and the magnetic lens, while the experimental chamber (c) is a new dedicated vacuum chamber used for the moving target. The target has been moved in vacuum by the same stepper motor that will be used at SPES to move the detector. The two chambers have been separated by a valve to allow changes in the target chamber while keeping the detector cooled at working temperature. The opening and closing of the valve are remotely controlled.

The measurements were performed cyclically alternating irradiation periods with measuring periods. To achieve this functionality in an automatized way, a dedicated control program has been implemented. It is able to handle both the stopping of the beam, the movement of the target and the start of the acquisition system. Activation and measurement times are optimized on the basis of the lifetime of the parent nucleus. If needed, it is possible to interpose a waiting time between activation and measurement periods to allow for the decay of, potentially disturbing, short-living species.

The new setup allowed the use of a quartz in place of the target during the beam alignment phase. The positioning of the quartz did not require the break of the vacuum in the chamber. The same computer code, that controls the target movement, can activate the insertion or removal of the quartz, via a pneumatically-operated holder.

The lower panel of Fig. 4.1 shows a view of the configuration adopted in the commissioning. In this setup, the detector-target distance is fixed to 117 mm while the configuration of the magnetic lens could be chosen to maximize the detection efficiency in the ICE energy range of interest. In order to reduce the backscattering contribution,

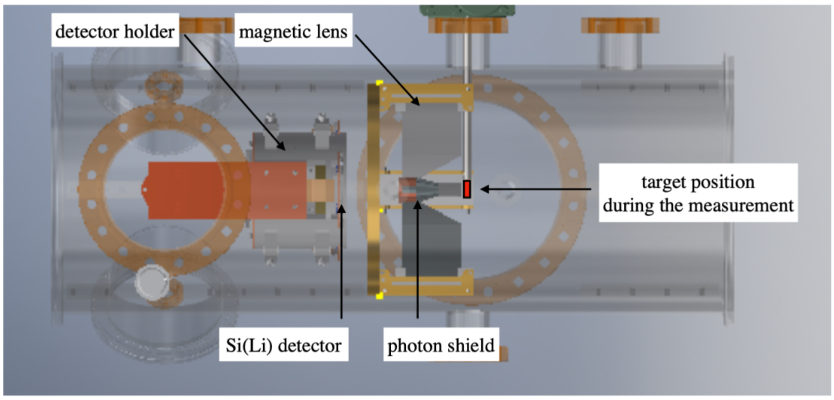

Figure 4.1: Upper part: Design of the experimental setup for internal conversion electron measurements planned for the SLICES commissioning. The dimensions are given in mm. In this configuration the detector-target distance is equal and fixed to 117 mm. Lower part: view of the main SLICES components inside the experimental chamber (a)

$J_i^+ \rightarrow J_f^+$	E_e [keV]
$0_2^+ \rightarrow 0_1^+$	1109
$0_3^+ \rightarrow 0_1^+$	1682
$0_4^+ \rightarrow 0_1^+$	1977
$2_2^+ \rightarrow 2_1^+$	592
$2_3^+ \rightarrow 2_1^+$	1026

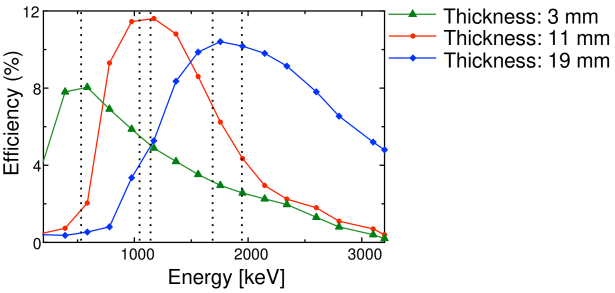

Figure 4.2: Left: table with ICE energies of the transitions of interest for this thesis. Right: simulated SLICES efficiencies for a 117 mm detector-target distance and four gaps configuration with different thickness of clusters. The vertical dotted lines correspond to the ICE energies of interest.

the cluster of magnets configuration has been adopted (see Section 3.3.4).

The transitions and the electron energies of interest in this experiment are reported in the left part of Fig. 4.2, while the right part of the figure shows the simulated SLICES efficiency obtained considering four clusters of magnets. Different colors correspond to different magnet thicknesses, as indicated in the Figure. The vertical lines mark the energies of interest. It could be noticed that the best magnetic lens configuration for the present commissioning is the one composed of four magnetic clusters each with a maximum thickness of 11 mm. The four magnetic clusters have been arranged around the photon shield shown in Fig. 3.9. The efficiency measured in this configuration of SLICES with a radioactive ^{207}Bi source is reported in Fig. 3.11.

4.2 ICE measurements in ^{106}Pd

The ^{106}Ag isotope has two EC/β-decaying states, the 1^+ ground state ($T_{1/2}$=24 min) and the 6^+ isomeric state ^{106m}Ag ($T_{1/2}$=8 d). With the aim to favor the fast decay activity of ^{106}Ag, which populate the 0^+ levels in ^{106}Pd, measurements have been performed by alternating bombarding and measuring period of 35 min.

At the beginning of the experiment, we noticed that an unexpected continuum background was visible in the electron spectra in the energy range from 500 to 1600 keV. Due to its shape, the background was attributed to β^- particles from the target, focused on the detector by the magnetic lens. The continuum β^- background is evident up to ~1650 keV. This energy corresponds to the Q value of the β^- decay of ^{108}Ag ($T_{1/2}$=3.4 d). The ^{108}Ag isotope was produced in the (p, n) reaction on the 1% ^{108}Pd isotope present in the target material. The ^{108}Ag ground state decays 97% β^- to ^{108}Cd (95% to the ground state), producing the background in the electron spectra. The only other contaminant present in the target that can significantly contribute to the background is the ^{105}Pd isotope (2%). However, no transitions related to the ^{105g}Ag EC decay are visible in the spectrum.

A 5 min waiting time was then inserted after the activation, to allow the decay of the short lived ^{108}Ag before starting the counting period. Fig. 4.3 shows a comparison of the spectra acquired with and without the waiting time in brown and black, respectively. The spectra were normalized to the intensity of the 616 keV γ-ray transition in ^{106}Pd, to take into account possible fluctuations in the beam current. Thanks to the waiting

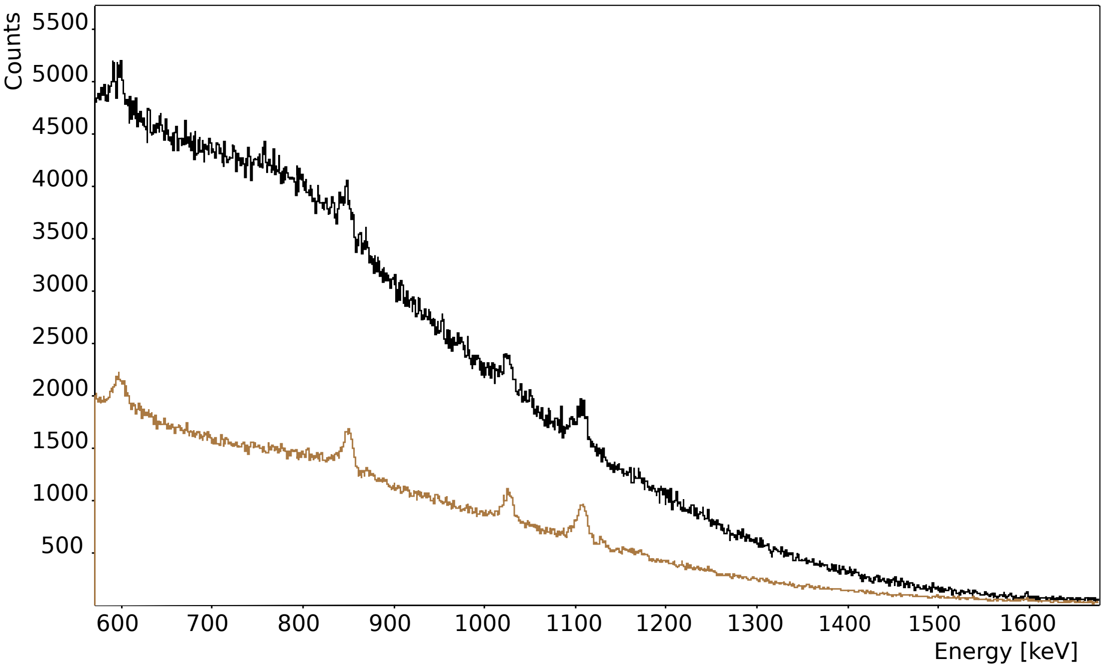

Figure 4.3: SLICES spectra from the EC/β^+ decays of ^{106}Ag acquired with (brown line) and without (black line) the waiting time. The spectra are normalized to the intensity of the 616 keV γ-ray transition in ^{106}Pd.

time, the β^- background is strongly reduced gaining a factor ≈2 in the peak to total ratio.

The residual background in the brown spectrum of Fig. 4.3 is also due to γ-rays reaching the Si(Li) detector, despite the presence of the photon shield. The reason is that the thickness of the photon shield has been calculated taking as a reference a γ-ray of 511 keV (see Section 3.3.3). As the energy of the γ-ray increases the shield is less effective and the number of the γ-rays that cross the shield increases. At an energy of 1 MeV, only 94% of the γ-rays are stopped, while at 2 MeV the percentage drops to 84%.

As a first step, the photon shield has been tested with a ^{207}Bi source placed at the target position. The spectra acquired with (upper panel) and without (lower panel) the magnetic transport system are reported in Fig. 4.4 (discussed in detail in Section 4.4). The reduction of the γ-ray background is evident; indeed the Compton edge for the γ-ray transition at 1063 keV is no longer visible.

As a second step, a ^{152}Eu source was placed at the target position, the obtained spectrum shows a continuum background (the Compton plateau) ending with the Compton Edge of the 1408 keV transition. No full energy peaks are visible in the energy region where the strong line at 344 keV is expected (see Table 4.1), thus confirming the well-chosen photon shield thickness.

With no clear γ-rays from the target, the only radiations that can contribute to the background are those that are scattered off the various components within the chamber and the chamber itself. Our conclusion is that the residual background is partly due to the β^- radiation from the not yet decayed ^{108}Ag nuclei and partly due to the scattered radiation onto the detector. Dedicated GEANT4 simulations are ongoing to confirm this hypothesis.

4.3 Acquisition System

The data acquisition system is fully digital and similar to the one implemented for the SPES β-decay station: the signals from the preamplifiers are sent to a digital readout made of commercial 14-bit V1725 digitizers from CAEN, running at 250 Msps. A master clock signal is propagated to the individual modules to achieve the synchronization of all digitizers clock.

The data are acquired in “cycles” in which an off-line counting period follows an activation period. The timing of the cycles is controlled by a dedicated control program previously described, which generates a number of logic signals: one to enable the beam for a predetermined time and to veto the digitizer trigger, one to stop the beam, and to enable the measurement for a predetermined time. In order to avoid collecting data during the target (or the tape for SPES) motion, the veto signal lasts for a preset time after the beam interruption. This waiting time, if needed, can be lengthened to allow short-lived activation to decay.

In the commissioning experiment, data are online monitored and acquired using the CAEN Multi-PArameter Spectroscopy Software (CoMPASS) [17]. For the future experiment at the SPES facility, the acquisition will be based on the XDAQ distributed acquisition framework for which dedicated modules have been developed. The architecture will be similar to the one developed for the GALILEO HpGe array at LNL [31]. Each module will be in charge of a dedicated task: readout of the electronic modules, data formatting, event building. All modules offer the possibility to write the data directly on disk or send them to TCP receivers for data online monitoring. The γ-ray energy spectrum from the HPGe detector is also acquired in the CoMPASS framework.

4.4 Energy Calibrations

4.4.1 Si(Li) detector

The sectors composing SLICES have been individually energy calibrated using a ^{207}Bi source. The energy calibration was performed before the experiment and at the end of the experiment, to check the stability of the calibration over time. All sectors are summed off-line performing rebinning of the spectra: a procedure has been implemented to automatically align and calibrate all sectors using the ^{207}Bi source peaks, before adding up all spectra sectors.

As a first step the electron energy spectrum of a ^{207}Bi source, placed at the target position, has been acquired without the magnetic transport system. In this way, the resolution of the Si(Li) detector can be evaluated. In the spectrum the K and L conversion lines of all the three transitions at 569.7 keV, 1063.7 keV, and 1770.2 keV can be seen, while the M-conversion electron peak can only be observed for the 569.7 keV and 1063.7 keV transitions. The section of the spectrum ranging from 400 to 1100 keV is shown in the lower panel of Fig. 4.4. It is seen that the K-L-M lines of the most intense transition from the ^{207} Bi can be resolved. The FWHM is about 8 keV at 975 keV.

To have a direct comparison with the resolution obtained in Juelich during preliminary tests of the detector (see Section 3.3.1) the electron energy spectrum of one sector has been acquired also with analog electronics and a multichannel analyzer at the CN accelerator, before the experiment. In the traditional analog chain, the Shaping Ampli-

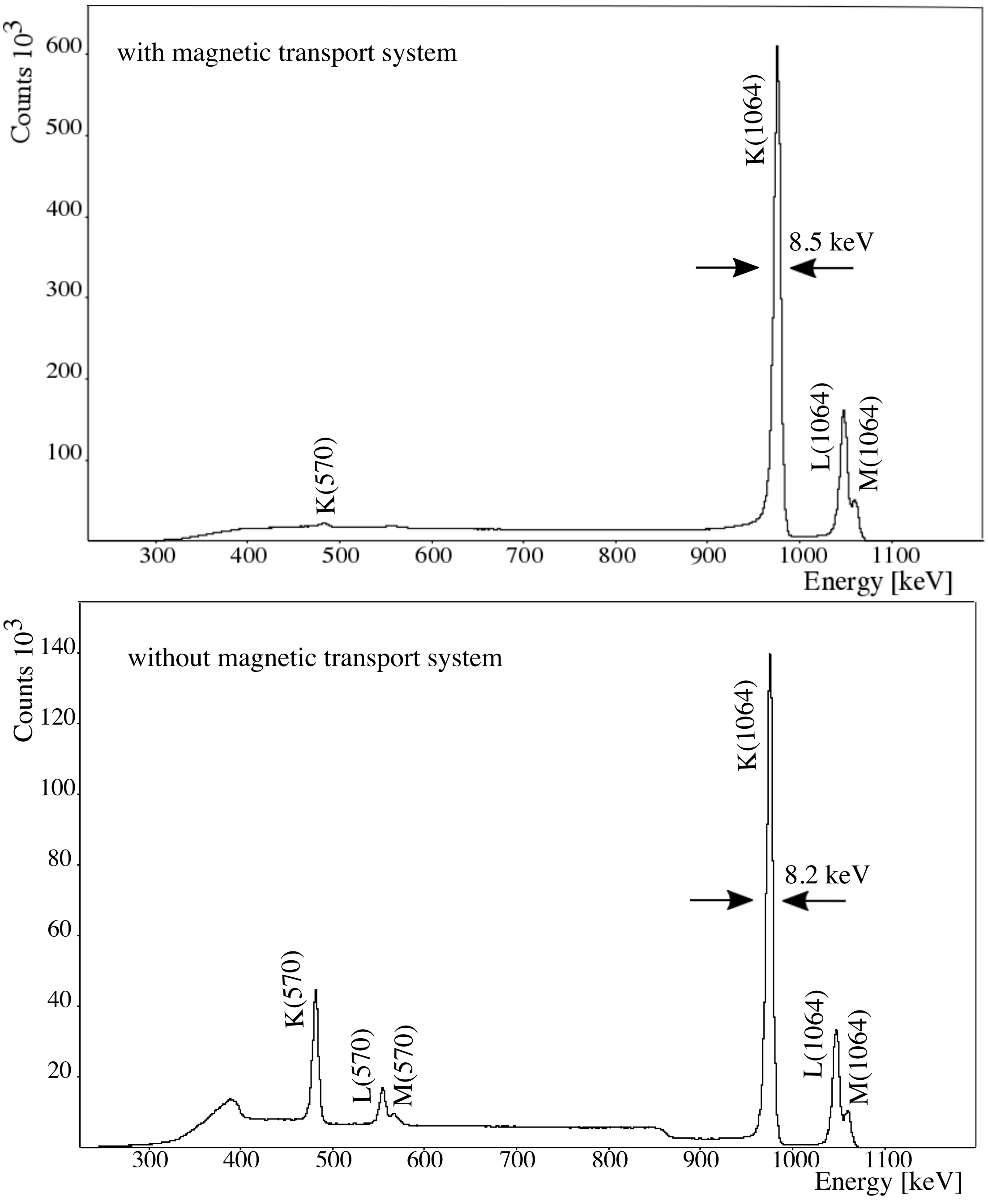

Figure 4.4: Normalized SLICES spectra from measurements of ^{207}Bi radioactive source acquired with (upper panel) and without (lower panel) the magnetic transport system. The FWHM of the main peak is reported in both panels. These spectra have been acquired by the digital acquisition system. The reduction of the radiation background using the magnetic transport system is clearly visible. The cut off around ≈350 keV is due to the acquisition threshold.

fier is able to convert the exponential shape from the Charge Sensitive Preamplifier into a Gaussian shape, whose height is proportional to the energy released in the detector. In the same way, the trapezoidal filter in the Compass acquisition system is able to transform it into a trapezoidal signal whose amplitude is proportional to the input pulse height (energy). In this analogy, the Trapezoid Rise Time corresponds to the Shaping Time times a factor of 2/2.5 (see Ref. [17]). Therefore electron energy spectra have been acquired setting the trapezoid rise time at 14 μsec (the maximum allowed value for our digitizers), corresponding to an analog shaping time of $\approx$6 μsec. The shaping time of the spectroscopy amplifier was set to 6 μsec, the same value adopted for the test. Using these parameters the obtained FWHM is $\approx$7 keV at 975 keV (it slightly depends on the sector being used) for both analog and digital acquisition systems. The increase in the FWHM with respect to the tests could be due to the noise present in the experimental hall. To reach the FWHM of $\approx$5 keV at 975 keV the shaping time has to be set to 10 μsec, which would imply a too large value for our digitizers.

For the future measurements at the SPES facility, where a β-tagging from a plastic scintillator (described in Chapter 3) will be used, it will be necessary to work with a shorter trapezoid rise time, around 8 μsec, to have a good time resolution.

As a second step, the magnetic transport system composed of four magnets clusters has been mounted inside the detector chamber as shown in the lower part of Fig. 4.1. The electron spectrum of the ^{207}Bi source acquired in this configuration is reported in the upper panel of Fig. 4.4. As expected on the basis of the simulated efficiency curve (red points in Fig. 4.2), the magnetic field produced by the chosen magnetic lens configuration enhances the intensity of K-L-M-conversion electrons around 1 MeV while the peaks around 500 keV are reduced. The energy resolution obtained with the magnetic transport system is 8.5 keV at 975 keV.

As already remarked in section 3.3.1, the electron peaks have a tail towards the low energy side. The tail is even more pronounced when the magnetic field is present, as shown in Fig. 4.4. This is due to the fact that the average electrons incident angle on the detector increases because of the bending of the trajectories. Indeed in the absence of the magnetic field, the maximum incident angle for a detector set at 117 mm from a point source is around 16°, while with the magnetic field this angle may reach the value of 30° for $\sim$ 1.2 MeV electrons (see Fig. 3.17).

Due to the asymmetric shape of the peaks in the electron energy spectra, for a precise evaluation of the peak areas, the lines have been fitted by a function resulting from the convolution of a Gaussian curve with a delta function plus an exponential “tail” on the low-energy side.

HPGe detector

The γ-ray energy spectrum has been calibrated using a 396 kBq ^{152}Eu source mounted at the target position. The energies and relative intensities of the transitions are shown in the first and second columns of Table 4.1.

The same ^{152}Eu source was used to measure the absolute photopeak efficiency ϵ_γ of the HPGe detector. Only the γ-ray lines whose relative intensities are known with high precision were considered. ϵ_γ is defined as the ratio of the numbers of γ-rays detected in the full energy peak to the number of those emitted from the source. These are obtained considering the source activity at the moment of the measurement, the duration of the measurement, and the relative intensities of each γ-ray transition. The absolute efficiency values obtained for the ^{152}Eu γ-ray energies are listed in the last

Table 4.1: Energy of the γ-ray transitions from the ^{152}Eu source, used for the efficiency calibration of the HPGe detector. Their relative intensities are reported in the second column, while the corresponding absolute photopeak efficiencies are listed in the last column.

E_γ[keV]	Intensity[%]	ϵ_{abs}[%]
121.8	28.37	0.218(8)
244.7	7.53	0.194(6)
344.3	26.57	0.159(5)
411	2.24	0.138(4)
444	3.13	0.129(4)
779	12.97	0.088(2)
867	4.21	0.082(3)
964	14.63	0.076(2)
1085	10.13	0.071(2)
1089	1.73	0.077(2)
1112	13.54	0.070(2)
1212	1.41	0.066(2)
1299	1.63	0.063(2)
1408	20.85	0.060(2)

column of Table 4.1.

The data have been fitted with the commercial software ProFit, using the custom defined function:

$$\epsilon(E_\gamma) = \frac{A}{x} + \frac{B}{x^2} + \frac{C}{x^3} + D \tag{4.1}$$

where A-D are the fitted parameters and x is the γ-ray energies. The result of the fit is shown in Fig. 4.5 together with the data points.

4.5 Experimental Results

4.5.1 E0 Transitions

Conversion electron measurements have been performed to determine K internal conversion coefficients and to evaluate the monopole strength of E0 transitions between states having the same spin and parity.

The electron energy spectrum of ^{106}Pd acquired with SLICES is shown in Fig. 4.6. The observed $2^+_2 \longrightarrow 2^+_1$, $0^+_2 \longrightarrow 2^+_1$, $0^+_4 \longrightarrow 0^+_2$, $0^+_4 \longrightarrow 2^+_2$, $2^+_3 \longrightarrow 2^+_1$, $2^+_2 \longrightarrow 0^+_1$, $0^+_2 \longrightarrow 0^+_1$, $0^+_3 \longrightarrow 0^+_1$ and $0^+_4 \longrightarrow 0^+_1$ transitions are labelled. Due to the smaller intensities of the $0^+_3 \longrightarrow 0^+_1$ and $0^+_4 \longrightarrow 0^+_1$ transitions, the vertical scale of the histogram in Fig. 4.6 has been scaled.

The internal conversion coefficients α_K, obtained from Eq. 2.18, are reported in Table 4.2. In the calculation of the experimental values of the α_K, the values obtained by the simulation for the SLICES efficiencies have been used, due to the good agreement between the simulated efficiency curve and experimental data from the ^{207}Bi source, shown in Fig. 3.11. In the same table, the theoretical values for E2 and M1 multipolarities calculated with the BrIcc online calculator [37] are shown.

The agreement between the experimental and the theoretical values for pure E2 transitions represents a stringent test of the reliability of SLICES apparatus in performing

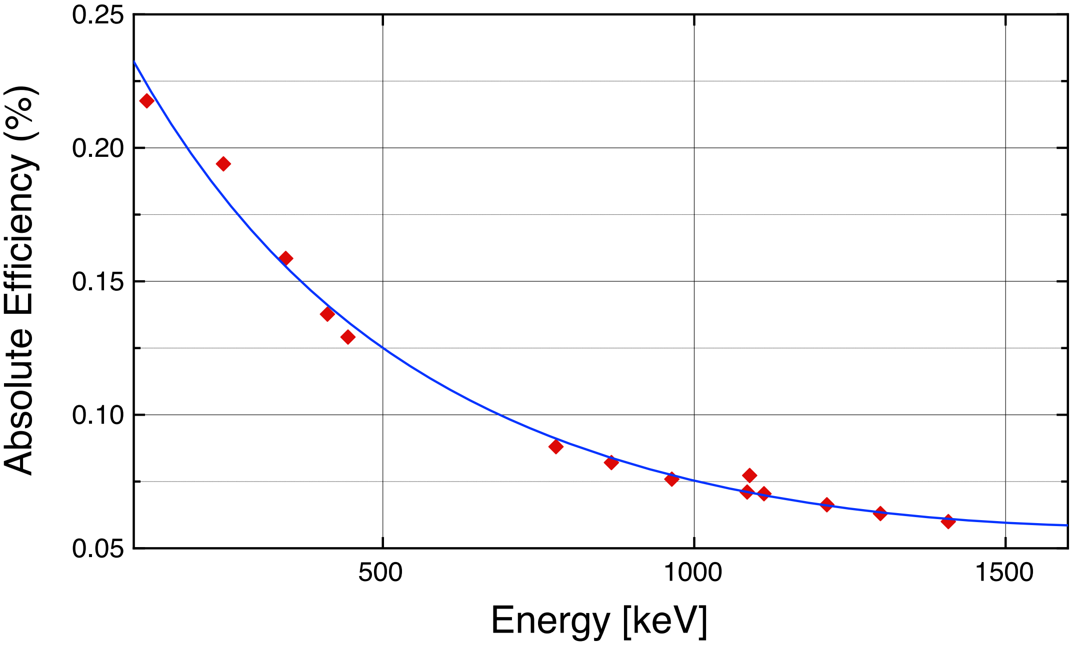

Figure 4.5: Absolute photopeak efficiency of the HPGe detector as a function of the γ-ray energies. The measured efficiencies are reported in red, while the fitted function is shown in blue.

internal conversion electron measurements.

It is noteworthy that two different α_K values for the $2_3^+ \longrightarrow 2_1^+$ transition are reported in the literature: $\alpha_K(2_3^+ \longrightarrow 2_1^+)$=1.12(15) in Ref.[16], and $\alpha_K(2_3^+ \longrightarrow 2_1^+)$=1.56(24) in Ref.[23]. The value obtained in the present thesis is compatible with the one determined in Ref. [16], thus solving the discrepancy. The experimental $\alpha_K(2_3^+ \longrightarrow 2_1^+)$ value, large with respect to the calculated alpha$_K$ for an M1/E2 transition,, suggests the presence of a significant E0 component.

Measurements of internal conversion electrons allows to determine the q^2(E0/E2) ratio, defined in Eq. 2.16, which is related to the the monopole transition strength ρ^2 via Eq. 2.20.

The value of q^2(E0/E2), can be obtained directly from the ratio of the peak areas corresponding to the E0 and E2 transitions of interest in the electron spectrum of Fig. 4.6.

In Table 4.3 the q^2(E0/E2) and ρ^2 values extracted in this thesis are summarized. The data about the level lifetimes, mixing ratios and branching ratios needed to calculate the ρ^2 values from the Eq. 2.20, are taken from [56].

The q^2(E0/E2) values for transitions from the fourth 0^+ state in ^{106}Pd are extracted for the first time in this thesis. Unfortunately, only a lower limit for the lifetime of this level is reported in the literature, therefore only an upper limit for the corresponding ρ^2 values was obtained.

Also, the E0 contribution to the K conversion $2_2^+ \longrightarrow 2_1^+$ transition was determined for the first time in this thesis. However, the obtained q^2($2_2^+ \longrightarrow 2_1^+$) value has a large uncertainty, since the analysis of the $2_2^+ \longrightarrow 2_1^+$ K electron line was made difficult by the presence of the predominant 616 keV peak corresponding to the K-conversion electrons of the $0_2^+ \longrightarrow 2_1^+$ transition.

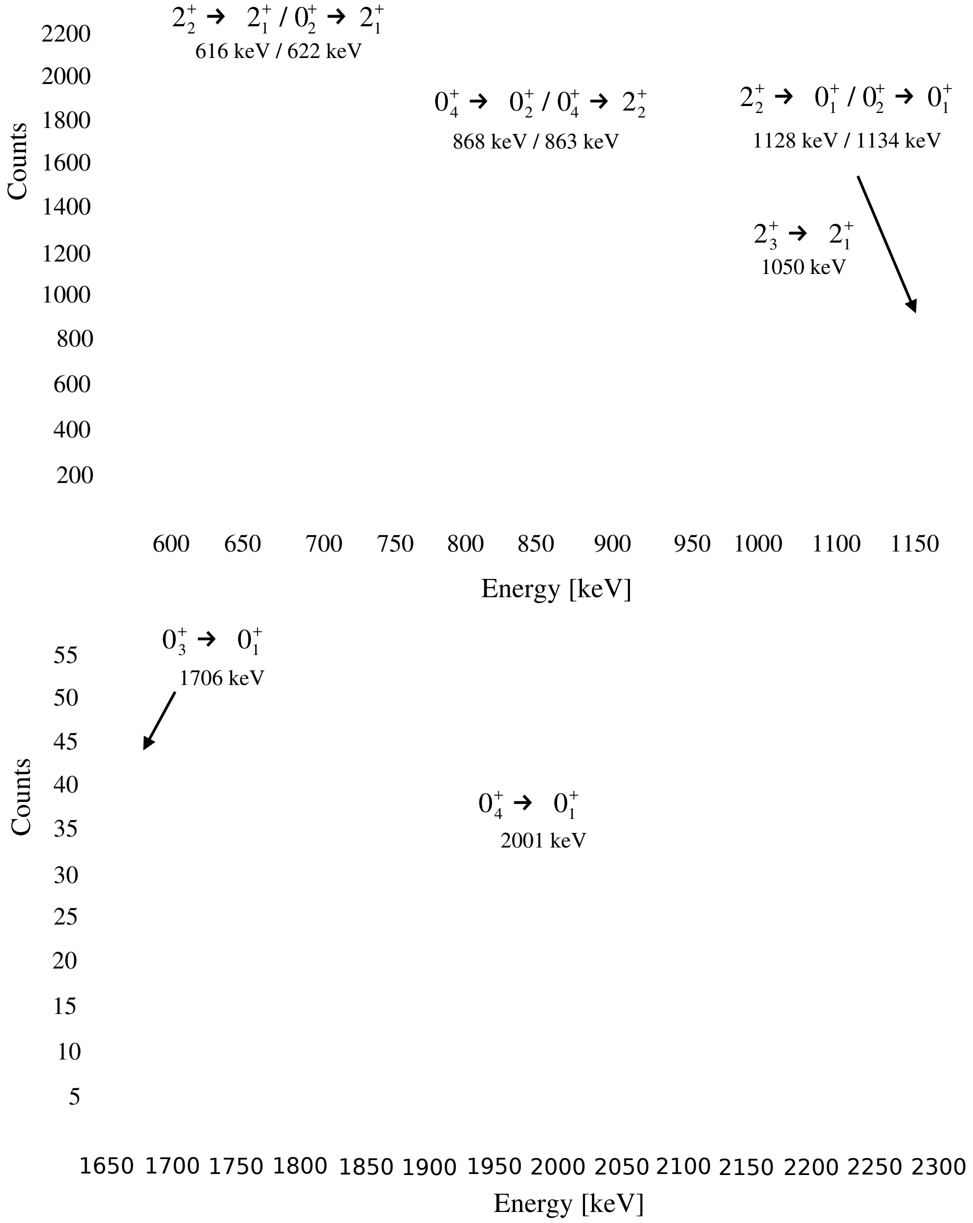

Figure 4.6: Electron energy spectrum acquired by SLICES. The peaks corresponding to the observed transitions are indicated. Since the smaller intensities of the $0_3^+ \longrightarrow 0_1^+$ and $0_4^+ \longrightarrow 0_1^+$ transitions the scale of the vertical axis has been expanded. In the rest of the spectrum no transition of interest is present.

Table 4.2: The internal conversion coefficients obtained in the present work. The transitions reported in the first column are compared with the theoretical values for E2 and M1 multipolarities reported in fourth and fifth columns. The theoretical values are calculated with the BrIcc online calculator [37].

$J_i^\pi \longrightarrow J_f^\pi$	E_γ [keV]	$\alpha_{Exp.} \cdot 10^3$	$\alpha_K(E2) \cdot 10^3$	$\alpha_K(M1) \cdot 10^3$
$2_2^+ \longrightarrow 2_1^+$	616	2.97(11)	2.89	2.97
$2_2^+ \longrightarrow 0_1^+$	1128	0.64(9)	0.68	
$2_3^+ \longrightarrow 2_1^+$	1050	1.06(7)	0.79	0.89
$0_2^+ \longrightarrow 2_1^+$	621	2.6(2)	2.8	
$0_3^+ \longrightarrow 2_1^+$	1195	0.71(13)	0.60	
$0_4^+ \longrightarrow 2_2^+$	873	1.23(8)	1.20	

Table 4.3: The q^2(E0/E2) values and E0 transition strengths ρ^2 in ^{106}Pd extracted in the present work. The transition energy, lifetime of the parent state, multipole mixing ratio δ(E2/M1) and branching fraction I$_\gamma$ are given for each transition if available [56]

$J_i^\pi \longrightarrow J_f^\pi$	E_γ [keV]	τ [fs]	$\delta(E2/M1)$	I$_\gamma$	q^2(E0/E2)	$\rho^2 \cdot 10^3$
$0_2^+ \longrightarrow 0_1^+$	1134	8400(1900)			0.166(15)	17(4)
$0_3^+ \longrightarrow 0_1^+$	1706	4000(700)			0.09(15)	2(4)
$0_4^+ \longrightarrow 0_1^+$	2001	> 1200			0.124(18)	< 19
$0_4^+ \longrightarrow 0_2^+$	867	> 1200			0.22(6)	< 90
$2_2^+ \longrightarrow 2_1^+$	616	4500(360)	-8.7^{+17}_{-19}	0.647(24)	0.027(38)	5(8)
$2_3^+ \longrightarrow 2_1^+$	1050	1900(190)	0.24(1)	0.853(34)	4.2(18)	26(11)

For the other E0 transitions a comparison between present and previous values is reported in Table 4.4. Again the good agreement of the ρ^2 values extracted in the present work with the ones from previous measurements indicate a successful outcome of the first experiment performed with the SLICES setup.

Table 4.4: A comparison between the monopole strengths ρ^2 and q^2(E0/E2) ratios extracted in the present work and in literature values.

		q^2(E0/E2)		$\rho^2 \cdot 10^3$	
$J_i^\pi \longrightarrow J_f^\pi$	E_γ [keV]	Present	Previous	Present	Previous
$0_2^+ \longrightarrow 0_1^+$	1134	0.166(15)	0.162(7)[1]	17(4)	16.4(40)[1]
$0_3^+ \longrightarrow 0_1^+$	1706	0.09(15)		2(4)	$<$ 3[2]
$0_4^+ \longrightarrow 0_1^+$	2001	0.124(18)		$<$ 19	
$0_4^+ \longrightarrow 0_2^+$	867	0.22(6)		$<$ 90	
$2_2^+ \longrightarrow 2_1^+$	616	0.027(38)		5(8)	
$2_3^+ \longrightarrow 2_1^+$	1050	4.2(18)	5.8(33)[1]	26(11)	34(22)[2]

[1] Reference [60]

[2] Reference [54]

4.5.2 ^{106}Pd decay scheme

The coupling of SLICES with an HPGe detector allows us not only to extract the internal conversion coefficients but also to study in detail the decay scheme of the low-lying levels in ^{106}Pd.

The γ-rays energy spectrum is reported in Fig. 4.7, where the transitions relevant for this work are shown. The part of the spectrum below 300 keV is dominated by the Compton edge of the 511 keV annihilation transition, which also covers the 512 keV, $2_1^+ \longrightarrow 0_1^+$ transition of ^{106}Pd.

The γ-ray intensities (I_γ) obtained in this work have been compared with the ones reported in Ref. [20] from a previous measurement of the ^{106}Pd states populated by EC/β decay of the ^{106}Ag. In particular, I_γ values have been calculated as:

$$I_\gamma = \frac{N_\gamma}{\epsilon_\gamma} \frac{\epsilon_{\gamma norm}}{N_{\gamma norm}} I_{\gamma norm} \tag{4.2}$$

where N_γ and $N_\gamma norm$ are the number of counts for the transition of interest and for the normalization transition, respectively. ϵ_γ and $\epsilon_{\gamma norm}$ are the γ-ray efficiencies for the energies of the two transitions, and $I_{\gamma norm}$ is the intensity reported in Ref. [20]. The transitions used as normalization are the $0_2^+ \rightarrow 2_1^+$ for the decay from the ^{106}Ag ground state and the $5_2^+ \rightarrow 4_1^-$ for the decay from the ^{106}Ag isomeric state. A good agreement between the results obtained in this work and in the previous EC/β^+ decay measurements has been found as reported in Table 4.5. All the transition are comparable within 2σ, the only exception is for the peak at 680 keV (underlined in the Table 4.5), which is too intense to be only due to the well-known $2_5^+ \longrightarrow 2_3^+$ (from ^{106}Ag fast decay) and $5_2^+ \longrightarrow 4_3^+$ (from ^{106m}Ag decay) transitions. Consequently, an additional contribution is suggested, see discussion below.

With the aim to extend the comparison to the experiment which populated the levels of interest through different reactions, the branching ratios of the observed transitions have been calculated using the expression:

$$BR_f^i = 100 \frac{I_f^i}{I_{norm}^i} \tag{4.3}$$

where I_f^i and I_{norm}^i are the γ-ray decay intensities of the transition of interest and the

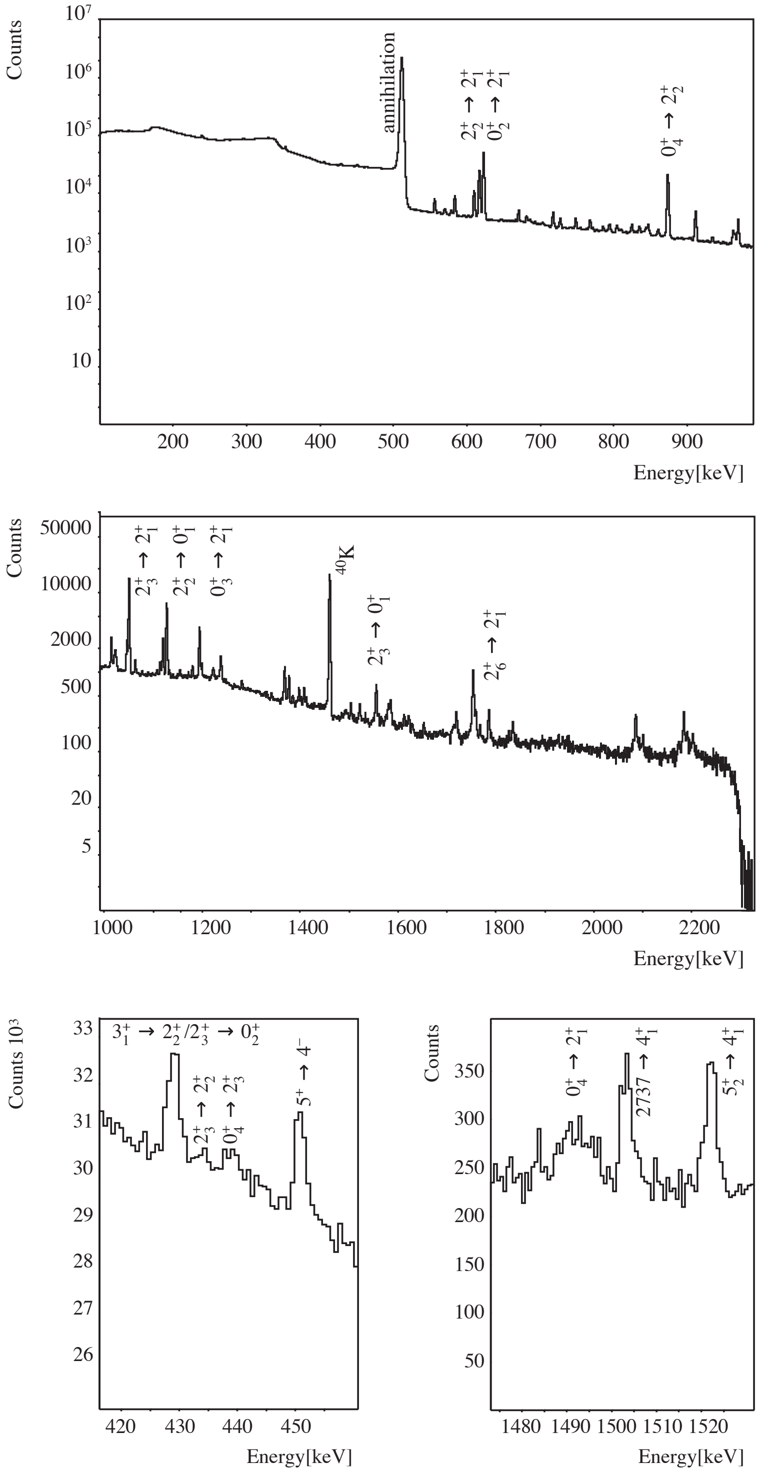

Figure 4.7: Sections of the ^{106}Pd γ-ray energy spectrum. The most intense peaks of interest are labeled with spin and parity of the initial and final levels.Also the contaminant peak has been labeled.

Table 4.5: Some of the γ-ray intensities measured in this thesis compared with the ones from literature in which the state of interest have been populated by EC/β^+ decay of the ground state (upper part) and isomeric state (lower part) of ^{106}Ag.

		^{106}Ag	
E_γ [keV]	$J_i^\pi \longrightarrow J_f^\pi$	I$_\gamma$(Present)	I$_\gamma$ [20]
429	$2_3^+ \longrightarrow 0_2^+$	0.29(4)	0.31(3)
434	$2_3^+ \longrightarrow 2_2^+$	0.09(3)	0.09(9)
439	$0_4^+ \longrightarrow 2_3^+$	0.16(4)	0.23(3)
578	$0_3^+ \longrightarrow 2_2^+$	0.24(2)	0.26(3)
616	$2_2^+ \longrightarrow 2_1^+$	6.05(12)	5.7(2)
622	$0_2^+ \longrightarrow 2_1^+$	12.70(16)	12.7(3)
680	$2_5^+ \longrightarrow 2_3^+$	0.25(2)	0.13(2)
873	$0_4^+ \longrightarrow 2_2^+$	7.46(10)	8(2)
1050	$2_3^+ \longrightarrow 2_1^+$	6.03(6)	6.7(2)
1109	$0_2^+ \longrightarrow 2_1^+$	0.12(1)	0.17(2)
1114	$2_5^+ \longrightarrow 2_2^+$	0.20(1)	0.25(2)
1128	$2_2^+ \longrightarrow 0_1^+$	2.98(4)	2,9(1)
1180	$2_6^+ \longrightarrow 2_2^+$	0.18(2)	0.22(2)
1194	$0_3^+ \longrightarrow 2_1^+$	1.50(3)	1.6(1)
1398	$2_4^+ \longrightarrow 2_1^+$	0.11(1)	0.12(1)

		^{106m}Ag	
E_γ [keV]	$J_i^\pi \longrightarrow J_f^\pi$	I$_\gamma$(Present)	I$_\gamma$ [20]
430	$3_1^+ \longrightarrow 2_2^+$	190(28)	150(4)
451	$5_2^+ \longrightarrow 4_1^-$	322(25)	322(8)
680	$5_2^+ \longrightarrow 4_3^+$	17(3)	17.6(9)
703	$4_2^+ \longrightarrow 4_1^+$	63(8)	51(2)
748	$4_1^+ \longrightarrow 3_1^+$	251(12)	235(7)
804	$4_2^+ \longrightarrow 2_2^+$	155(17)	141(6)
824	$5_2^+ \longrightarrow 4_2^+$	182(13)	175(5)
1045	$3_1^+ \longrightarrow 2_1^+$	354(10)	337(11)
1199	$5_2^+ \longrightarrow 3_1^+$	122(9)	128(6)
1223	$4_1^- \longrightarrow 2_2^+$	95(11)	80(4)

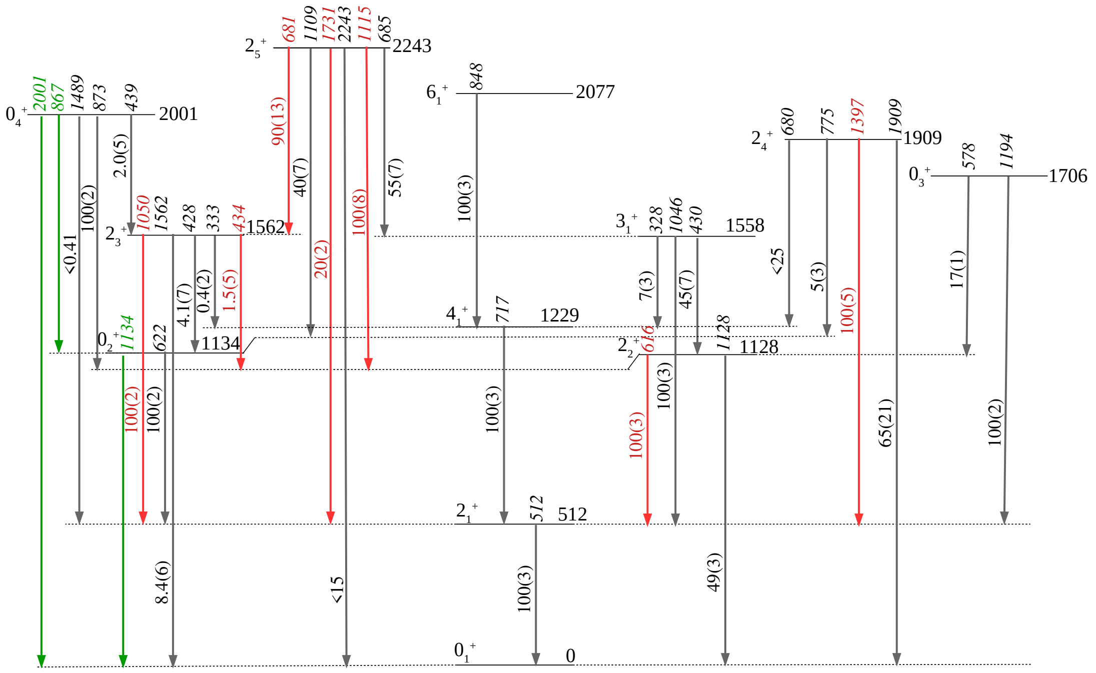

Figure 4.8: Partial level scheme of ^{106}Pd. The observed γ-ray transitions with the related branching ratios extracted in this experiment are reported next to the arrow. The observed E0 transitions between the excited 0^+ states are reported in green. The transition with mixed E0, E2 and M1 multipolarities are presented in red.

most intense transition de-exciting the i-th level of interest, respectively.

Fig. 4.8 shows the level scheme, up to an energy ~ 2.3 MeV. The decay branching ratios reported for each level were obtained in the present work. The branching ratios obtained in the present work are compared with those from the NNDC database [20] and with results from neutrons inelastic scattering experiment [56] in Table 4.6. In this paper a determination of new transitions has been provided. In particular, from the 2_4^+ level at 1909.5 keV four new transitions are assigned: $2_4^+ \longrightarrow 2_3^+$ at 347 keV, $2_4^+ \longrightarrow 3_1^+$ at 352 keV, $2_4^+ \longrightarrow 4_1^+$ at 680 keV and $2_4^+ \longrightarrow 0_2^+$ at 776 keV.

In our experiment, the peak at 680 keV, as already discussed, seems to provide a hint of an extra contribution not reported in the EC/β^+ decay measurements that could be due to the new proposed $2_4^+ \longrightarrow 4_1^+$ transition. A 439 keV transition from the 0_4^+ state to the 2_3^+ one, not reported in [56], is visible in the γ-ray energy spectrum (see left part of the lower panel of Fig. 4.7). A small peak at an energy of ~ 1489 keV has been assigned to the $0_4^+ \longrightarrow 2_1^+$ transition (see right part of the lower panel of Fig. 4.7). Both these transitions were previously reported in Ref. [20]. We cannot confirm the existence of the 347 keV, $2_4^+ \longrightarrow 2_3^+$, 352 keV, $2_4^+ \longrightarrow 3_1^+$ since their intensities are below the sensitivity level of this work. For this conclusion, an upper limit on their area has been established with a 95% confidence limit, using the method described in Ref. [19]. A critical limit L$_C$ has been defined as the number of counts below which a peak can be claimed not to be statistically significant. The area A above the background will be zero but distributed with a Gaussian probability above and below zero. The spread or standard deviation of this distribution will be indicated as σ_0. In the case one doesn't observe an expected area A and wants to discriminate if it is below the

Table 4.6: Some of the branching ratios measured in this work compared with those already reported in previous measurements.

		BR		
$J_i^\pi \longrightarrow J_f^\pi$	E_γ [keV]	Present	NSD[20]	Prados[56]
$0_3^+ \longrightarrow 2_1^+$	1194	100(2)	100.0(7)	100.0(30)
$0_3^+ \longrightarrow 2_2^+$	578	17(1)	15.1(11)	16.70(84)
$0_4^+ \longrightarrow 2_3^+$	439	2.0(5)	2.9(5)	
$0_4^+ \longrightarrow 2_2^+$	873	100(2)	100.0(12)	100
$0_4^+ \longrightarrow 2_1^+$	1489	< 0.41	0.75(13)	
$2_2^+ \longrightarrow 2_1^+$	616	100(3)	100.0(24)	100.0(30)
$2_2^+ \longrightarrow 0_1^+$	1128	49(3)	54.4(8)	54.6(16)
$2_3^+ \longrightarrow 4_1^+$	333	0.4(2)		0.40(10)
$2_3^+ \longrightarrow 0_2^+$	429	4.1(7)	4.53(13)	4.40(88)
$2_3^+ \longrightarrow 2_2^+$	434	1.5(5)	1.30(13)	
$2_3^+ \longrightarrow 2_1^+$	1050	100(2)	100.0(17)	100.0(30)
$2_3^+ \longrightarrow 0_1^+$	1562	8.4(6)	10.43(12)	11.20(56)
$2_4^+ \longrightarrow 2_1^+$	1397	100(5)	100.0(10)	100.0(30)
$2_4^+ \longrightarrow 4_1^+$	680	< 25		7.50(38)
$2_4^+ \longrightarrow 0_2^+$	776	5(3)		5.50(28)
$2_4^+ \longrightarrow 0_1^+$	1909	65(21)	35(4)	46.4(23)
$2_5^+ \longrightarrow 2_3^+$	680	90(13)	78(14)	98(15)
$2_5^+ \longrightarrow 3_1^+$	685	55(7)	42.8(16)	48.4(24)
$2_5^+ \longrightarrow 0_2^+$	1109	40(7)	47(4)	50.3(25)
$2_5^+ \longrightarrow 2_2^+$	1114	100(8)	1000(7)	100.0(30)
$2_5^+ \longrightarrow 2_1^+$	1730	20(2)	17.9(13)	16.59(83)
$2_5^+ \longrightarrow 0_1^+$	2243	< 15	15.8(7)	19.19(96)

background or not detected, they can claim it is not detected if it exceeds a certain number of standard deviations σ_0, namely if A $> k \cdot \sigma_0$. The factor k will be selected to provide a certain degree of confidence in the conclusion. For a confidence level of 95%, k would be 1.645. Therefore the critical limit would be $\mathrm{L}_C = 1.645\sigma_0$. Thanks to the background peak detected at ≈300 keV we found a FWHM of ≈9 channels. The σ_0 has been evaluated as the Poisson-distributed variable $\sigma(count) = \sqrt{count}$, where *count* is obtained integrating the background over 9 channels centered at the energy of the transition of interest. The calculated L_C is higher than the expected counts for the 347 keV, $2_4^+ \longrightarrow 2_3^+$, 352 keV, $2_4^+ \longrightarrow 3_1^+$ transitions.

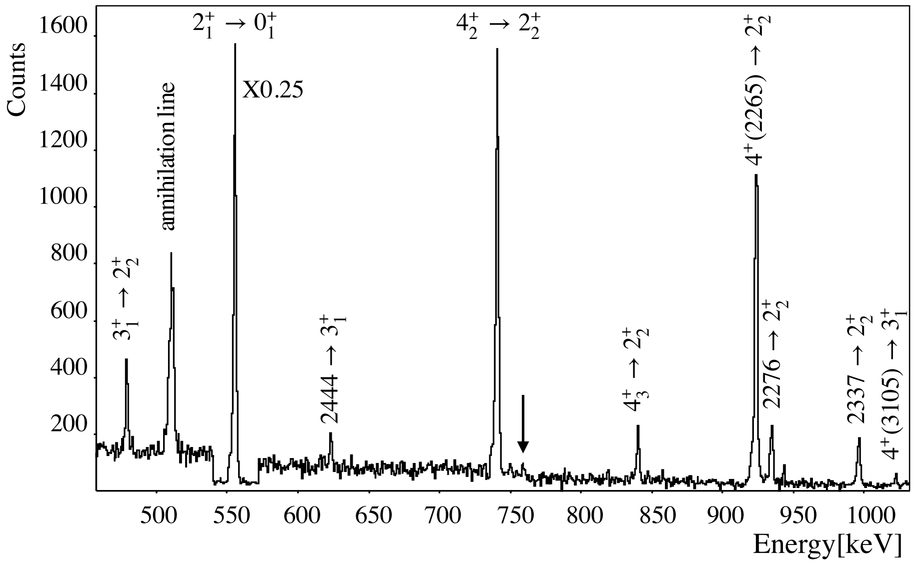

Figure 4.9: Section of the ^{104}Pd γ-ray energy spectrum gated on the 786 keV, $2_2^+ \longrightarrow 2_1^+$ transition showing the region around 750 keV. A small peak is visible at an energy of 759 keV (indicated by the arrow). The range around the $2_1^+ \longrightarrow 0_1^+$ transition at 556 keV has been multiplied by 0.25 for visualisation purposes.

4.6 ICE measurements in ^{104}Pd

Some years ago the Florence spectroscopy group has performed measurements of internal conversion electrons and $\gamma - \gamma$ coincidences to study the properties of the low-lying excited states in ^{104}Pd.

The states in ^{104}Pd were populated in the EC/β^+ decay of ^{104g}Ag ($T_{1/2} = 69\ min$) and ^{104m}Ag ($T_{1/2} = 34\ min$), produced via (p,n) reaction on a target of ^{104}Pd. A proton beam, at an energy of 6.8 MeV, from the CN accelerator of LNL was used.

The E0 strengths deduced in this experiment for transition between low-lying states having the same J are reported in Table 5.2 (more detailed discussion below).

Since the identification of a possible candidate to be associated to the 0^+ state having $n_d = 3$ is very important for the present study, the old data have been re-analysed. Aim of this new analysis is to gain a deeper insight into the existence of a 0_4^+ state, reported in Ref. [20] at 2103(2) keV. This level has been seen only in a (p, p') reaction and no information is given on its decay properties.

Since the $n_d = 3$, 0^+ state predicted by the IBM model has a preferential decay to the 2_2^+ level, the γ-ray energy spectrum acquired in coincidence with the 786 keV $2_2^+ \longrightarrow 2_1^+$ transition, has been examined to investigate the possible existence of a $0_4^+ \longrightarrow 2_2^+$ transition. Indeed a small peak is visible (see. Fig. 4.9) at 759.3(5) keV. In the single spectra, this peak is completely dominated by the more intense 758.8 keV $4_2^+ \longrightarrow 4_1^+$ transition. Assuming that the peak corresponds to the $0_4^+ \longrightarrow 2_2^+$ transition, the energy of the initial level would be 2101.0(5) keV.

As a consequence possible transition associated to de-excitations from this state to

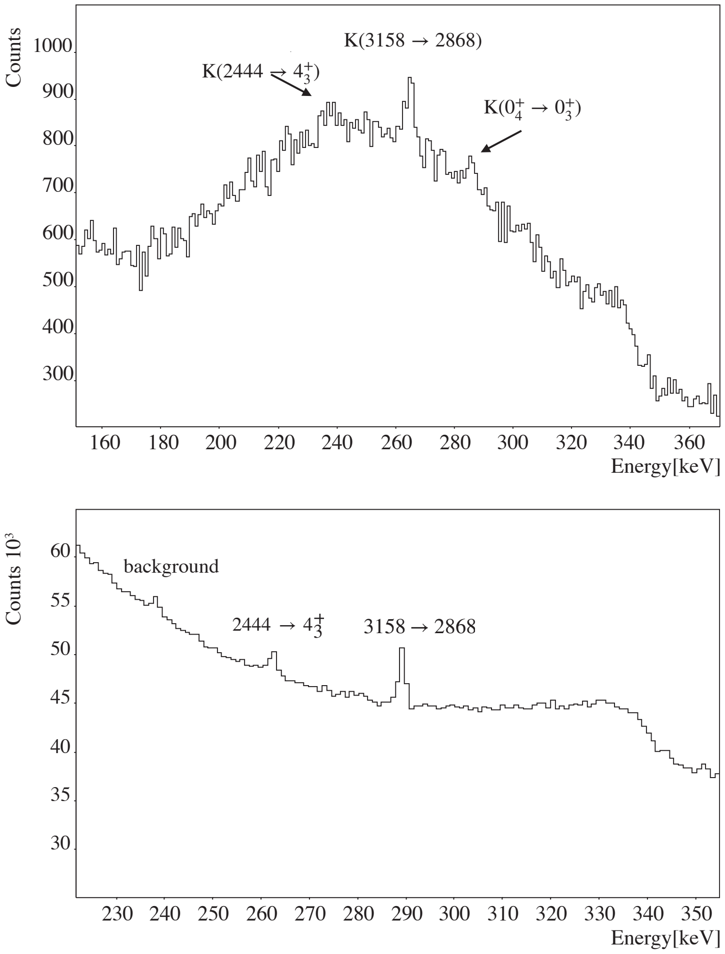

Figure 4.10: Sections of the ^{104}Pd electron and γ-ray energy spectra. Upper panel: Section of the electron energy spectrum in the 160 – 360 keV energy range. The small peak visible at an energy of 284 keV has been assigned to the $0_4^+ \longrightarrow 0_3^+$ transition. Lower panel: Portion of the γ-ray energy spectrum in the 230 – 350 energy range. No peak is visible above the line corresponding to the 289 keV transition from the 4^+ state at 3158 keV. See text for more details.

the 2_1^+ state and to the 0_2^+, 0_3^+ ones were searched for in the γ-ray and electron spectra, respectively. The energies corresponding to the γ and E0 transitions would be 1545.2 keV, 743.0(5) keV, and 283.8(5) keV, respectively.

A new 1545.2(3) keV transition was indeed identified in Ref. [6] but was assigned to the decay of the 2868.7 keV state, populated in the decay of the 5^+ state of ^{104}Ag ($T_{1/2}$ = 69 *min*). In this work, the intensity ratio of the 1545 keV γ transition to a reference γ-ray de-exciting a state that is known to be strongly populated only by either the 5^+ or the 2^+ state of ^{104}Ag was checked as a function of time. The result is that it cannot be excluded that the 1545.2(3) keV transition has a component coming from a level populated in the faster decay ($T_{1/2} = 34$ *min*) from the 2^+ state.

The 743 keV E0 transition in the electron spectrum would be completely covered by the much more intense K-conversion line of the 768 keV, $4_1^+ \longrightarrow 2_1^+$ transition (unfortunately no electron-γ coincidences were acquired). A small peak at 284 keV was instead visible in the electron spectrum, as shown in the upper panel of Fig. 4.10. It is too intense to be due to the L-conversion line of the 289 keV transition from the 4^+ level at 3158 keV. Since in the corresponding γ-ray energy spectrum (Fig. 4.10, lower panel), there is no peak at an energy $\sim$ 308 keV (while the peak corresponding to the 289 keV transition is clearly visible) we tentatively assign E0 multipolarity to the transition and hence spin-parity 0^+ to the level at an energy of 2101 keV in ^{104}Pd.

5. Interpretation of the Experimental Results

In this chapter, the IBM-2 analysis performed using the NPBOS code is presented. The obtained values are compared to the experimental results with the aim to provide further information for an improved understanding of the structure of low-lying 0^+ and 2^+ states in the ^{104,106}Pd isotopes. Furthermore the experimental $\rho^2(0_2^+ \rightarrow 0_1^+)$ has been analyzed in a simple two-level mixing model, to extract information on the deformation and mixing of the two levels.

5.1 IBM-2 Calculations

In order to further clarify to what extent the interpretation of the Pd isotopes in the framework of the IBM-2 model is valid, we performed an analysis of the available experimental data on the E0 transition between the low-lying states in $^{104-106}$Pd. The analysis is limited to these isotopes, for which new experimental data concerning the low-lying 0^+ and 2^+ states have been obtained in this thesis.

The analysis has been performed by using for the Hamiltonian the same expression used in [29, 28]:

$$\begin{aligned} H = \quad & \varepsilon\,(\hat{n}_{d_\pi} + \hat{n}_{d_\nu}) + \kappa\,\hat{Q}_\pi[\chi_\pi] \cdot \hat{Q}_\nu[\chi_\nu] + \\ & w_{\pi\nu}\,\hat{L}_\pi \cdot \hat{L}_\nu + \hat{M}_{\pi\nu}[\xi_1, \xi_2, \xi_3] \end{aligned} \tag{5.1}$$

where the indexes π and ν refer to proton- and neutron-bosons, respectively. In the first term, $\hat{n}_d$ ($\hat{n}_d = \hat{n}_{d_\pi} + \hat{n}_{d_\nu}$) is the d-boson number operator. The second and third terms represent the quadrupole and dipole interactions. The Majorana operator, $\hat{M}_{\pi\nu}[\xi_1, \xi_2, \xi_3]$, properly accounts for the so called mixed-symmetry states (i.e. states partly antisymmetric under the interchange of proton and neutron boson degrees of freedom). See Appendix A for a detailed explanation of all the terms and all the parameters present in Eq. 5.1.

For the parameters ϵ, κ, $w_{\pi\nu}$, ξ_2, ξ_3 the values reported in [29] have been adopted. The authors have been determined these parameters in order to reproduce as closely as possible the excitation-energy of all positive parity levels for which a clear indication of the spin value exists. For the final choice of the parameters χ_π and χ_ν , their influence on quadrupole moments and E2/M1 mixing ratios has also been taken into account. The values of the χ_π (dimensionless) and ξ_1 parameters, kept fixed along the isotopic chain, are -0.9 and 1.0 MeV [29], respectively. The values of the parameters varying as a function of the mass number, A, are reported in Table 5.1. From Ref. [29] the smooth changes along the isotopic chain is evident, which is just what is to be expected when the states under study have a collective structure.

Table 5.1: Hamiltonian parameters used in the IBM-2 calculations. The values are taken from Ref.[29]. All parameters are in MeV, except for χ_ν (dimensionless).

A	ε	κ	χ_ν	$w_{\pi,\nu}$	ξ_2	ξ_3
104	0.800	-0.08	-0.65	0.030	0.24	-0.28
106	0.741	-0.08	-0.55	0.030	0.20	-0.25

The Hamiltonian has been diagonalized in the $\mathrm{U}_{\pi,\nu}(5)$ basis, using the NPBOS code [52], which gives in its output the d-boson number components for each state. It is to be noted that, in the U(5) limit (characterized by a Hamiltonian included only the first term in Eq. 5.1) of the model, n_d is a good quantum number. The level scheme displays multiplets of levels marked by increasing values of n_d as the excitation energies increase. For this reason in the following the model states will be characterized by the value taken by the quantum number n_d.

The $\hat{T}(E2)$ and $\hat{T}(M1)$ operators which determine the E2 and M1 reduced transition probabilities between any pair of states, has the standard expressions [33] :

$$\hat{T}(E2) \equiv e_\nu \, \hat{T}_\nu(E2) + e_\pi \, \hat{T}_\pi(E2), \tag{5.2}$$

$$\hat{T}(M1) \equiv g_\nu \, \hat{T}_\nu(M1) + g_\pi \, \hat{T}_\pi(M1), \tag{5.3}$$

where e_ν, e_π and g_ν, g_π are the effective quadrupole charges and gyromagnetic ratios, respectively. The values, $e_\pi = 0.095$, $e_\nu = 0.115$ eb, $g_\pi = 0.51$ and $g_\nu = 0.28$ μ_N, derived in Ref.[29] have been adopted. The effective quadrupole charges have been deduced through a χ^2 minimum procedure performed usually performed in this field. Their values are close to those previously found for the ruthenium chain [30]. For the effective gyromagnetic ratios in Ref.[29] the values derived for the ruthenium chain [30] are adopted.

In the IBM-2 model the E0 transition operator and the E0 strength have the expressions [33]:

$$\begin{aligned} \hat{T}(E0) &= \beta_{0\nu}\hat{T}_\nu(E0) + \beta_{0\pi}\hat{T}_\pi(E0) \\ &= \beta_{0\nu}(d_\nu^\dagger \times \tilde{d}_\nu)^{(0)} + \beta_{0\pi}(d_\pi^\dagger \times \tilde{d}_\pi)^{(0)} \end{aligned} \tag{5.4}$$

$$\begin{aligned} \rho^2(J_i^+ \rightarrow J_f^+) = \frac{Z^2}{e^2R^4} &|\beta_{0\nu}\langle J_f|\hat{T}_\nu(E0)|J_i\rangle \\ &+ \beta_{0\pi}\langle J_f|\hat{T}_\pi(E0)|J_i\rangle|^2 \end{aligned} \tag{5.5}$$

where $\mathrm{R}=1.2\mathrm{A}^{1/3}$ fm, and the parameters $\beta_{0\nu}$ and $\beta_{0\pi}$ are expressed in e fm^2.

The lack of systematics on the values of the E0 effective charge is one of the major difficulties in the study of the E0 transitions in the framework of IBM since very rarely these transitions are considered in the analysis.

In this thesis, in order to evaluate the effective monopole charges, the experimental data on ρ^2 have been compared with the corresponding theoretical values by performing a standard χ^2 minimization procedure restricted to the range [-1,+1] e fm^2. The ρ^2 values used in the comparison are marked with asterisks in Table 5.2. We included the $\rho^2(0_2^+ \longrightarrow 0_1^+)$ values measured in the isotone $^{100-102}$Ru nuclei to further constrain the minimization procedure.

In the comparison, we assumed that the experimental 0_3^+ state is an intruder 0^+ state in ^{104,106}Pd. This is because the model completely fails to reproduce the B(E2) values for transitions from these states, as can be seen in Fig. 5.1. Due the form of the E2 transition operators, E2 transitions obey the selection rules $\Delta n_d = 0, \pm 1$. Therefore the $0_3^+ \to 2_1^+$ transition is forbidden for isotopes having a structure close to the U(5) limit, while the 0_3^+ level in both ^{104,106}Pd isotopes preferentially decays to the 2_1^+ (see Fig. 5.1). The identification of a 0_4^+ state at 2001 keV in ^{106}Pd isotope, which decays (96%) to the 2_2^+ level and only 0.7% to the 2_1^+ level, leads to associate to the 0_3^+ state predicted by the model. Similarly, a re-analysis, performed in this thesis, of some internal conversion electrons data on ^{104}Pd (collected some years ago), seems to indicate that the 0^+ at 2101 keV might be the third collective 0^+ state in this nucleus.

Having confirmed the intruder character of the third experimental excited state (in accordance with what is reported in the literature [44, 43, 66, 29]), the comparison was made between the monopole strengths for transitions from the third theoretical state and the fourth experimental state in both isotopes.

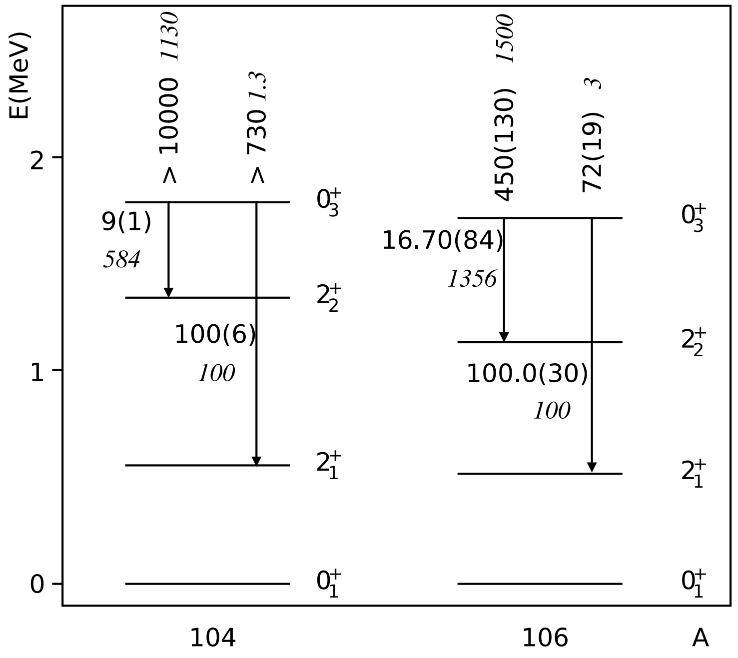

Figure 5.1: Decay scheme of the 0_3^+ state in the ^{104,106}Pd isotopes. Experimental and calculated (in italics) values for the branching ratios are shown. Experimental and predicted (in italics) B(E2) values (in 10^{-4} e^2b^2) are given in the upper part.

In Fig. 5.2 the contour plot for the normalized χ^2, resulting from the minimization procedure, is reported. The minimum is located at $\beta_{0\nu}$=0.194 e fm^2 and $\beta_{0\pi}$=0.009 e fm^2. By using these values for the effective monopole charges, we have calculated the ρ^2 reported in the last column of Table 5.2.

The agreement between experimental and calculated values of the ρ^2 for the transition de-exciting the 0_2^+ levels in ^{104,106}Pd supports the interpretation of this state as belonging to the IBM-2 model space. Also for the 2_2^+ state, the IBM-2 calculations of the $\rho^2(2_2^+ \longrightarrow 2_1^+)$ values do not contradict the interpretation of these states as belonging to the $n_d = 2$ triplet.

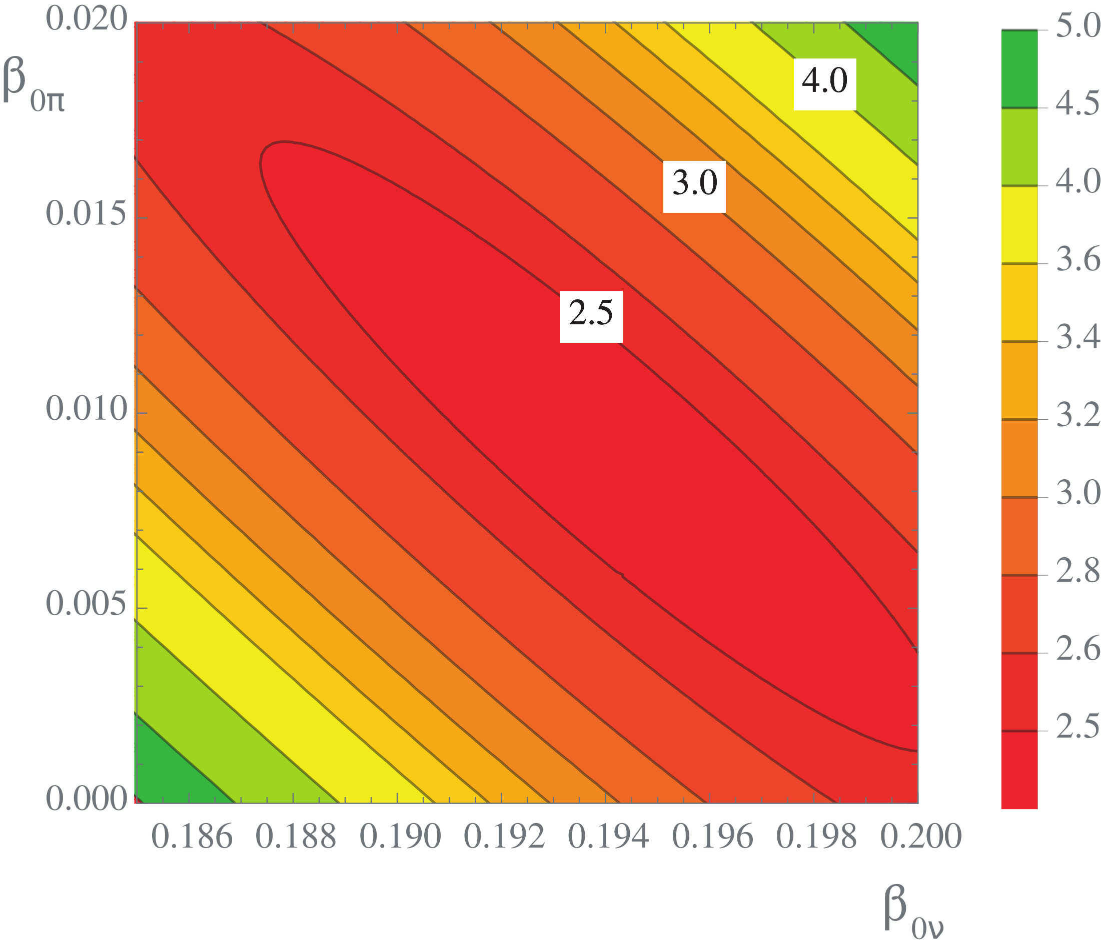

Figure 5.2: Contour plot for the reduced χ^2 variable based on the comparison of theoretical and experimental ρ^2 values as a function of the effective monopole charges $\beta_{0\nu}$ and $\beta_{0\pi}$ (in e fm^2).

The comparison between the experimental and calculated electromagnetic properties of the $n_d = 2$ candidates with spin-parity $2^+, 4^+$ has been extended to the spectroscopic quadrupole moment Q of the 2_2^+ and 4_1^+ levels. In Fig. 5.3 the experimental values of Q, normalized to the $Q(2_1^+)$, in ^{106,108,110}Pd isotopes are compared with the calculated ones. No experimental data for the Q in ^{104}Pd isotopes are reported in the literature. Values referring to the 2_2^+ and 4_1^+ levels are reported in red and green, respectively. The agreement is good and the calculations are able to correctly predict the $Q(2_2^+)$ sign inversion deduced from Coulomb Excitation experiment [62]. The interpretation of the 2_2^+, 4_1^+ and 0_2^+ levels as belonging to the $n_d = 2$ triplet is also supported by the good agreement between the experimental and calculated B(E2), B(M1), mixing ratios and branching ratios reported in Table 5.3 (from Ref. [29]).

For what concerns the identification of the possible 0^+ and 2^+ states belonging to the $n_d = 3$ multiplet, we start considering the E0 transitions from the 0_4^+ state. The calculated $\rho^2(0_4^+ \longrightarrow 0_1^+)$ value (reported in Table 5.2) is much smaller than $\rho^2(0_4^+ \longrightarrow 0_2^+)$ one as suggested by the experimental limits. Also, a general good agreement between the experimental B(E2) values and the calculated ones has been found, as reported in Table 5.3. The experimental values for E2 transitions from the

Table 5.2: Experimental values of ρ^2 in ^{104,106}Pd and ^{100,102}Ru compared to theoretical ones evaluated using the Hamiltonian parameters from Ref. [29] and the E0 effective charges $\beta_{0\nu}$=0.194 e fm^2, $\beta_{0\pi}$=0.009 e fm^2 deduced in the present work. The values marked by an asterisk have been used in the χ^2 minimization procedure.

Nuclide	$J_i^\pi \longrightarrow J_f^\pi$	E_γ [keV]	$\rho^2_{exp} \cdot 10^3$		$\rho^2_{calc} \cdot 10^3$
^{104}Pd	$0_2^+ \longrightarrow 0_1^+$	1334	$11(2)^1$	*	10
^{104}Pd	$2_2^+ \longrightarrow 2_1^+$	786	$5(4)^2$	*	1
^{104}Pd	$4_2^+ \longrightarrow 4_1^+$	759	$< 90^1$		0.5
^{106}Pd	$0_2^+ \longrightarrow 0_1^+$	1134	$17(4)^3$	*	16
^{106}Pd	$0_4^+ \longrightarrow 0_1^+$	2001	$< 19^3$		0.3
^{106}Pd	$0_4^+ \longrightarrow 0_2^+$	867	$< 90^3$		4
^{106}Pd	$2_2^+ \longrightarrow 2_1^+$	616	$5(8)^3$		1
^{106}Pd	$2_3^+ \longrightarrow 2_1^+$	1050	$26(11)^3$	*	28
^{106}Pd	$2_4^+ \longrightarrow 2_1^+$	1398	21^{+104}_{-21}		0.1
			18^{+104}_{-18}		
^{106}Pd	$2_5^+ \longrightarrow 2_2^+$	1115	96^{+434}_{-61}		18
^{100}Ru	$0_2^+ \longrightarrow 0_1^+$	1130	$10.3(18)^5$	*	11.4
^{102}Ru	$0_2^+ \longrightarrow 0_1^+$	944	$14(3)^5$	*	17

[1] Reference [6]

[2] Calculated in the present work from the data of Ref. [6]

[3] Present work

[4] Reference [60]

[5] Reference [63]

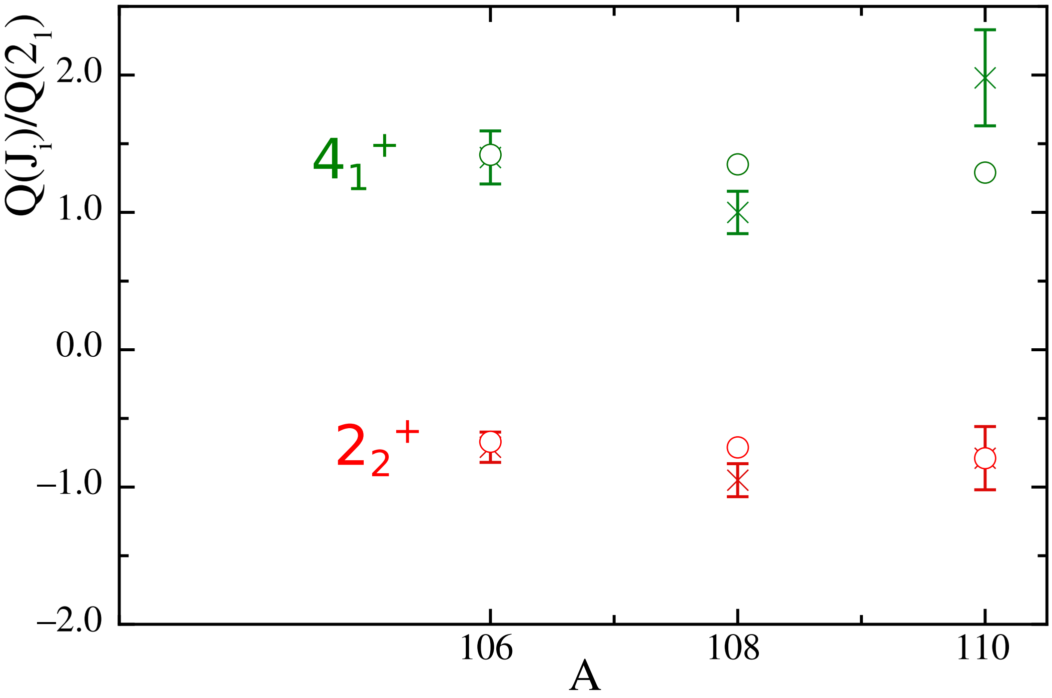

Figure 5.3: Experimental values (crosses) and theoretical values (open circles) of Q for the 2_2^+, 4_1^+ states, normalized to the Q(2_1) as a function of mass number. Data for the 4_1^+ and 2_2^+ levels are reported in green and red respectively. The values are taken from Ref. [28].

Table 5.3: The experimental values of B(E2) in $10^{-4}\,e^2b^2$ and B(M1) value in $10^{-3}\,\mu_N^2$ of the transition de-exiciting the levels of interest of ^{106}Pd. The experimental data are taken from Ref. [56], with the exception of the B(E2) marked with asterisk only reported in Ref. [62]. The theoretical values have been evaluated using the parameters from Ref. [29].

$J_i^\pi \longrightarrow J_f^\pi$	E_γ [keV]	$B(E2)_{exp}$	$B(E2)_{calc}$	$B(M1)_{exp}$	$B(M1)_{calc}$
$0_2^+ \longrightarrow 2_1^+$	439	1043(238)	1356		
$2_2^+ \longrightarrow 2_1^+$	616	1302^{+173}_{-149}	1409	$0.46^{+0.33}_{-0.18}$	0.213
$2_2^+ \longrightarrow 0_1^+$	1128	35^{+5}_{-4}	17		
$4_1^+ \longrightarrow 2_2^+$	101	$21^{+215}_{-9}*$	28		
$4_1^+ \longrightarrow 2_1^+$	717	2265(328)	1964		
$0_4^+ \longrightarrow 2_3^+$	439	< 32	30		
$0_4^+ \longrightarrow 2_2^+$	873	< 1600	1500		
$0_4^+ \longrightarrow 2_1^+$	1489	< 2	3		
$2_4^+ \longrightarrow 2_3^+$	347	3600^{+2400}_{-3600}	14		
$2_4^+ \longrightarrow 4_1^+$	680	155^{+9}_{-8}	240		
$2_4^+ \longrightarrow 0_2^+$	776	60^{+36}_{-30}	515		
$2_4^+ \longrightarrow 2_2^+$	782	13^{+12}_{-8}	230	$0.13^{+0.29}_{-0.10}$	$7 \cdot 10^{-4}$
$2_4^+ \longrightarrow 2_1^+$	1397	$0.4^{+0.4}_{-0.2}$	2	$7.3^{+4.2}_{-3.8}$	5.1
		36^{+23}_{-20}	2	$2.8^{+2.2}_{-1.6}$	5.1
$2_4^+ \longrightarrow 0_1^+$	1909	$5.7^{+3.3}_{-3.0}$	0.4		
$2_5^+ \longrightarrow 2_3^+$	680	1400^{+900}_{-700}	680	42^{+43}_{-32}	0.543
$2_5^+ \longrightarrow 3_1^+$	684	1600^{+690}_{-600}	44	$3.8^{+3.8}_{-2.0}$	0.10
$2_5^+ \longrightarrow 0_2^+$	1109	160^{+6}_{-7}	1		
$2_5^+ \longrightarrow 2_2^+$	115	100^{+150}_{-70}	1.7	19^{+15}_{-11}	0.87
$2_5^+ \longrightarrow 2_1^+$	1731	5.0^{+25}_{-21}	1.2	0.177^{+22}_{-11}	0.7
		$(6^{+155}_{-6}) \cdot 10^{-3}$	1.2	$(1.20^{+47}_{-42}) \cdot 10^{-3}$	$(6.97) \cdot 10^{-4}$
$2_5^+ \longrightarrow 0_1^+$	2242	1.8^{+7}_{-6}	1.2		

0_4^+ state are calculated using the limit on the lifetime recently reported in Ref. [56] and the branching ratios from the present analysis. The good agreement supports our interpretation, of the 0_4^+ as the 0^+ state having $n_d = 3$, predicted by the model.

For ^{104}Pd, no information about the decay of the 0_4^+ state at 2103 keV is reported in the literature, and the data analysis performed in this thesis did not allow to obtain information on the branching ratio of transitions from this level.

The agreement found between the calculated and experimental $\rho^2(2_3^+ \longrightarrow 2_1^+)$ values seems to exclude the interpretation of 2_3^+ state as a member of an intruder band. Since also all the other electromagnetic properties of this state were reasonably reproduced by the calculations in Ref. [29] we are led to confirm that it lies within the model space.

The scenario is different for the $\rho^2(2_4^+ \longrightarrow 2_1^+)$ and $\rho^2(2_5^+ \longrightarrow 2_1^+)$ strengths still known with limited precision. In Table 5.3 the comparison between the experimental B(E2) and B(M1) values (from Ref. [56]) and the calculated ones for the 2_4^+ and 2_5^+ states is reported. For both states, the electromagnetic transition probabilities are known with a large uncertainty so that the comparison with the calculation is not decisive. As a consequence, no definite conclusion could be drawn on the interpretation of the 2_4^+ states as a member of the intruder band built on the 0_3^+ state, as suggested in Ref. [66]. We note also that no evidence for the $2_4^+ \rightarrow 0_3^+$ transition has been reported so far and also in this thesis no such transition was observed. Similarly, no definite conclusion can be drawn on the character of the 2_5^+ state. However, since this state does not decay to the 4_1^+, while the 2_4^+ does, it seems preferable to associate the 2_4^+ state to the 2^+ state of a $n_d = 3$ quintuplet and the 2_5^+ state to an intruder configuration as suggested in Ref. [26].

5.2 Two-level Mixing

As already mentioned, E0 transitions reflect a change in the radial distribution of the electric charge inside the nucleus, therefore a large E0 strength is expected whenever configurations with different mean-square charge radii mix. An enhancement of the monopole strength in transitions between levels having the same J may be considered as a “signature” of strong mixing between two states with different deformation [34]. According to the conclusions reported in Ref. [54], the large ρ^2 values measured in ^{106}Pd provide evidence for shape coexistence in this nucleus.

In this section, the mixing amplitude a has been extracted using the available experimental data and the two-level mixing model described in Sec. 2.3. Information on the deformation of the 0_2^+ state has been inferred.

5.2.1 Extraction of the mixing amplitude a

According to Eq. 2.15, the deformation parameter β_1, β_2, γ_1 and γ_2 of the unmixed $|1\rangle$ and $|2\rangle$ configurations are needed, in order to extract the mixing amplitude a from the measured ρ^2 monopole strength.

As a first step, only the terms up to the second order in β in Eq. 2.15 have been considered. In this approximation the expression for the E0 strength becomes:

$$\rho^2(0_2^+ \rightarrow 0_1^+) = (\frac{3Z}{4\pi})^2 a^2 (1-a^2) |(\beta_1^2 - \beta_2^2)|^2 \tag{5.6}$$

The deformation parameters for the first two 0^+ states in ^{106}Pd have been measured in a Coulomb Excitation experiment performed some years ago [62]. Here the authors apply the quadrupole sum rules method [15] to determine the deformation parameters Q and δ, defined in the intrinsic frame of the nucleus, and related to the Hill-Wheeler parameters β and γ. The Q parameter describes the magnitude of the deformation, while the δ parameter measures triaxiality. From the data reported in [62] the experimental values $\beta^2(0_1) = 0.050(2)$ and $\beta^2(0_2) = 0.069(3)$ have been extracted.

In the quadrupole sum rule approach the Q^2 invariant, hence the β^2 one is written in terms of the E2 matrix elements connecting the 0^+ state in question with all the low-lying 2^+ excited states. The parameter $\beta^2(0_1)(\beta^2(0_2))$ have the expression:

$$\beta^2(0_1) = \frac{1}{k_0^2}\frac{1}{5}\sum_m \langle 0_1 \,||E2||\, 2_m\rangle \langle 2_m \,||E2||\, 0_1\rangle \tag{5.7}$$

where $k_0 = (3/4\pi)ZR^2$

Considering the 0_1^+ state as a linear combination of two basic configurations $|1\rangle$ and $|2\rangle$ (see Eq. 2.12), it is possible to express the $\beta^2(0_1)$ parameter as:

$$\begin{aligned}\beta^2(0_1) = \frac{1}{k_0^2}\frac{1}{5}[a^2 &\sum_m \langle 1 \,||E2||\, 2_m\rangle \langle 2_m \,||E2||\, 1\rangle \\ &+ ab\sum_m \langle 1 \,||E2||\, 2_m\rangle \langle 2_m \,||E2||\, 2\rangle \\ &+ ba\sum_m \langle 2 \,||E2||\, 2_m\rangle \langle 2_m \,||E2||\, 1\rangle \\ &+ b^2\sum_m \langle 2 \,||E2||\, 2_m\rangle \langle 2_m \,||E2||\, 2\rangle]\end{aligned} \tag{5.8}$$

On the basis of the quadrupole sum rules method [15] the second and third terms in Eq. 5.8 are negligible. The first and the last terms are the deformation parameters β_1^2 and β_2^2 of the unmixed $|1\rangle$ and $|2\rangle$ configurations, respectively. Following the same procedure for the 0_2^+ state, the deformation parameters of the experimental 0_1^+ and 0_2^+ levels are given by:

$$\begin{aligned}\beta^2(0_1) &= a^2\beta_1^2 + b^2\beta_2^2 \\ \beta^2(0_2) &= b^2\beta_1^2 - a^2\beta_2^2\end{aligned} \tag{5.9}$$

Inserting the experimental values in the Eqs. (5.6,5.9) a system of three linear equations with three unknown quantities, a β_1 β_2, is obtained. The resulting values are $a^2 = 0.1$ for the mixing coefficient, $\beta_1 = 0.29$ $\beta_2 = 0.21$ for the quadrupole deformation parameters of the $|1\rangle$ and $|2\rangle$ states respectively. The value obtained for a indicates that the mixing of the two $|1\rangle$ and $|2\rangle$ states is small, hence the ground state and the 0_2^+ state have a rather ”pure” configuration. In this context, one can assume that the deformation of the ground (the 0_2^+) state is similar to those of the $|1\rangle$ ($|2\rangle$) one.

5.2.2 Determination of γ_2

As a second step the value of $\rho^2(0_2^+ \longrightarrow 0_1^+)$ has been calculated keeping all the terms in Eq. (2.15), under the hypothesis that the deformation β_1 β_2 of the unmixed states are the same of the experimental 0_1^+ and 0_2^+ ones (small mixing).

We assume in the calculations the values, deduced from experiment [62], $\sqrt{\beta^2(0_1)} = 0.22$, $\gamma_1 = 20°$ and $\sqrt{\beta^2(0_2)} = 0.26$. The deformation parameter γ_2 has been varied over a reasonable range for three different set of values for a^2, corresponding to small

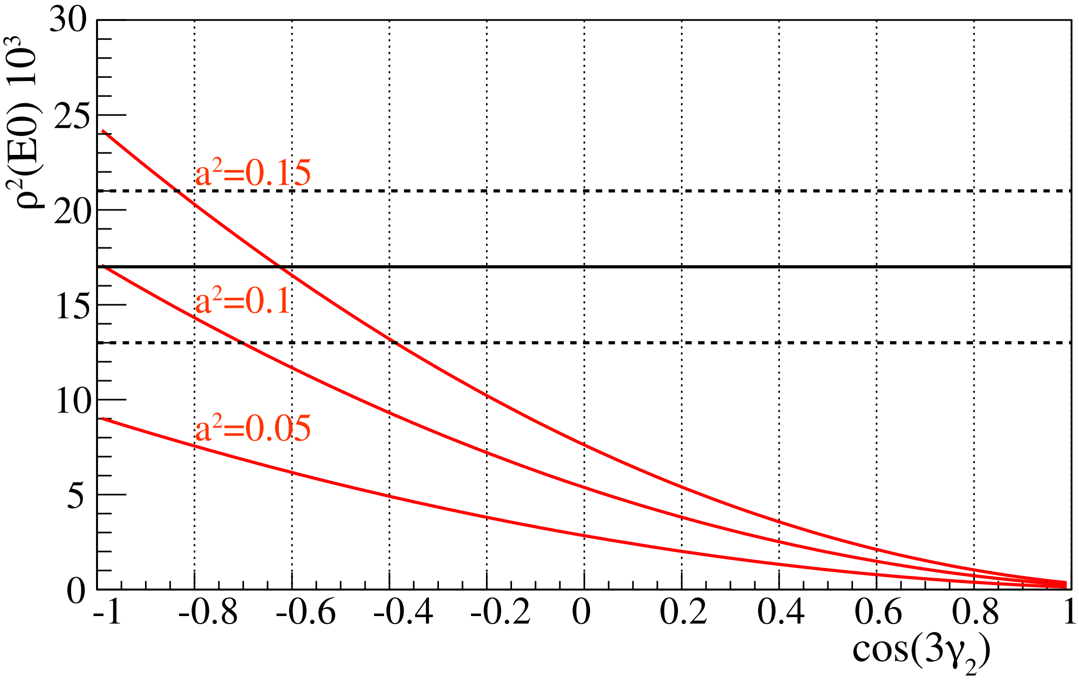

Figure 5.4: Values of ρ^2 calculated as a function of the deformation parameter $cos(3\gamma_2)$ for different values of the squared mixing amplitude a^2, assumed γ_1, β_1 and β_2 reported in Ref. [62]. The horizontal lines indicate the experimental value together with the $\pm\sigma$ statistical uncertainty.

mixing. The calculated values of $\rho^2(0_2^+ \longrightarrow 0_1^+)$ are compared to the experimental one in Fig. 5.4. The comparison implies $\gamma_2 \approx 45°$ for the $|2\rangle$ state, hence for the 0_2^+ state. This result would imply the coexistence of different shapes, triaxial for the ground state and oblate for the first excited 0^+ state, in agreement with the conclusions drawn in Ref. [54].

6. Conclusions and Further Perspectives

In this thesis, the design and implementation of the new apparatus for electron spectroscopy, SLICES, have been presented. The main components of the apparatus are described in detail: the Si(Li) detector and the magnetic transport system, which have the primary role to reduce the background from e.g. γ-rays and to focus the electrons on the detector with high efficiency.

In particular, it has been underlined how the efficiency is not only affected by the choice of the geometric configuration (the distances target-magnetic lens and magnetic lens-detector) but also by the shapes and thicknesses of the magnets, which generate the magnetic field. On the basis of the electron energy range of interest, the design of magnetic lens has to be studied using simulations based on the CST and GEANT4 software, to grant the highest detection efficiency for each case. The validation of the simulated efficiency curves obtained via the standard radioactive source makes the procedure a powerful tool in the planning of SLICES configuration for the future experiment.

The first experiment performed at LNL using SLICES has been described. SLICES has been coupled to an HPGe detector to study the structure of the low-lying states in ^{106}Pd. The internal conversion coefficients, the ratio $q^2(E0/E2)$ and the ρ^2 values have been deduced. In particular, the $q^2(E0/E2)$ and the ρ^2 values for transitions from the 0^+_4 state are extracted for the first time in this thesis. Also, the E0 contribution to the K conversion $2^+_2 \longrightarrow 2^+_1$ transition is determined for the first time. The obtained data allow us to discriminate between the two conflicting values reported in the literature for the α_K of the $(2^+_3 \longrightarrow 2^+_1)$ transition.

The good agreement of the present results with the ones already available in the literature is a test of the reliability of SLICES apparatus in performing internal conversion electron measurements.

With the aim to extend our study to the neighbor ^{104}Pd, the data from a previously performed ICE experiment were re-analyzed finding hints of the existence of the fourth 0^+ state at 2101 keV.

Calculations of the ρ^2 values in ^{104,106}Pd were performed in the framework of the interacting boson model, using the parameters reported in Ref. [29] and the monopole boson charges extracted in the present work. The agreement between theoretical calculations and experimental results is good, once the experimental 0^+_3 is considered as intruder state. For ^{106}Pd isotope the 0^+_2, 2^+_2, 4^+_1 experimental states have been associated with the predicted states having a structure resembling that of states belonging to the n_d=2 multiplets of the U(5) limit. For what concern the n_d=3 multiplets of the U(5) limit, the experimental 0^+_4 state has been identified as the possible 0^+ state belonging this multiplets, while the identification of the 2^+ state is difficult due to the limited precision of the available experimental data.

The experimental value of the $\rho^2(0_2^+ \longrightarrow 0_1^+)$ in ^{106}Pd has been also compared to that calculated in a simple two-states mixing model, to obtain further insight on the mixing and deformation of the first two 0^+ states in this nucleus. A shape coexistence scenario, with small mixing between different configurations has been found.

Further experimental studies aimed at providing additional information about excited 0^+ and 2^+ states in the neighboring palladium isotopes will be extremely important to confirm their interpretation as states belonging to the IBM-2 model space. For this reason, we plan to continue our investigation of Pd isotopes in a near future, proposing experiments to be performed at the CN accelerator.

Before performing new experiment, work should be done to improve the resolution of the Si(Li) detector, when its signals are acquired with digital electronics. This is especially important in view of performing experiments using the plastic scintillator for β-tagging, which require a short trapezoid rise time. For this reason, we are in contact with the electronic service of the INFN section of Milan, to modify the input stage circuit of the preamplifiers supplied by the Juelich research center.

A number of new experiments with SLICES have been already planned, both using the stable beams available at LNL or the future radioactive beam from SPES.

A Letter of Intent has been presented to study shape coexistence in the ^{96}Sr isotope:
Electron conversion measurements at SPES 1^+ beam line: measurement of E0 transitions in ^{96}Sr
Spokespersons : A.Nannini, N.Marchini, M.Rocchini

Coexistence between deformed and spherical configurations has been established for the 0_2^+ and 0_3^+ states in ^{96}Sr, however, there is a disagreement in the degree of mixing between them. Aim of the LoI is to investigate the E0 decay between low-energy 0^+ states in this nucleus, especially since the only available information on E0 transitions in ^{96}Sr is the strength of the $0_3^+ \rightarrow 0_2^+$ transition from an unpublished PhD thesis. The levels of interest will be populated via β-decay of ^{96}Rb, produced as 1^+ mass separated ions at the SPES facility. The expected yield for a 40 keV ^{96}Rb beam at SPES Phase 1 (proton current of 5 μA and UCx target) is about 2.5×10^7 p/s. The lifetime of the ^{96}Rb isotope ($T_{1/2}$=0.203 s) is ideal in performing internal conversion measurements with the SLICES spectrometer at the β-decay station.

Waiting for the completion of the SPES facility, we also propose a letter of intent for coupling SLICES with the AGATA γ-ray spectrometer [2]:
An Electron Conversion Spectrometer for AGATA: Study of the vibrational modes in stable Cd isotopes.
Spokespersons : N.Marchini, A.Nannini, A.Saltarelli

Aim of the experiment is to study the level structure of the ^{106,108}Cd isotopes, corresponding to N=58,60 isotones for the ^{104,106}Pd isotopes studied in this thesis. The even-even Cd isotopes were traditionally considered as good examples of spherical quadrupole shape vibrators. Indeed, the excitation pattern of the low-lying levels in these isotopes resembles that of a nearly harmonic vibrator, except for the presence of additional states lying close to the two- and three-phonon multiplets. While the role played by proton excitation across a Z = 50 closed shell is widely recognized to be responsible for the appearance of the intruder configurations; a still controversial matter is the amount of mixing between normal and intruder configurations. Recently, on the basis of the available values for B(E2) transition strengths and deformation parameters, a new interpretation of the low-lying energy states has been suggested; namely, a quasi rotational structure with K=0 and K=2 band, plus a shape-coexisting band based on the 0^+ intruder state. The confutation of the vibrational behaviour of the states at low energy in the Cd isotopes opens an entire spectrum of issues on the nature of 0^+ and 2^+ states in these nuclei. In this scenario a measurement of the E0 transitions, still missing for the ^{106,108}Cd isotopes, is crucial to provide further information to better understand the structure of low-lying levels in the Cd isotopes with N$\sim$ 60.

In conclusion, a new experimental setup for electron spectroscopy is now available at LNL, the SLICES spectrometer. The first experiment has been successfully performed, paving the way for future experimental campaigns, in particular, by exploiting the first radioactive beams which will be provided by the SPES facility in the next future.

A. Interacting Boson Model

A.1 IBM-1

The most general two-body Hamiltonian for a system of s and d bosons that conserves the total number of bosons (the number of creation operators equals the number of annihilation operators) can be written as:

$$\begin{aligned} H = E_0 + \epsilon_s(s^\dagger \cdot \tilde{s}) + \epsilon_d(d^\dagger \cdot \tilde{d}) \\ + \sum_{L=0,2,4} \frac{1}{2}(2L+1)^{\frac{1}{2}} c_L[[d^\dagger \times d^\dagger]^{(L)} \times [\tilde{d} \times \tilde{d}]^{(L)}]_0^{(0)} \\ + \frac{1}{\sqrt{2}} v_2[[d^\dagger \times d^\dagger]^{(2)} \times [\tilde{d} \times \tilde{s}]^{(2)} + [d^\dagger \times s^\dagger]^{(2)} \times [\tilde{d} \times \tilde{d}]^{(2)}]_0^{(0)} \\ + \frac{1}{2} v_0[[d^\dagger \times d^\dagger]^{(0)} \times [\tilde{s} \times \tilde{s}]^{(0)} + [s^\dagger \times s^\dagger]^{(0)} \times [\tilde{d} \times \tilde{d}]^{(0)}]_0^{(0)} \\ + u_2[[d^\dagger \times s^\dagger]^{(2)} \times [\tilde{d} \times \tilde{s}]_0^{(0)} + \frac{1}{2} u_0[[s^\dagger \times s^\dagger]^{(0)} \times [\tilde{s} \times \tilde{s}]^{(0)}]_0^{(0)} \end{aligned} \tag{A.1}$$

where E_0 is a core energy, ϵ_s and ϵ_d are related to the binding energies of the s and d bosons, the c_L and u_0 constant specify the interaction between d bosons and s bosons respectively, while the interaction of d bosons with s bosons is given by u_2, v_0 and v_2 constants. In this way the one-body terms are specified by the parameters ϵ_s, ϵ_d and the two-body terms are specified by the c_L, v_L and u_L parameters.

Considering the Hamiltonian in a space of a fixed number of bosons, $\hat{N} = \hat{n_s} + \hat{n_d}$, the number of independent terms is reduced. The term ϵ_s can be written as:

$$\epsilon_s(s^\dagger \cdot \tilde{s}) = \epsilon_s \hat{n_s} = \epsilon_s(\hat{N} - \hat{n_d}) = \epsilon_s \hat{N} - \epsilon_s(d^\dagger \cdot \tilde{d}) \tag{A.2}$$

When applied to the Hamiltonian, H become:

$$\begin{aligned} H = E_0' + \epsilon'(d^\dagger \cdot \tilde{d}) \\ + \sum_{L=0,2,4} \frac{1}{2}(2L+1)^{\frac{1}{2}} c_L'[[d^\dagger \times d^\dagger]^{(L)} \times [\tilde{d} \times \tilde{d}]^{(L)}]_0^{(0)} \\ + \frac{1}{\sqrt{2}} v_2[[d^\dagger \times d^\dagger]^{(2)} \times [\tilde{d} \times \tilde{s}]^{(2)} + [d^\dagger \times s^\dagger]^{(2)} \times [\tilde{d} \times \tilde{d}]^{(2)}]_0^{(0)} \\ + \frac{1}{2} v_0[[d^\dagger \times d^\dagger]^{(0)} \times [\tilde{s} \times \tilde{s}]^{(0)} + [s^\dagger \times s^\dagger]^{(0)} \times [\tilde{d} \times \tilde{d}]^{(0)}]_0^{(0)} \end{aligned} \tag{A.3}$$

with

$$E_0' = E_0 + \epsilon_s N + \frac{1}{2} u_0 N(N-1)$$

$$\epsilon' = (\epsilon_d - \epsilon_s) + \frac{1}{\sqrt{5}}u_2(N-1) - u_0(N-1)$$

$$c'_L = c_L + u_0 - \frac{2}{\sqrt{5}}u_2 \tag{A.4}$$

The operators inducing electromagnetic transitions of multipolarity L can be written in terms of s and d bosons, conserving N. For example the E0 transition operator is:

$$T_0^{(E0)} = \gamma_0 + \beta_0[d^\dagger \times \tilde{d}]_0^{(0)} \tag{A.5}$$

Knowing that:

$$\hat{n_d} = \sqrt{5} \cdot [d^\dagger \times \tilde{d}]^{(0)}] = \sqrt{5} \cdot (d^\dagger \cdot \tilde{d}) \tag{A.6}$$

the Eq. A.5 become:

$$T_0^{(E0)} = \gamma_0 + \sqrt{5} \cdot [\beta_0(d^\dagger \cdot \tilde{d})] \tag{A.7}$$

A.2 IBM-2

IBM-2 was born from the necessity to give to the collective nuclear states described in the IBM-1 a microscopic foundation rooted in the spherical shell model. In this model the particles move in the average field due to all others, producing single-particle levels characterized by j total angular momentum equal to $j = l \pm \frac{1}{2}$ with l the orbital angular momentum. The properties of a given even-even nucleus are calculated diagonalizing the residual interaction in the space provided by the average field under common assumptions: the closed shells are treated as an inert core while the rest of protons (neutrons) gradually fills the upper proton (neutron) levels.

In analogy with this view a system of interacting bosons of two types, proton bosons (s_π, d_π) and neutron bosons (s_ν, d_ν) has been provided [1]. The number of bosons (N_π, N_ν) is equal to the number of pairs of particles outside the closed shell or if the major shell is more than half filled, one should count the number of hole-pairs. For example, for $^{110}_{46}Pd_{64}$, N_π=(50-46)/2=2 is a hole state while N_ν=(64-50)/2=7 is a particle state. The total number of bosons N is:

$$N = N_\pi + N_\nu \tag{A.8}$$

Following the microscopic structure of the model, Otsuka et al. in [64] defined the Hamiltonian of the IBM-2 as:

$$H = E_0 + \epsilon_\pi \hat{n}_{d_\pi} + \epsilon_\nu \hat{n}_{d_\nu} + k\hat{Q}^\chi_\pi \cdot \hat{Q}^\chi_\nu \tag{A.9}$$

where E_0 is the core energy, the second and third terms are due to the fact that in the spherical shell model, the residual nucleon-nucleon interaction is dominated by a pairing term between identical nucleons. Often in the phenomenological calculation $\epsilon = \epsilon_\pi = \epsilon_\nu$. The last term is due to the quadrupole-quadrupole interaction between non-identical nucleons given by:

$$\hat{Q}^\chi_\rho = [d^\dagger_\rho \times \tilde{s}_\rho + s^\dagger_\rho \times \tilde{d}_\rho]^{(2)} + \chi_\rho[d^\dagger_\rho \times \tilde{d}_\rho]^{(2)}, (\rho = \pi, \nu) \tag{A.10}$$

In addition to these terms other two types of interactions have to be taken into account: on one hand the $V_{\rho\rho}$ residual boson interaction which is significant only in nuclei with few bosons outside the closed shell, on the other the Majorana term introduces the possibility to have states asymmetric under the interchange of neutrons and protons. From the spectra of even-even nuclei there is evidence that the states, not fully symmetric in neutron and proton degrees of freedom, do not occur below an excitation energy of about 2 MeV. These terms have the expressions:

$$\hat{V}_{\rho\rho} = \sum_{L=0,2,4} \frac{1}{2}(2L+1)^{\frac{1}{2}} c_L [[d^\dagger_\rho \times d^\dagger_\rho]^{(L)} \times [\tilde{d}_\rho \times \tilde{d}_\rho]^{(L)}]^{(0)}_0 \tag{A.11}$$

$$\hat{M}_{\pi\nu} = \xi_2 [s^\dagger_\nu \times d^\dagger_\pi - s^\dagger_\pi \times d^\dagger_\nu]^{(2)} \cdot [\tilde{s}_\nu \times \tilde{d}_\pi - \tilde{s}_\pi \times \tilde{d}_\nu]^{(2)} - 2 \sum_{k=1,3} \xi_k [d^\dagger_\nu \times d^\dagger_\pi]^{(k)} \cdot [\tilde{d}_\nu \times \tilde{d}_\pi]^{(k)} \tag{A.12}$$

In conclusion, the adopted Hamiltonian is:

$$H = E_0 + \epsilon(\hat{n}_{d_\pi} + \hat{n}_{d_\nu}) + k\hat{Q}^\chi_\pi \cdot \hat{Q}^\chi_\nu + \hat{V}_{\pi\pi} + \hat{V}_{\nu\nu} + \hat{M}_{\pi\nu} \tag{A.13}$$

In the IBM-2 scenario the operators inducing electromagnetic transition of multipolarity L can be written as:

$$T^{(L)} = T^{(L)}_\pi + T^{(L)}_\nu \tag{A.14}$$

In the case of E0 transition the Eq. A.7 become:

$$T^{(E0)}_0 = \gamma_0 + \sqrt{5} \cdot [\beta_{0\pi}(d^\dagger_\pi \cdot \tilde{d}_\pi) + \beta_{0\nu}(d^\dagger_\nu \cdot \tilde{d}_\nu)] \tag{A.15}$$

The M(E0) matrix element is calculated evaluating the T(E0) operator for the transition from an initial state Ψ_i to a final state Ψ_f. The ρ^2 quantity could be extracted using the Eq. 2.8.

B. DetectorConstruction class of the GEANT4 simulations

The GEANT4 software tool kit includes a complete range of functionalities to handle the physical layout of an experimental apparatus. GEANT4 uses object oriented programming in C++, thus several classes have been created according to the kinematic processes, physical interactions, detectors construction, etc. The class DetectorConstruction.cc, has the primary role of providing geometry of the SLICES spectrometer: the shape of the detector, its location in the workspace, and material of the detector. The material around the detector hence the thickness of the magnetic lens and the gap between them have to be defined.

Due to the large number of elements in our setup, we chose to design in detail the geometry using the CAD system and import the geometry into the GEANT4 simulation. Each physical element was imported in a separate STEP file, read by a dedicated program that creates the gdml files for each of them. The information for each material used in the apparatus was provided in the DetectorConstruction.cc class.

A similar procedure has been implemented for the magnetic field: it is mapped using the CST software and imported into the GEANT4 simulation. In order to propagate a particle in a field, GEANT4 solves the equation of motion using the Runge-Kutta method for the integration of the ordinary differential equations of motion. Following the method to calculate the track's motion in the magnetic field, GEANT4 breaks up the curved path into linear chord segments which are 'intersected' so see it crosses a volume boundary. To have an accurate tracking of the particle in the magnetic field the tunable parameters are:

- the miss distance (minStep, maxStep in the code below) important in the accuracy

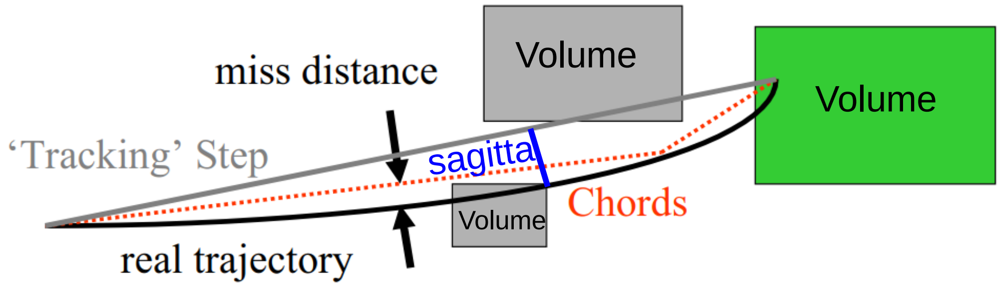

Figure B.1: Schematic view of the calculated trajectory of a particle in a magnetic field using GEANT4. The main tunable parameters are reported. See text for more details of the volume intersection (see Fig. B.1). The miss distance is a measure of the error resolution by which the chord may intersect a volume. A good compromise between accuracy and CPU time has to be found.

- δ intersection important in the accuracy of the calculation of the intersection with a volume boundary.
- δ one step important in the accuracy for the endpoint of integration steps that do not intersect a volume boundary
- δ chord to limit the maximum sagitta which is the maximum distance between the curved path and the straight line in Fig B.1.
- ϵ minimum and maximum important in the final errors of the particle position and momentum

```
#include "DetectorConstruction.hh"
#include "G4Material.hh"
#include "G4NistManager.hh"
#include "G4ElementTable.hh"
#include "G4Element.hh"
#include "G4Box.hh"
#include "G4Tubs.hh"
#include "G4LogicalVolume.hh"
#include "G4PVReplica.hh"
#include "G4GlobalMagFieldMessenger.hh"
#include "G4AutoDelete.hh"
#include "G4ThreeVector.hh"
#include "G4PVPlacement.hh"
#include "globals.hh"
#include "G4VisAttributes.hh"
#include "G4Colour.hh"
#include "G4SDManager.hh"
#include "G4MultiFunctionalDetector.hh"
#include "G4VPrimitiveScorer.hh"
#include "G4PSEnergyDeposit.hh"
#include "G4SystemOfUnits.hh"
#include "G4SDManager.hh"
#include "G4SDChargedFilter.hh"
#include "G4VPrimitiveScorer.hh"
#include "G4PSEnergyDeposit.hh"
#include "G4PSTrackLength.hh"

// Geant4 include
//
#include "globals.hh"
#include "G4GeometryManager.hh"
#include "G4VisAttributes.hh"

// Materials
//
#include "G4Material.hh"
#include "G4MaterialTable.hh"
#include "G4Element.hh"
#include "G4ElementTable.hh"
#include "G4NistManager.hh"

// Geometry includes
//
```

```
#include "G4LogicalVolume.hh"
#include "G4VPhysicalVolume.hh"
#include "G4PVParameterised.hh"
#include "G4PVPlacement.hh"
#include "G4Box.hh"
#include "G4Tubs.hh"

// GDML parser include
//
#include "G4GDMLParser.hh"

//Units include
#include "G4PhysicalConstants.hh"
#include "G4SystemOfUnits.hh"

//Magnetic field include
#include "TabulatedField3D.hh"
#include "G4Mag_UsualEqRhs.hh"
#include "G4FieldManager.hh"
#include "G4TransportationManager.hh"
#include "G4EqMagElectricField.hh"
#include "G4PropagatorInField.hh"
#include "G4ChordFinder.hh"
#include "G4ExplicitEuler.hh"
#include "G4ImplicitEuler.hh"
#include "G4SimpleRunge.hh"
#include "G4SimpleHeum.hh"
#include "G4ClassicalRK4.hh"
#include "G4HelixImplicitEuler.hh"
#include "G4HelixExplicitEuler.hh"
#include "G4HelixSimpleRunge.hh"
#include "G4CashKarpRKF45.hh"
#include "G4RKG3_Stepper.hh"
#include "G4UnitsTable.hh"
#include "G4ios.hh"
#include "G4MagIntegratorDriver.hh"
#include "G4GlobalMagFieldMessenger.hh"
#include "G4NystromRK4.hh"

// Possibility to turn off (0) magnetic field and measurement volume.
#define MAG 1          // Magnetic field grid

//
// Constructor
//


DetectorConstruction::DetectorConstruction()
: G4VUserDetectorConstruction(),
  fMagneticLogical(nullptr),
  fCheckOverlaps(true)
 {
  fField.Put(0);
  fReadFile ="assembly.gdml";
 }

//
// Destructor
//
DetectorConstruction::~DetectorConstruction()
{
```

```
}

//
// Constructs geometries and materials
//
G4VPhysicalVolume* DetectorConstruction::Construct()
{
  // Define materials
  DefineMaterials();

  // Define volumes
  return DefineVolumes();
}


void DetectorConstruction::DefineMaterials()
{

// Lead material defined using NIST Manager
  G4double a, z;
  G4double density;
  G4int ncomps, natoms;

//Elements
  G4Element* H = new G4Element("Hydrogen", "H", z=1., a=1.008*g/mole);
  G4Element* B = new G4Element("Boron", "B", z=5., a=10.81*g/mole);
  G4Element* C = new G4Element("Carbon", "C", z=6., a=12.01*g/mole);
  G4Element* N = new G4Element("Carbon", "N", z=7., a=14.007*g/mole);
  G4Element* O = new G4Element("Carbon", "O", z=8., a=15.999*g/mole);
  G4Element* F = new G4Element("Fluorine", "F", z=9., a=18.9984*g/mole);
  G4Element* Ar = new G4Element("Argon", "Ar", z=18., a=39.948*g/mole);
  G4Element* Cr = new G4Element("Chromium", "cr", z=24., a=51.996*g/mole);
  G4Element* Fe = new G4Element("IroG4NystromRK4n", "Fe", z=26., a=55.845*g/mole);
  G4Element* Ni = new G4Element("Nickel", "Ni", z=28., a=58.6934*g/mole);
  G4Element* Cu = new G4Element("Copper", "Cu", z=29., a=63.546*g/mole);
  G4Element* Zn = new G4Element("Zinc", "Zn", z=30., a=65.38*g/mole);
  G4Element* Nd = new G4Element("Neodymium", "Nd", z=60.,a=144.242*g/mole);
  G4Element* Pb = new G4Element("Lead", "Pb", z=82., a=207.2*g/mole);


//Vacuum
  density=3.e-25*g/cm3;
  G4Material* Vacuum = new G4Material("Vacuum", density,ncomps=3);
  Vacuum->AddElement(N, 78.0*perCent);
  Vacuum->AddElement(O, 21.0*perCent);
  Vacuum->AddElement(Ar,1.0*perCent);

//steel
  density= 8.03*g/cm3;
  G4Material* Steel = new G4Material("Steel", density,ncomps=3);
  Steel->AddElement(Fe, 74.0*perCent);
  Steel->AddElement(Cr, 18.0*perCent);
  Steel->AddElement(Ni, 8.0*perCent);

//Teflon
   density = 2.2 *g/cm3;
   G4Material* Teflon = new G4Material("Teflon",density,ncomps=2);
   Teflon->AddElement(C,natoms=1);
   Teflon->AddElement(F,natoms=2);

```

```
//N52
  density=7.5*g/cm3;
  G4Material* N52 = new G4Material("N52", density,ncomps=3);
  N52->AddElement(Nd,natoms=2);
  N52->AddElement(Fe,natoms=14);
  N52->AddElement(B,natoms=1);

//Brass
  density=8.7*g/cm3;
  G4Material* Brass = new G4Material("Brass", density,ncomps=3);
  Brass->AddElement(Cu,62.0*perCent);
  Brass->AddElement(Pb,3.0*perCent);
  Brass->AddElement(Zn,35.0*perCent);

// Kapton
  density=1.42*g/cm3;
  G4Material* Kapton = new G4Material("Kapton",density,ncomps=4);
  Kapton->AddElement(C,72.13*perCent);
  Kapton->AddElement(H,2.73*perCent);
  Kapton->AddElement(N,7.65*perCent);
  Kapton->AddElement(O,17.49*perCent);

// EJ212
  density=1.023*g/cm3;
  G4Material* EJ212 = new G4Material("EJ212",density,ncomps=3);
  EJ212->AddElement(C,50.00*perCent);
  EJ212->AddElement(H,35.71*perCent);
  EJ212->AddElement(O,14.29*perCent);


  // Print materials
  G4cout << *(G4Material::GetMaterialTable()) << G4endl;
}

G4VPhysicalVolume* DetectorConstruction::DefineVolumes()
{
   auto worldMaterial = G4Material::GetMaterial("Vacuum");
   auto detMaterial = G4Material::GetMaterial("EJ212");
   zOffset = 0.0*mm;

  if ( ! worldMaterial || ! detMaterial ) {
    G4ExceptionDescription msg;
    msg << "Cannot retrieve materials already defined.";
    G4Exception("DetectorConstruction::DefineVolumes()",
      "MyCode0001", FatalException, msg);
  }

  G4GDMLParser Parser;
  Parser.Read(fReadFile);
  auto WorldPhysVol = Parser.GetWorldVolume();

  //------------------------------------------------------------------
  //
  return WorldPhysVol;
}


void DetectorConstruction::ConstructSDandField()
{

#if MAG
```

```

  if(fField.Get() == 0)
     {
      //Field grid in A9.TABLE. File must be in accessible from run urn directory.
      G4MagneticField* MagField= new TabulatedField3D("//path/magfield.txt", zOffset);

      //Accuracy
      G4double minStep           = 0.01*millimeter;
      G4double deltaChord        = 3*millimeter;
      G4double deltaIntersection = 0.1*millimeter;
      G4double deltaOneStep      = 0.25*millimeter;
      G4double epsMin            = 0.5e-7;
      G4double epsMax            = 0.05;
      G4int maxStep              = 20000;

      //This is thread-local
      G4FieldManager* pFieldMgr = G4TransportationManager::GetTransportationManager()->GetFieldManager();
      pFieldMgr->SetDetectorField(MagField);

      G4Mag_UsualEqRhs* pEquation = new G4Mag_UsualEqRhs(MagField);

      //Set the stepper
      auto* pStepper = new G4NystromRK4(pEquation);
      auto pIntgrDriver = new G4MagInt_Driver(minStep,pStepper,pStepper->GetNumberOfVariables() );
      G4ChordFinder* pChordFinder = new G4ChordFinder(pIntgrDriver);

      pFieldMgr->SetChordFinder(pChordFinder);
      pFieldMgr->SetAccuraciesWithDeltaOneStep(deltaOneStep);
      pFieldMgr->GetChordFinder()->SetDeltaChord(deltaChord);
      pFieldMgr->SetDeltaIntersection(deltaIntersection);
      pFieldMgr->SetDeltaOneStep(deltaOneStep);

      G4PropagatorInField* pPropInField = G4TransportationManager::GetTransportationManager()->GetPropagatorInField();
      pPropInField->SetMinimumEpsilonStep(epsMin);
      pPropInField->SetMaximumEpsilonStep(epsMax);
      pPropInField->SetMaxLoopCount(maxStep);

      // Register the field and its manager for deleting
      G4AutoDelete::Register(MagField);
      G4AutoDelete::Register(pFieldMgr);     }

#endif
  //
  // Scorers
  //
  // declare detectors
  //

  //HPGe
  G4SDManager::GetSDMpointer()->SetVerboseLevel(1);

  auto GeDet = new G4MultiFunctionalDetector("GeDet");
  G4SDManager::GetSDMpointer()->AddNewDetector(GeDet);
  G4VPrimitiveScorer* primitivege1e;
  primitivege1e = new G4PSEnergyDeposit("GeDetE");
  GeDet->RegisterPrimitive(primitivege1e);
```

```
  SetSensitiveDetector("Part4_Germanium",GeDet);

  auto SiDet = new G4MultiFunctionalDetector("SiDet");
  G4SDManager::GetSDMpointer()->AddNewDetector(SiDet);
  G4VPrimitiveScorer* primitivege2e;
  primitivege2e = new G4PSEnergyDeposit("SiDetE");
  SiDet->RegisterPrimitive(primitivege2e);
  SetSensitiveDetector("Part8_Silicon",SiDet);
}
```

Bibliography

[1] F. Iachello A. Arima T. Otsuka and I. Talmi. In: *Physics Letters B 66, 205* (1977).

[2] S. Akkoyun et al. In: *Nucl. Instrum. Methods Phys. Res. A 668, 26* (2012).

[3] A.N. Andreyev et al. In: *Nature 405, 430* (2000).

[4] S.F. Antonova et al. In: *Sov. J. Phys. JETP 11, 554* (1960).

[5] A. Baxter et al. In: *Phys. Rev. C 48, R2140* (1993).

[6] M. E. Bellizzi et al. In: *Phys. Rev. C 63, 064313* (2001).

[7] M. Bender, P. H. Heenen, and P. G. Reinhard. In: *Rev. Mod. Phys. 75, 121* (2003).

[8] J. F. Berger, M. Girod, and D. Gogny. In: *Nuclear Physics A, 428, 23* (1984).

[9] C. A. Bertulani. *Nuclear Physics in a Nutshell.* Priceton University Press, (2007).

[10] N. Blasi et al. In: *Physical Review C 88, 014318* (2013).

[11] A. Bohr and B. Mottelson. *Nuclear Structure Vol. 1.* Benjamin, Reading, (1969).

[12] R. Casten. *Nuclear Structure from a Simple Perspective.* Oxford University Press, (1990).

[13] E. Caurier et al. In: *Rev. Mod. Phys. 77, 427* (2005).

[14] E.L. Church and J. Weneser. In: *Physical Review, 103, 1035* (1956).

[15] D. Cline. In: *Annu. Rev. Nucl. Part. Sci. 36, 683* (1986).

[16] G.G. Colvin, F. Hoyler, and S.J. Robinson. In: *J. Phys. G.: Nucl. Phys. 13, 191* (1987).

[17] *CoMPASS: Multiparametric DAQ Software for Physics Applications.* URL: https://www.caen.it/products/compass/.

[18] *CST Studio Suite Web page.* URL: https://www.3ds.com/products-services/simulia/products/cst-studio-suite/.

[19] L. A. Currie. In: *Analytical Chemistry 40,586* (1968).

[20] *Data extracted using the NNDC On-Line Data Service from the ENSDF database.* URL: http://www.nndc.bnl.gov/ensdf/.

[21] A. S. Davydov, V. S. Rostovsky, and A. A. Chaban. In: *Nucl. Phys. 27, 134* (1961).

[22] J.T.H. Dowie et al. In: *At. Data Nucl. Data Tables 131, 101283* (2020).

[23] K. Farzin et al. In: *Z. Phys. A 326,402* (1987).

[24] L. Fortunato. In: *Eur. Phys. J. A 26, 1* (2005).

[25] P. E. Garrett. In: *J. Phys. G: Nucl. Part. Phys. 43, 084002* (2016).

[26] P. E. Garrett, J. L. Wood, and S. W. Yates. In: *Physica Scripta, 93, 063001* (2018).

[27] *GEANT4, GEometry ANd Tracking.* URL: `http://geant4.web.cern.ch/geant4/`.

[28] A. Giannatiempo. In: *Physical Review C 98, 034305* (2018).

[29] A. Giannatiempo, A. Nannini, and P. Sona. In: *Physical Review C 58, 3316* (1998).

[30] A. Giannatiempo et al. In: *Phys. Rev. C 52, 2969* (1995).

[31] A. Goasduff et al. In: *Nucl. Instrum. Methods Phys. Res. A 1015, 165753* (2021).

[32] K. Heyde and J. Wood. In: *Reviews of Modern Physics 83, 1467* (2011).

[33] F. Iachello and A. Arima. *The Interacting Boson Model.* Cambridge University, (1987).

[34] C. de Coster J. Wood E. Zganja and K. Heyde. In: *Nuclear Physics A, 651, 323* (1999).

[35] J. Kern et al. In: *Nuclear Physics A, 593, 21* (1995).

[36] S. Ketelhut. In: *Nuclear Instruments and Methods in Physics Research A 753, 154* (2014).

[37] T. Kibedi et al. In: *Nucl. Instrum. Methods A 589, 202* (2008).

[38] J. van Klinken and K. Wisshak. In: *Nuclear Instruments and Methods, 98, 1* (1972).

[39] K. Wisshak J. van Klinken S.J. Feenstra and H. Faust. In: *Nuclear Instruments and Methods, 130, 427* (1975).

[40] N. Benczer Koller, M. Nessin, and T.H. Kruse. In: *Phys. Rev. 123, 262* (1961).

[41] K. Krane and R. Steffen. In: *Phys. Rev. C 2, 724* (1970).

[42] A. Saltarelli L. Guerro N. Blasi. In: *Nuclear Instruments and Methods in Physics Research A, 739, 32* (2014).

[43] G Lhersonneau et al. In: *European Physics Journal A 2, 25* (1998).

[44] G Lhersonneau et al. In: *Physics Review C 60, 014315* (1999).

[45] *LISE ++ Web page.* URL: `http://lise.nscl.msu.edu/lise.html`.

[46] *LNL Web page.* URL: `https://www.lnl.infn.it/`.

[47] N. Marchini et al. In: *Nuclear Instruments and Methods in Physics Research A, 1020, 165860* (2021).

[48] M.G. Mayer. In: *Phys. Rev. 75, 1969* (1949).

[49] M. Moukaddam. In: *Nuclear Instruments and Methods in Physics Research A, 905, 180* (2018).

[50] M. Nessin, T.H. Kruse, and K.E. Eklund. In: *Phys. Rev. 125, 639* (1962).

[51] *NuDat 2.8, Nuclear structure and nuclear decay Data.* URL: `https://www.nndc.bnl.gov/nudat2/index.jsp`.

[52] T. Otsuka and N. Yoshida. *Program NPBOS Japan Atomic Energy Research Institute report JAERI-M85-094.* (1985).

[53] A. Passoja et al. In: *Nuclear Phys. A 438, 413* (1985).

[54] E.E. Peters et al. In: *Eur. Phys. J. A 96, 52* (2016).

[55] A. Poves. In: *J. Phys. G: Nucl. Part. Phys. 43, 020401* (2016).

[56] F.M. Prados-Estévez et al. In: *Phys. Rev. C 95, 034328* (2017).

[57] J.O. Rasmussen. In: *Nuclear Physics, 19, 85* (1960).

[58] M. Schumaker. "Ph.D. Thesis". In: *Ph.D. Thesis* (2009).

[59] T. H. R. Skyrme. In: *Nuclear Physics , 9, 615* (1959).

[60] J. Smallcomb et al. In: *Eur. Phys. J. A 54, 165* (2018).

[61] *SPES Web page:* URL: `http://web.infn.it/spes`.

[62] L.E. Svensson et al. In: *Nuclear Physics A, 584, 547* (1995).

[63] R. H. Spear T. Kibédi. In: *Atomic Data and Nuclear Data Tables, 89, 77* (2005).

[64] F. Iachello T. Otsuka A. Arima and I. Talmi. In: *Physics Letters B 76, 139* (1978).

[65] D. Vautherin et al. In: *Phys. Rev. C 5, 626* (1972).

[66] Y. Wang et al. In: *Physics Review C 63, 024309* (2001).

[67] E. F. Zganjar. In: *J. Phys. G: Nucl. Part. Phys. 43, 024013* (2016).

Acknowledgements

First of all, I would like to thank the γ spectroscopy Florence group for giving me the amazing opportunity to work in nuclear physics. In particular, I have had an extraordinary Co-supervisor Adriana; a special teacher who made me get passionate about her subject, which is now also mine; most of all, an amazing person that I dare to consider a friend. I am so grateful for all your trust and teaching.

A person without whom my work would have never been possible is Marco Ottanelli. I am grateful to him for his help and for sharing his deep expertise with me, as well as for traveling with me for every my exams. His friendship has really made a difference during my PhD.

My gratefulness goes also to Prof. Pietro Sona for reading versions of the manuscript, for having raised many interesting questions and for his valuable suggestions.

Furthermore, I would like to thank Alessandro Saltarelli for providing good advice, help, and enriching ideas. He started to develop the code for the GEANT4 simulations before my arrival and he helped me in the improvement of the code. Thanks also to made us all laugh many times with your jokes.

My deepest gratitude goes to Mili, a constant partner in my life. You have supported me by helping me with all the other things in life, making me a better woman.

Finally, I thanked mom, dad, and Botox for everything they have done and represented for me. Instead of giving thanks, I feel free on this occasion to dedicate this manuscript to them. I don't care if they don't understand my work, because of the language or the physics. Every single word is for them.

List of Figures

List of Tables